

# REPORT DOCUMENTATION PAGE

Form Approved  
OMB NO. 0704-0188

Public Reporting burden for this collection of information is estimated to average 1 hour per response, including the time for reviewing instructions, searching existing data sources, gathering and maintaining the data needed, and completing and reviewing the collection of information. Send comment regarding this burden estimate or any other aspect of this collection of information, including suggestions for reducing this burden, to Washington Headquarters Services, Directorate for Information Operations and Reports, 1215 Jefferson Davis Highway, Suite 1204, Arlington, VA 22202-4302, and to the Office of Management and Budget, Paperwork Reduction Project (0704-0188), Washington, DC 20503.

1. AGENCY USE ONLY (Leave Blank)		2. REPORT DATE 8/14/01	3. REPORT TYPE AND DATES COVERED Final Report, 5/20/98-8/31/01
4. TITLE AND SUBTITLE Modeling Diesel Engine Injector Flows		5. FUNDING NUMBERS DAAG55-98-1-0318	
6. AUTHOR(S) S. D. Heister and G. A. Blaisdell			
7. PERFORMING ORGANIZATION NAME(S) AND ADDRESS(ES) Purdue University, School of Aeronautics and Astronautics 1282 Grissom Hall West Lafayette, IN 47907-1282		8. PERFORMING ORGANIZATION REPORT NUMBER	
9. SPONSORING / MONITORING AGENCY NAME(S) AND ADDRESS(ES) U. S. Army Research Office P.O. Box 12211 Research Triangle Park, NC 27709-2211		10. SPONSORING / MONITORING AGENCY REPORT NUMBER 37304.5-EG	
11. SUPPLEMENTARY NOTES The views, opinions and/or findings contained in this report are those of the author(s) and should not be construed as an official Department of the Army position, policy or decision, unless so designated by other documentation.			
12 a. DISTRIBUTION / AVAILABILITY STATEMENT Approved for public release; distribution unlimited.		12 b. DISTRIBUTION CODE	
13. ABSTRACT (Maximum 200 words) <p>Models have been developed to assess flowfields inside diesel injector orifice passages in order to increase our understanding of the spray formation process which governs performance and emissions in these engines. Fully viscous, unsteady, and two-phase codes have been developed to analyze 2-D and 3-D flows and the effect of turbulence has also been incorporated in the 2-D models. A series of parametric studies have been conducted to characterize unsteadiness in the flow brought about by instabilities of the vena-contracta formed downstream of the orifice inlet lip. Turbulence effects have been investigated extensively and the production of turbulence in the bubble collapse region is evident in the simulations. Including the effects of turbulence improves predictions of the extent of the two-phase region. Large three-dimensional simulations have been conducted to reflect the asymmetric inlet conditions realized in today's diesel injectors. The crossflow which is present at the inlet lip has a dramatic impact on the extent of the cavity and the massflow/velocity distribution at the exit of the orifice. Vortices are formed at the inlet lip; these structures persist the entire length of the passage. The structures elucidated by the calculations have also been observed experimentally in recent work from Delphi Systems. These works have shown that the vortices persist into the spray itself and therefore the simulation of the orifice flow does provide a good predictive tool for subsequent spray development.</p>			
14. SUBJECT TERMS Cavitating flows, computational fluid dynamics, atomization		15. NUMBER OF PAGES 93	
		16. PRICE CODE C	
17. SECURITY CLASSIFICATION OR REPORT UNCLASSIFIED	18. SECURITY CLASSIFICATION ON THIS PAGE UNCLASSIFIED	19. SECURITY CLASSIFICATION OF ABSTRACT UNCLASSIFIED	20. LIMITATION OF ABSTRACT UL

NSN 7540-01-280-5500

Standard Form 298 (Rev.2-89)  
Prescribed by ANSI Std. Z39-18  
298-102

20010831 009

**MASTER COPY:** PLEASE KEEP THIS "MEMORANDUM OF TRANSMITTAL" BLANK FOR REPRODUCTION PURPOSES. WHEN REPORTS ARE GENERATED UNDER THE ARO SPONSORSHIP, FORWARD A COMPLETED COPY OF THIS FORM WITH EACH REPORT SHIPMENT TO THE ARO. THIS WILL ASSURE PROPER IDENTIFICATION. NOT TO BE USED FOR INTERIM PROGRESS REPORTS; SEE PAGE 2 FOR INTERIM PROGRESS REPORT INSTRUCTIONS.

**MEMORANDUM OF TRANSMITTAL**

U.S. Army Research Office  
ATTN: AMSRL-RO-BI (TR)  
P.O. Box 12211  
Research Triangle Park, NC 27709-2211

- |  |   |
|--|---|
| <input type="checkbox"/> Reprint (Orig + 2 copies) | <input type="checkbox"/> Technical Report (Orig + 2 copies)                 |
| <input type="checkbox"/> Manuscript (1 copy)       | <input checked="" type="checkbox"/> Final Progress Report (Orig + 2 copies) |
|  | <input type="checkbox"/> Related Materials, Abstracts, Theses (1 copy)      |


CONTRACT/GRANT NUMBER: DAAG55-98-1-0318

REPORT TITLE: Modeling Diesel Engine Injector Flows

is forwarded for your information.

SUBMITTED FOR PUBLICATION TO (applicable only if report is manuscript):

Sincerely,

  
Gregory A. Bradell

DAAG55-98-1-0318

## MODELING DIESEL ENGINE INJECTOR FLOWS

Stephen D. Heister, Professor  
Gregory A. Blaisdell, Associate Professor  
School of Aeronautics and Astronautics  
Purdue University  
1282 Grissom Hall  
West Lafayette, IN 47907

1 August 2001

Final Technical Report for Period 20 May 1998 - 31 May 2001

Approved for Public Release, Distribution is Unlimited
---

Prepared for:  
U. S. Army Research Office P. O. Box 12211 Research Triangle Park, NC 27709-2211

## Foreword

This research program has focused on enhancing the understanding of the internal flows in injector passages and their contributions to the subsequent spray formation outside the orifice. During the past three years, progress has been made in the following aspects. First, the investigation of the unsteadiness in orifice massflow caused by the hydrodynamic instability of the vena-contracta or the presence of cavitation in this region through a parametric study of an axisymmetric orifice. Second, the  $k - \omega$  turbulence model and the homogeneous pseudo density model has been combined to approximate two-dimensional and axisymmetric turbulent cavitating flows. Although, the turbulence model generate a steady attached cavity at the inlet corner, it shows an improvement in the prediction of mass flow through an orifice. Finally, three dimensional laminar calculations were conducted to provide a better understanding of cross-flow effects. The effect of cross flow velocity on orifice mass flow is investigated and the three dimensional model predicts a satisfactory results compared with experimental measurements.

# Contents

<b>1</b>	<b>Research Objectives</b>	<b>1</b>
<b>2</b>	<b>Summary of The Most Important Results</b>	<b>1</b>
2.1	Laminar Parametric Study on an Axisymmetric Orifice . . . . .	1
2.1.1	Unsteadiness in Massflow and Cavitation Length . . . . .	2
2.1.2	Effect of Inlet Rounding . . . . .	2
2.2	Turbulent Injector Internal Flows . . . . .	3
2.2.1	Discharge Coefficient Prediction . . . . .	3
2.2.2	Cavitation Extent Comparison . . . . .	4
2.2.3	Turbulent Kinetic Energy (TKE) . . . . .	5
2.3	The Effect of Cross Flow . . . . .	5
2.3.1	Discharge Coefficient . . . . .	5
2.3.2	Internal Flow Structure . . . . .	5
<b>3</b>	<b>Technology Transfer</b>	<b>8</b>
<b>4</b>	<b>Publications</b>	<b>9</b>
<b>5</b>	<b>Participants</b>	<b>9</b>
<b>6</b>	<b>Bibliography</b>	<b>9</b>
<b>7</b>	<b>Appendix A - On the Influence of Internal Flow Structure on Performance of Plain-Orifice Atomizers</b>	<b>11</b>
<b>8</b>	<b>Appendix B - 2D and Axisymmetric Turbulent, Cavitating Flow Simulations</b>	<b>34</b>
<b>9</b>	<b>Appendix C - 3D Cavitating Flow Simulations</b>	<b>74</b>

## List of Figures

1	Computational domain and mesh for orifice flow. . . . .	1
2	Typical quasi-periodic behavior of cavitation length $L_C$ and orifice discharge coefficient $C_D$ .	2
3	Frequency of discharge coefficient ( $f_D$ ) and cavitation length ( $f_C$ ) vs. cavitation number; $L/D = 8, P_2 = 1$ atm. . . . .	3
4	The effect of inlet rounding on the fluctuation of discharge coefficient $\Delta C_D$ and its mean value $\overline{C_D}$ . . . . .	3
5	Discharge coefficient $C_D$ comparison with experimental results; $L/D = 6, D = 3.18mm$ ; and the comparison of velocity profile at the exit for laminar and turbulent solutions . . . . .	4
6	Overlays of numerical results and photographic time shot of cavitation region, ( $\Delta P \approx 36psi, L/D =$ $10.714$ ). Here, $\rho = 0.98$ on the outermost contour with gradients of 0.2 between contours . . .	4
7	Turbulence intensities and mass-averaged Reynolds stress comparison with experimental re- sults at different axial locations, with and without cavitation (turbulent calculation) . . . . .	6
8	3-D manifold cross flow model and key parameters . . . . .	7
9	The effect of cross flow velocity on discharge coefficient and the comparison with experiment measurement . . . . .	7
10	Experimental snapshots of vortex structure inside an orifice (on the left) and of diesel sprays (on the right). [From Soteriou et al. <sup>[16]</sup> , used by permission] . . . . .	8
11	Vortex structure inside the orifice under cavitating ( $K = 1.2$ on the left) and non-cavitating ( $K = 6.0$ , on the right) conditions, $V_1 = 6.0m/s$ . Green lines are vortex lines outlined parallel to local vorticity vector. . . . .	8

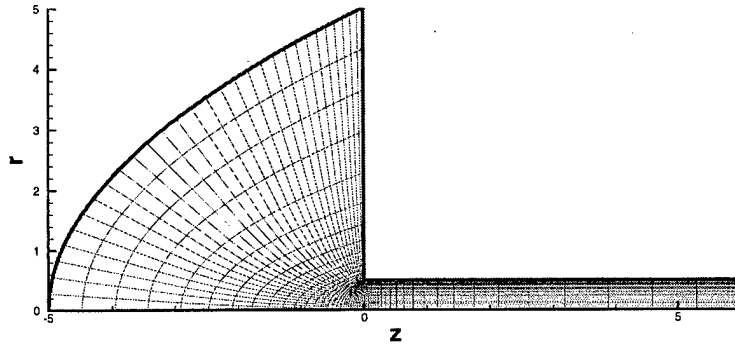


Figure 1: Computational domain and mesh for orifice flow.

## 1 Research Objectives

Notable changes in spray structure are evident under the variations of the cavitation extent inside the injector passage [1,2,3]. Hence, the understanding of the complex cavitation phenomena present in an injector passage is fundamental to the subsequent jet atomization. For this purpose, a focused research effort has been conducted to develop models capable of providing quantitative information regarding the cavitation process. The models have centered on the use of Marker and Cell finite volume method as a means to provide accurate description of the complex, and arbitrary unsteady conditions.

The homogeneous pseudo density model, developed by Chen and Heister [4,5], which describes the non-equilibrium interaction between liquid and bubbles provides the basis of this research. It assumes two phases to be fully mixed on the sub-grid level and the local density is a measure of void fraction. This simplification circumvents the great challenge of tracing each individual bubble which is implausible at current stage, but instead focuses on the global/integral dynamics of bubble clusters. Based on this pseudo density formulation, a series of CFD program have been developed with increasing physics and complexity: (1) two-dimensional and axisymmetric laminar [4,6], (2) two-dimensional and axisymmetric turbulent [7], (3) three-dimensional laminar [8]. These CFD programs were used to predict the evolution of cavitation and its effect on orifice mass flow.

## 2 Summary of The Most Important Results

Three major tasks have been accomplished during the three years research program. The unsteady effect of the instability of the vena-contracta or cavitation in this region on massflow is addressed in Section 3.1. The influence of cavitation on flow turbulence, and turbulent orifice/slot internal flow is described in Section 3.2. Finally, the results from an unsteady three-dimensional two-phase model are provided in Section 3.3.

Figure 1 shows a typical mesh for an axisymmetric orifice or a two-dimensional slot. Grid refinement study were performed for both laminar and turbulent calculations. It is verified that a mesh employing 140 grid points in the axial direction and 60 points in the radial direction is adequate to resolve salient flow-field structures for laminar calculation [6]. For turbulent calculation the number of grid points in radial direction is increased to 90. Constant pressure boundary conditions are imposed on inflow and outflow boundaries; no-slip conditions are imposed along walls, and symmetry conditions are imposed along the centerline. To approximate the velocity at the inflow boundary, we employ a sink at the origin. The strength of the sink is updated during each time step by the conservation of mass flow rate through the nozzle passage.

### 2.1 Laminar Parametric Study on an Axisymmetric Orifice

A series laminar simulations were conducted to assess the unsteady flow perturbations brought about by the vena-contracta in single and two-phase regimes. The influence of Reynolds number, supply pressure,

discharge pressure, orifice  $L/D$  and inlet rounding have been investigated. In this report, the unsteadiness in orifice massflow and the effect of inlet rounding are described.

### 2.1.1 Unsteadiness in Massflow and Cavitation Length

The predicted orifice massflow characteristics shows a quasi-periodic oscillation under both cavitating and non-cavitating conditions. Under the presence of cavitation, the oscillation of the extent of cavitation region is the primary reason that causes the unsteadiness of the massflow through orifice. Figure 2 shows the time history of cavitation length ( $L_C$ ) and discharge coefficient ( $C_D$ ) for a typical cavitating conditions.

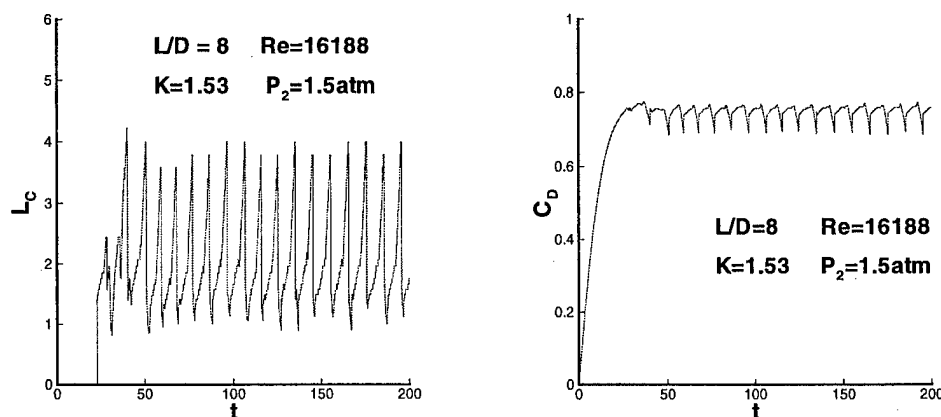


Figure 2: Typical quasi-periodic behavior of cavitation length  $L_C$  and orifice discharge coefficient  $C_D$

By performing a Fourier transform on the  $L_C$  and  $C_D$  histories, one can obtain the principle frequency of oscillation of each of these parameters,  $f_C$  and  $f_D$ . We should point out that the Fourier transforms typically show energy in 2-3 discrete frequencies<sup>[9,10]</sup>. The bulk of the energy is contained in the primary harmonic, other frequencies which appear to be higher harmonics tend to contain much less energy. In addition, the oscillation of  $L_C$  and  $C_D$  is coupled tightly. This point is evidenced in figure 3 which shows the change in  $f_C$  and  $f_D$  with variations in  $K$  at fixed Reynolds number for an orifice with  $L/D = 8$ . The point of cavitation inception is shown on the figure; the region to the left of this point is where cavitation is evident in the flow field. Note in the plot,  $f_C$  and  $f_D$  are almost identical under the presence of cavitation.

It may be possible to make use of this result to design passive oscillations of a desired frequency. In general, the frequencies are consistent with the time it takes a fluid element to traverse the length of the orifice passage. Atomizers which produce fine sprays tend to produce droplets at much higher frequencies than those noted in figure 3. Partial cavitation may be used to "pump" instabilities for atomizers operating at more modest pressure drops such as a flow produced in inkjet printing applications.

### 2.1.2 Effect of Inlet Rounding

Several experiments and numerical simulations<sup>[5]</sup> have noted that inlet rounding can delay the occurrence of cavitation and increase discharge coefficient through reductions in contraction losses. However, the effects of rounding on the unsteady behavior has not been investigated in any great detail. For this reason, the unsteady characteristics have been studied assuming the inlet is rounded with a given radius circle. Figure 4 depicts the level of massflow variations at various cavitation numbers for three levels of inlet rounding ( $r/R = 0, 0.05, 0.1$ ) and the change of average discharge coefficient vs. inlet rounding at fixed cavitation number  $K = 1.56$ . The cavitation onset point is noted on the left plot; cavitating results lie to the left of this point since decreasing  $K$  corresponds to increased supply pressure. Results in the figures show that massflow variations are reduced dramatically for even a small amount of inlet rounding, while the average mass flow rate is increased.



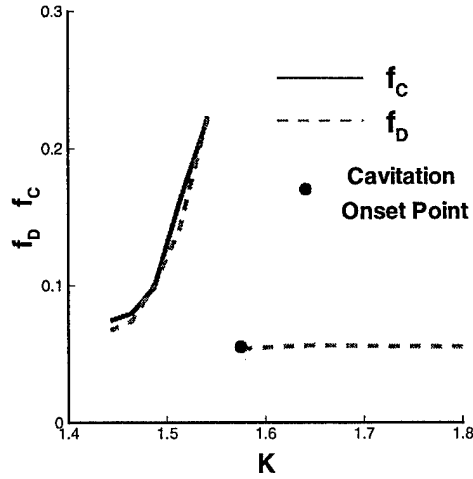


Figure 3: Frequency of discharge coefficient ( $f_D$ ) and cavitation length ( $f_C$ ) vs. cavitation number;  $L/D = 8$ ,  $P_2 = 1$  atm.

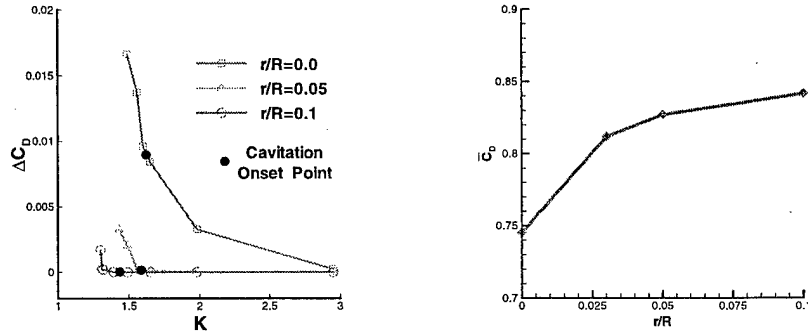


Figure 4: The effect of inlet rounding on the fluctuation of discharge coefficient  $\Delta C_D$  and its mean value  $\bar{C}_D$

## 2.2 Turbulent Injector Internal Flows

A few axisymmetric turbulent simulations were made and the predicted discharge coefficient is compared with the measurements by Nurick<sup>[11]</sup>. The two dimensional code was used to assess the turbulent cavitating flow through a slot. The computed cavitation extension and turbulent quantities is compared with available experimental measurements. The results are described in the following sections.

### 2.2.1 Discharge Coefficient Prediction

Figure 5 shows the results of the discharge coefficient comparison on an orifice of  $L/D = 6$ ,  $D = 3.18\text{mm}$  under a back pressure of  $P_2 = 13.8\text{psi}$ . In the figure, "Lam1" represents a laminar calculation without sink-inflow velocity boundary condition, "Lam2" represents a laminar calculation with an approximated inflow velocity from an artificial sink as described in the previous section, and the line denoted as "Turb" is calculated from the turbulence model. As shown in the plot, the sink-inflow velocity treatment greatly improves the prediction of discharge coefficient. There is an increase in the magnitude of  $C_D$  of 4.7% over the zero inflow velocity treatment. The turbulence model shows a further improvement and gives results somewhat closer to the experimental data. The differences between the turbulence model and laminar predictions on  $C_D$  might be explained by the exit velocity profiles from both types calculation. The turbulent

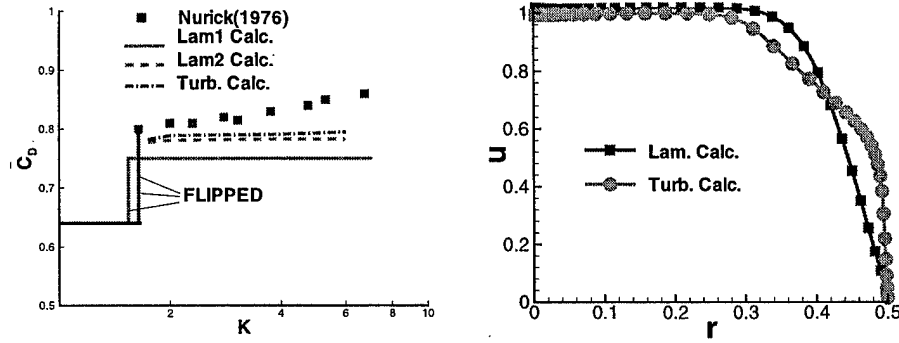


Figure 5: Discharge coefficient  $C_D$  comparison with experimental results;  $L/D = 6$ ,  $D = 3.18mm$ ; and the comparison of velocity profile at the exit for laminar and turbulent solutions

velocity profile is fuller than the laminar one. Due to this feature, the turbulence model yields a larger  $C_D$  by 1.6%. In the calculations a sharp-edged inlet is assumed, however the amount of inlet rounding on the experimental hardware is not known. As indicated in figure 4 small degree of inlet rounding can lead to substantial increase in discharge coefficient. It is estimated that an inlet rounding less than 0.025 would be sufficient for the laminar model to generate a discharge coefficient that is high enough to match the measurement. This factor might be the primary reason for the model's consistent underprediction of discharge coefficient.

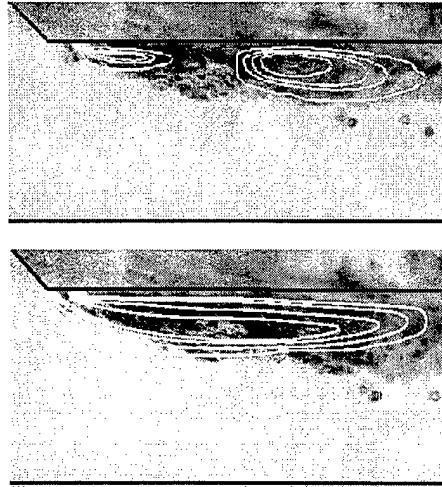


Figure 6: Overlays of numerical results and photographic time shot of cavitation region, ( $\Delta P \approx 36psi$ ,  $L/D = 10.714$ ). Here,  $\rho = 0.98$  on the outermost contour with gradients of 0.2 between contours

### 2.2.2 Cavitation Extent Comparison

The 2-D code was used to simulate the flow through slots with the geometry used by Henry<sup>[9]</sup> and Sanchez<sup>[12]</sup>. Although the turbulent code produces a constant value of the cavitation length, the turbulent calculation generates a single contiguous cavitation region near the inlet corner, consistent with experimental observation. Figure 6 shows density contours, which denote the cavity region, obtained from laminar (the upper one) and turbulent (the lower one) calculations, overlaying one photographic snapshot by Henry<sup>[9]</sup>. Although the laminar simulation results in an overall cavitation extent consistent with experiment, it indicates two separate regions of cavitation. The turbulence model improves on this point by generating a single cavitation region which appears to be quite consistent with experimental results both in axial and cross-stream directions.

### 2.2.3 Turbulent Kinetic Energy (TKE)

The turbulence model predicts highest TKE at the rear end of cavity region, the wake of the cavity, for all operating conditions. It is known that the wake where bubble detachment and collapses accompanied with pressure recovery occurs is the most dynamic region. The computed turbulence quantity is compared with the measurement of Ruiz and He<sup>[13]</sup>. Figure 7 shows turbulence intensities in the streamwise and normal direction and Reynolds shear stress as well as the experimental data at different streamwise locations. Here,  $R_{xx}^{\frac{1}{2}} = \sqrt{\rho u'' u''}$  and  $R_{yy}^{\frac{1}{2}} = \sqrt{\rho v'' v''}$ , representing turbulence intensity in  $x$  and  $y$  directions are the dimensionless mass weighted velocity fluctuation in streamwise and normal directions, and  $R_{xy} = \overline{\rho u'' v''}$  is the mass averaged Reynolds shear stress. The cavitation extent is also shown in this plot.

Near the rear end of cavity region the calculation predicts  $R_{xx}^{\frac{1}{2}}$ ,  $R_{yy}^{\frac{1}{2}}$  and  $R_{xy}$  are slightly larger under cavitating conditions than under non-cavitating conditions due to flow reattachment. It should be mentioned the  $k - \omega$  model does not include any production terms due to bubble collapse. The only mechanism to capture turbulence generation for the turbulence model is the occurrence of a strong strain rate. However, due to the presence of cavitation the pseudo density model produces a larger strain rate flow field. It has been observed that the collapse of bubbles is a source of vortex generation<sup>[14]</sup>.

## 2.3 The Effect of Cross Flow

The fully three-dimensional two-phase Navier-Stokes solver is utilized to simulate an orifice flow driven by the cross flow in a manifold. Figure 8 shows the schematic representation of the three-dimensional manifold cross flow. In the figure,  $V_1$  is the cross flow velocity, and  $V_2$  is ideal discharge velocity at the exit, calculated from Bernoulli's equation. The effect of the cross flow velocity on cavitation length and discharge coefficient are investigated. The computed discharge coefficient is compared with Strakey and Talley's<sup>[15]</sup> measurement.

### 2.3.1 Discharge Coefficient

Figure 9 shows the comparison of the computed average discharge coefficient and the experimentally measured discharge coefficient. Note the average value is obtained by sampling the data after it reaches a steady oscillation state. Although the number of computed data is fewer than that of the experimental results because of the high expense of the computation, two patterns can still be observed from the plot. First, for a given cross flow velocity, as cavitation number increases the discharge coefficient increases at first. After reaching the maximum value, discharge coefficient then begins to drop off. The maximum value in discharge coefficient occurs when the cavitation number is about 1.8, a value close to the experimentally measured inception index. The reason for that is the following. The mass flow rate is proportional to the pressure drop through the orifice (increasing with decreasing cavitation number) before the inception of cavitation. When the pressure loss is large enough to cause cavitation to occur, the mass flow rate begins to drop due to the slipstream effect of the cavity as pointed out by Bunnell and Heister<sup>[8]</sup>. The more significant cavitation becomes, the lower the mass flow rate is. The limited computed data samples reproduce this feature as the experimental counterparts do, except that they overpredict the discharge coefficient in general, especially when  $V_1 = 8.9m/s$  and  $K = 6.0$ . The overprediction might be due to the lack of turbulence in the modeling or because the grid is not fine enough<sup>[8]</sup>.

The second trend observed in figure 9 is with regard to the effect of cross flow velocity. Both the computation and experiment show that as cross velocity increases, discharge coefficient decreases. This phenomenon can be attributed to the increase in velocity ratio, the ratio of the cross flow velocity to the ideal orifice discharge velocity  $V_1/V_2$ <sup>[15]</sup>. With increasing velocity ratio, less amount of fluid passes through the orifice.

### 2.3.2 Internal Flow Structure

Soteriou et al.<sup>[16]</sup> have found strong vortex structures exist inside the orifice when cavitation occurs based on their observation on a large scale nozzle. Vortex interaction can also be observed under non-cavitating conditions. The vortices inside the nozzle sometimes intertwine with each other. Figure 10 shows the photographic shot of a vortex intertwining structure inside an orifice, and the vortex structure of a diesel

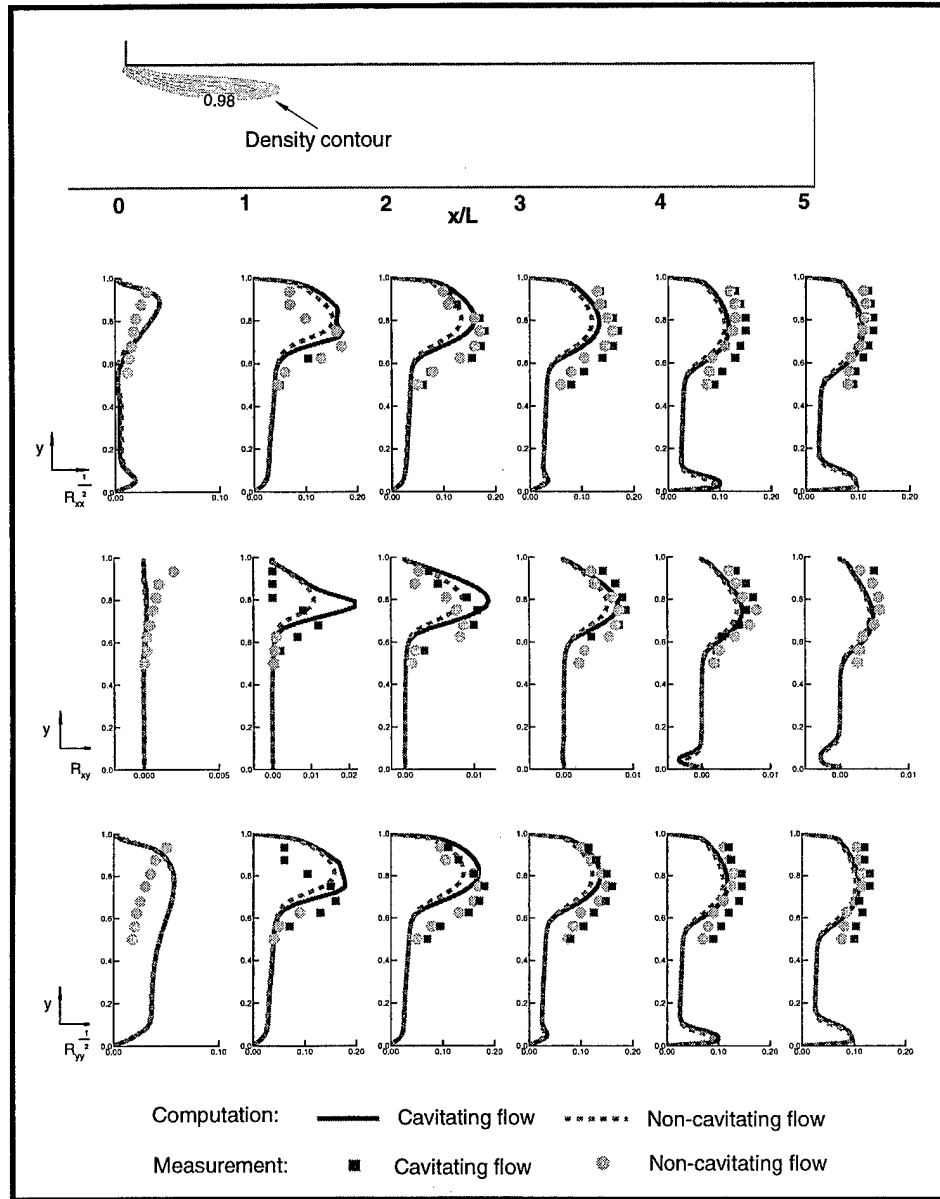


Figure 7: Turbulence intensities and mass-averaged Reynolds stress comparison with experimental results at different axial locations, with and without cavitation (turbulent calculation)

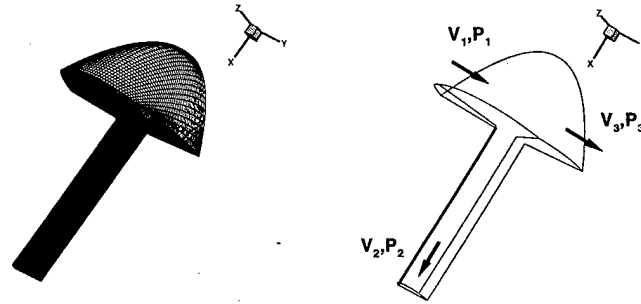


Figure 8: 3-D manifold cross flow model and key parameters

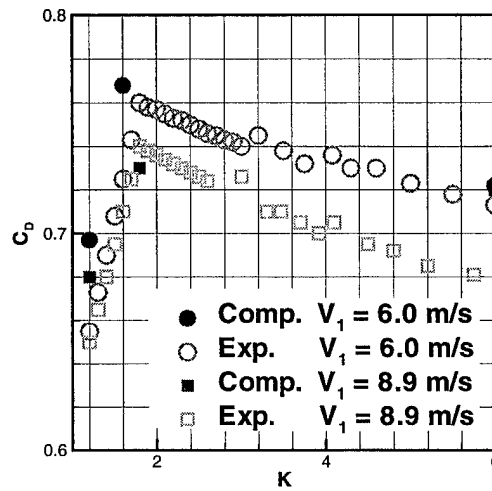


Figure 9: The effect of cross flow velocity on discharge coefficient and the comparison with experiment measurement

spray. Contrary to the traditional theory that the aerodynamic interfacial shear is the dominant force that causes the breakup of the fuel injected from the orifice, Soteriou et al. indicated that the primary factors inducing atomization are associated with the characteristics of the internal flow inside the nozzle.

Figure 11 shows the various computed vortex lines inside the orifice at one instant in time for the conditions with and without cavitation. At other instants, both flow conditions show a vortex structure similar to what are shown in these two figures. As seen from the figure, the difference between the vortex structure under cavitating condition and that under non-cavitating condition is significant. For non-cavitating case, in the front section of the orifice, the cross or vertical components of the vorticity are dominant. The few vortex lines shown in the figure are nearly parallel to each other and perpendicular to streamwise direction. Based on these representing vortex lines, we believe vortex sheet-like structures exist near the wall region in the front section of the orifice. In the rear section of orifice, the streamwise component of the vorticity start to be dominant. The vortex sheet starts to roll up and several vertex lines intertwine and form a strong vortex structure on the windward side of orifice. For the flow with cavitation, vortex interaction begins earlier on the leeward side and two primary vortex structures are formed at the exit of orifice. These vortex structures indicates that swirls with rotating axis in line with streamwise direction exist at the exit.

The role played by the internal vortex structure on spray atomization is not well understood since it is both a numerical and an experimental new discovery. Recently some authors<sup>[2,3,16]</sup> have suggested that cavitation inside the orifice is an important factor that promotes atomization. This might be attributed to

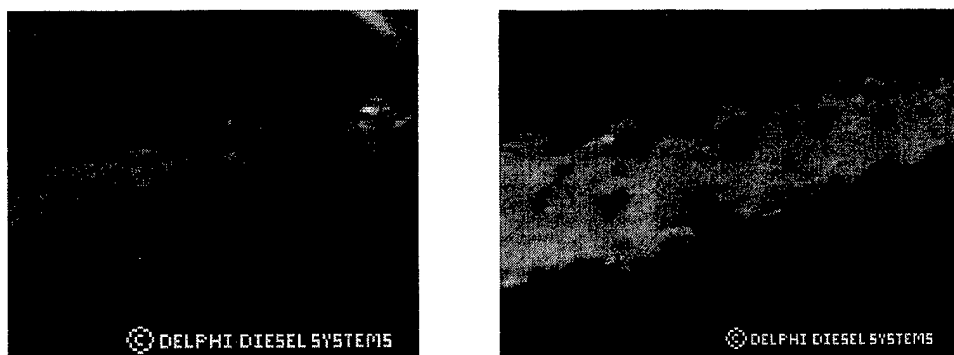


Figure 10: Experimental snapshots of vortex structure inside an orifice (on the left) and of diesel sprays (on the right). [From Soteriou et al.<sup>[16]</sup>, used by permission]

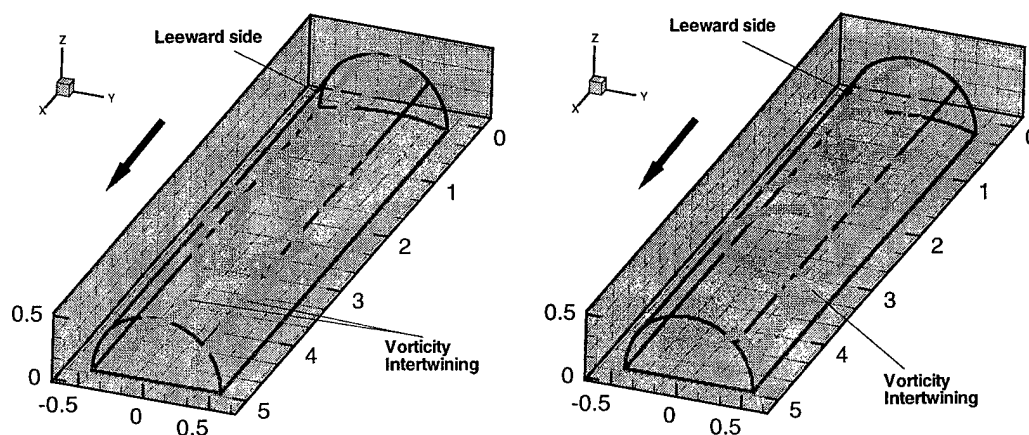


Figure 11: Vortex structure inside the orifice under cavitating ( $K = 1.2$  on the left) and non-cavitating ( $K = 6.0$ , on the right) conditions,  $V_1 = 6.0 \text{ m/s}$ . Green lines are vortex lines outlined parallel to local vorticity vector.

the difference made by cavitation on the internal flow structure and the magnitude of the vorticity vector at the exit plane. The simulation shows that there is a stronger swirl on the leeward side for cavitating flow. Once the fuel flows out of the orifice, without the constraint of the wall boundary the stronger velocity components in cross and vertical directions tend to cause the jet to break up earlier.

### 3 Technology Transfer

We continue to work closely with Cummins Engines in transferring results from this research to the field. In late 1999, we completed a series of fully 3-D unsteady calculations of one of Cummins injector designs. These demanding calculations were not totally coupled to the inflow from the injector plunger and we have plans to continue the work to include this coupling. We have also had several conversations with officials at Detroit Diesel and Catapiller at national meetings and continue to inform the community of our findings. Politically, it is difficult for us to work directly with these other organizations due to conflict of interest concerns by Cummins.

## 4 Publications

- Xu, C., Bunnell, R. A., Heister, S. D., "On the Influence of Internal Flow Structure On Performance of Plain-Orifice Atomizers," *Atomization and Sprays*, accepted.
- Xu, C., Blaisdell, G. A., Heister, S. D., "Simulations of Turbulent Cavitating Internal Flows," in Proceedings of Multiphase Flow 2001, Orlando, Florida, USA, March 2001.
- Xu, C., Bunnell, R. A., Heister, S. D., Tuan, T. L., "On the Influence of Internal Flow Structure On Performance of Plain-Orifice Atomizers," in Proceedings of ICLASS-2000, Pasadena, CA, USA, July 2000.

## 5 Participants

- Steven D. Heister, Professor, Purdue University
- Gregory A. Blaidell, Associate Professor, Purdue University
- Changhai Xu, Research Assitant, Purdue University, expected doctorate degree in December 2001.

## 6 Bibliography

1. Bergwerk, W., "Flow Pattern in Diesel Nozzle Spray Holes," *Procs. Instn. Mech. Engrs.*, Vol. 173, pp. 655-660, 1959.
2. Hiroyasu, H., "Spray Breakup Mechanism From The Hole-Type Nozzle And Its Applications," *Atomization and Sprays*, Vol. 10, pp. 511-527, 2000
3. Tamaki, N., Shimizu, M., Mishida, K. and Hiroyasu, H., "Effects of Cavitation and Internal Flow on Atomization of A Liquid Jet," *Atomization and Sprays*, Vol. 8, pp. 179-197, 1998
4. Chen, Y., and Heister, S. D., "Modeling Hydrodynamic Non-Equilibrium in Bubbly and Cavitating Flows," *Journal of Fluids Engineering*, Vol. 118, No. 1, pp. 172-178, 1995.
5. Chen, Y. and Heister, S. D., "Modeling Cavitating Flows in Diesel Injectors," *Atomization and Sprays*, Vol. 6, pp. 709-726, 1996.
6. Bunnell, R. A., Heister, S. D., Yen, C. and Collicott, S. H., "Cavitating Injector Flows: Validation of Numerical Models and Simulations of Pressure Atomizers," *Atomization and Sprays*, Vol. 9, pp. 445-465, 1999.
7. Xu, C., *Simulation of Orifice Internal Flows Including Cavitation And Turbulence*, Ph.D. Thesis, School of Aeronautics and Astronautics, Purdue University, West Lafayette, IN, August 2001.
8. Bunnell, R. A., Heister, S. D., "Three-Dimensional Unsteady Simulation of Cavitating Flows in Injector Passages," *Journal of Fluids Engineering*, Vol. 122, pp. 791-797, 2000.
9. Henry, M. E., *An Experimental Investigation of a Cavitation Slot Orifice*, MS. Thesis, School of Aeronautics and Astronautics, Purdue University, West Lafayette, IN, May 1997.
10. Chandra, B. W. and Collicott, S. H., "Experimental Investigation of Cavitation Frequency in A Slot Orifice," ILASS-99 Conference Proceedings, pp. 379-384, Indianapolis, IN 1999.
11. Nurick, W. H., "Orifice Cavitation and Its Effect on Spray Mixing," *Journal of Fluids Engineering*, December, pp. 681-687, 1976.
12. Sanchez, P. K., *Rigorous Investigation Of Cavitation In A 2-D Slot Orifice*, MS. Thesis, School of Aeronautics and Astronautics, Purdue University, West Lafayette, IN, May 1997.

13. Ruiz, F. and He, L., "Turbulence Under Quasi-Cavitating Conditions: A New Species," *Atomization and Sprays*, Vol. 9, pp.419-429, 1999.
14. Kubota, A., H. Kato, and H. Yamaguchi, "A New Modeling of Cavitating Flows: A Numerical Study of Unsteady Cavitation on a Hydrofoil Section," *Journal of Fluid Mechanics*, Vol. 240, pp.59-96, 1992.
15. Strakey, P. A., Talley, D. G., "The effect of manifold cross-flow on the discharge coefficient of sharp-edged orifices," *Atomization and Sprays*, Vol. 9, No.1, 1999.
16. Soteriou, C., Andrews, R., Torres, N., Smith, M. and Kunkulagunta, R., "Through the Diesel Nozzle Hole - a Journey of Discovery," CLASS-2001 Conference Proceedings, Dearborn, Michigan, USA, 1999.



## **7 Appendix A - On the Influence of Internal Flow Structure on Performance of Plain-Orifice Atomizers**

Xu, C., Bunnell, R. A., and Heister, S. D., *"Atomization and Sprays"*, *Accepted*.

# On the Influence of Internal Flow Structure on Performance of Plain-Orifice Atomizers

Changhai Xu \*, R. A. Bunnell\* and S. D. Heister†

\* Graduate Research Assistant

† Professor, School of Aeronautics and Astronautics, Purdue University, W. Lafayette, IN

## Abstract

A series of parametric simulations have been conducted to investigate the unsteady internal flow behavior in plain orifice, or "pressure" atomizers. The unsteady behavior is attributed to instabilities in the vena contracta and the presence of cavitation in this region. Even though the present calculations are laminar, they exhibit turbulent-like characteristics due to this instability. Orifice massflow is shown to be periodic in most instances with fluctuations occurring at frequencies consistent with the orifice transit time. Cavitation is shown to enhance fluctuations; in some cases quite dramatically. Results are presented for a range of flow conditions and orifice geometries.

## Introduction

The plain-orifice, or pressure atomizer represents the simplest solution for atomizing liquids in many applications. By simply drilling a small hole in a piece of material, adequate atomization can be obtained in many instances for fluids of low or modest viscosity. For this reason, the pressure atomizer has very wide usage and has been the subject of research studies for well over 100 years<sup>1</sup>. Innumerable works have focused on the droplet/spray produced by these devices and modern instrumentation provides accurate measures of droplet sizes and velocities in dilute regions downstream from the orifice exit.

It has long been recognized the design of the orifice flow passage (both length and diameter) has important implications on the type of spray pattern produced by the orifice<sup>2,3</sup>. Through changes in orifice design, a high pressure drop atomizer can be manufactured to produce a very fine spray or a water-jet cutter. The tendency for the flow to cavitate on the inner orifice lip has also been inferred as a basic atomization mechanism by some authors<sup>3-5</sup>. These factors have led numerous researchers to begin to study both experimentally<sup>5-15</sup>, and analytically<sup>16-22</sup> the flow pattern inside the orifice passage in hopes to gain insight on its effect on spray attributes.

Motivated primarily by the diesel injector application, recent efforts have focused on the impact of cavitation on internal flow and spray characteristics. Figure 1 highlights the simple geometry for a typical pressure atomizer with upstream and downstream pressures,  $P_1$  and  $P_2$ , respectively. The large fluid acceleration near the inlet lip leads to a locally low pressure region; a vena-contracta is formed and cavitation will first appear in this area. Numerous experiments have shown the cavitation region to be inherently unsteady; the collapsing bubbles at the aft end to the region cause local pressure rises which are fed upstream and effect

subsequent shapes of the cavity. Recent experiments<sup>15</sup> have shown that this “partial cavitation” behavior enhances instabilities in the jet produced by the orifice thereby promoting atomization.

Even under non-cavitated conditions, the vena-contracta is still present and is subject to instabilities arising from the abrupt pressure rise at the end of the recirculation zone. As the pressure drop  $P_1 - P_2$  increases, the flow in the passage will eventually reach the hydraulic flip condition in which the vena contracta extends the entire length of the orifice. Notable changes in spray structure are evident under these conditions; atomization is generally much poorer than under partial cavitation conditions.

Numerical modeling of these orifice flows is challenging because one must normally account for unsteadiness and the possibility of cavitation within the passage. Recently, several authors<sup>16,17,19,22</sup> have approached this problem with a homogeneous, or “pseudo-density” formulation in which the single phase Navier Stokes equations are solved on a fixed computational mesh. An additional constitutive relation is required for the pseudo-density in these schemes. These schemes are powerful in that they can normally provide economical calculations of flows in which there are simply too many bubbles to track individually.

In this paper, we apply a recently developed homogeneous flow model to assess the unsteady flow perturbations brought about by the vena-contracta in single and two-phase flow regimes. The following section provides a brief description of the model and its validation against experimental data. A large number of parametric simulations are then summarized, followed by conclusion from the studies.

## Modeling Description

Since the numerical model has been described in great detail in other works<sup>19–21</sup>, we will provide just a brief overview here. We assume a laminar, axisymmetric, incompressible flow and solve the Navier-Stokes equations on a fixed structured mesh using the Marker and Cell algorithm. Liquid density ( $\rho_l$ ), the “Bernoulli” velocity in the orifice ( $v = \sqrt{2(P_1 - P_2)/\rho_l}$ ), and the orifice diameter ( $D$ ) are chosen as dimensions. In this case, the two dimensionless parameters are the Reynolds number ( $Re$ ) and cavitation number ( $K$ ):

$$Re = \frac{\rho_l v D}{\mu_l} \quad K = \frac{P_1 - P_v}{P_1 - P_2} \quad (1)$$

where  $P_v$  is the fluid vapor pressure and  $\mu_l$  is the liquid viscosity. The viscosity in the two-phase mixture is generally based on the local void fraction<sup>19</sup>,  $\alpha$ :

$$\mu = \alpha \mu_g + (1 - \alpha) \mu_l \quad (2)$$

Since  $\mu_g \ll \mu_l$  and  $\rho_g \ll \rho_l$  for most liquid/vapor mixtures, we can effectively neglect the influence of gas phase viscosity. Under these assumptions, the pseudo-density of the mixture is  $\rho = 1 - \alpha$  and Eq. 2 becomes:

$$\mu = \rho \mu_l \quad (3)$$

Figure 2 shows a typical mesh for an orifice  $L/D=6$ . The mesh employed 140 grid points in the axial direction and 60 points in the radial direction. Recent grid convergence studies have verified that this mesh

is adequate to resolve salient flowfield structures<sup>21</sup> for non-cavitating or cavitating flows. Constant pressure boundary conditions are imposed on inflow and outflow boundaries; no-slip conditions are used along walls, and symmetry conditions are imposed along the orifice centerline.

The two-phase treatment requires a constitutive relation for the pseudo-density,  $\rho$ , in order to obtain closure for the governing equations. The current treatment<sup>19</sup> is based on the dynamic response of a monodisperse bubble field to changes in pressure and inertial forces per the Rayleigh-Plesset equation. The treatment neglects surface tension, bubble coalescence, bubble breakup, and slip between phases. However, the approach does apply for arbitrary void fraction (or pseudo-density) and we do not assume a disperse bubble field used by many researchers. These assumptions greatly simplify the physics of the flow, but still provide a gross response to the spatial and time varying pressure field. The resulting constitutive relation takes on a form similar to the Rayleigh-Plesset equation in that changes in pseudo-density are governed by pressure and inertial forces:

$$\frac{D^2\rho}{Dt^2} = \frac{6\alpha'(1+\alpha'+\alpha'^2)^2}{L_0^2(2+\alpha')(1-\alpha'^3)^{\frac{1}{3}}}(P-P_v) + \left[ \frac{11\alpha'^3 - \alpha'^2 - \alpha' - 1}{6\alpha'^3(1-\alpha'^3)} - \frac{1+4\alpha'+\alpha'^2}{6\alpha'^2(2+\alpha')(1+\alpha'+\alpha'^2)} \right] \left( \frac{D\rho}{Dt} \right)^2 \quad (4)$$

Here,  $\alpha' = \sqrt[3]{1-\rho}$ , and  $P$  is the local pressure returned by the Navier-Stokes solver. Finally, in Eq. 4  $L_0$  is a *non-dimensional* characteristic length scale:

$$L_0^2 = \left( \frac{3}{4\pi n_o} \right)^{\frac{2}{3}} \quad (5)$$

Here,  $n_o$  is the non-dimensional site density. Letting the dimensional site density be represented by  $\hat{n}_o$ , then

$$n_o = \hat{n}_o \hat{D}^3 \quad (6)$$

The value of  $\hat{n}_o$  is a subject of debate since it is currently impossible to measure submicron scale bubbles which can presumably serve as nucleations sites. Current estimates lie in the range of  $10^8 - 10^{12}$  sites/ $m^3$  for small scale internal flows. Recent parametric analyses<sup>21</sup> indicate that results are not sensitive to this parameter; a value of  $10^{12}$  sites/ $m^3$  was used for all calculations presented herein.

As the number of sites decrease with the volume of liquid,  $L_o$  grows and the pressure difference term in Eq. 4 becomes less dominant. This feature accounts for hydrodynamic non-equilibrium effects in which the inertia of the liquid (second term on RHS of Eq. 4) becomes significant. It is this feature that accounts for scaling effects which are well established in cavitating flows.

## Model Validation

The model has had extensive validation on a variety of cavitating flows. Cavitation extent ( $L_C$  in Fig. 1) matches experimental results for flows over axisymmetric headforms<sup>18,19</sup>. In addition, extensive comparisons

have been made on experiments conducted in a high aspect ratio cavitating slot flow using a 2-D approximation for the flowfield. In this case, cavitation lengths<sup>9,12</sup> compare well with measurements from Dr. Collicott's research group at Purdue.

For the present studies, comparisons were made with cavitation inception pressure measurements of Bergwerk<sup>5</sup>, with discharge coefficient measurements of Nurick<sup>6</sup> and with cavitation frequency measurements of Chandra and Collicott<sup>11</sup>. Figure 3 provides a comparison of the "critical pressure ratio" measured by Bergwerk and the results from the model. Excellent agreement is shown over the range of  $L/D$  values presented.

Comparisons on the discharge coefficient (Fig. 4) showed greater discrepancies. The discharge coefficient is defined as the ratio of the measured (or calculated) flowrate to the ideal flowrate one gets by using the Bernoulli velocity. This parameter measures contraction and friction losses in this particular flowfield. Since the flow is inherently unsteady for most cases studied, we computed a time-averaged value,  $\bar{C}_D$ , which was compared to Nurick's measurements in Fig. 4. The model consistently under predicts consistently under predicts discharge coefficient values by a few percent for the fairly long ( $L/D = 6$ ) orifice studied. While the calculations assume a sharp-edged inlet, the amount of inlet rounding/beveling on the experimental hardware is not known. Note that a small degree of rounding can lead to substantial changes in discharge<sup>20</sup> (also see Fig. 16 and associated discussion).

The dimensional cavitation frequency,  $f_c^*$ , is compared with the measurements of Chandra and Collicott<sup>11</sup> in Fig. 5. The computed results were obtained by comparing 2-D simulations with measurements on a high aspect ratio slot. For the numerical results, cavitation frequency was obtained by performing Fourier transform. Results in Fig. 5 compare the primary harmonic (which contains the bulk of the oscillatory energy) for both experiment and calculation. Good comparisons are noted, thereby validating the utility of the model to assess frequencies developed in these flows.

## Results of Parametric Studies

Given the nondimensionalization describe above, a sharp-edged orifice geometry is completely prescribed from an input  $L/D$  value. From Eq. 1, Reynolds and cavitation numbers also characterize the flow. However, the flow is not uniquely defined by these two parameters since  $K$  depends on the pressure drop, vapor pressure, and inlet pressure. We chose to use the downstream pressure,  $P_2$  as the third parameter characterizing a given flow situation. By raising  $P_2$  and maintaining a constant pressure drop, pressure levels throughout the orifice are increased and the extent of cavitation tends to be reduced.

In this work, we focus on the unsteadiness caused by instability of the vena-contracta under cavitating and non-cavitating conditions. Previous works<sup>18-21</sup> provide in-depth maps of the flowfield; the present study focuses primarily on unsteadiness in global/integral parameters. Nearly 200 simulations were conducted in the studies. A typical simulation required 6-8 hours runtime on a 450 MHz Pentium II PC.

Figure 6 presents the gross structure of the flowfield near the inlet lip at a given instant in time for

both cavitating and non-cavitating flows. The radial coordinate is expanded in these plots for clarity. The pressure increases at the aft end of the vena contracta are fed forward and effect the subsequent shape of this region. This process is documented in detail for cavitating flows in Ref. 21. In the case where cavitation is present, the recirculation zone can detach from the main vena contracta and be convected downstream. The particular image in Fig. 6 depicts an instant in this process. The influences on orifice discharge characteristics are investigated with respect to this unsteadiness from these vena contracta instabilities in the following sections.

## Orifice Flow Under Partial Cavitation Conditions

A “baseline” case is presented to provide the reader with insight into the unsteady massflow characteristics which can be attributed to partial cavitation. Orifice massflow is represented in terms of a discharge coefficient,  $C_D$ , which is defined in the usual manner:

$$C_D = \dot{m}/(\rho_l v A) \quad (7)$$

where  $\dot{m}$  is the massflow obtained by integration of the velocity profile at the exit plane,  $v$  is the Bernoulli velocity as described previously, and  $A$  is the orifice cross-sectional area. The conditions noted in Figs. 7 and 8 would be consistent with the flow of water through a 580 micron orifice with an inlet pressure ( $P_1$ ) of 4.3 atmospheres.

Figure 7 shows the periodic variations in dimensionless cavitation length ( $L_C$ ) for these conditions. In this work, the cavitation length was assumed to correspond to the downstream point in the orifice where the pseudo-density had a value of 0.98. Since the density changes rapidly at the end of the cavitation region, similar results are obtained for other density threshold values. Note the periodic behavior; in this case, the cavity oscillates over a range of about 10-50% of the orifice length.

The repercussions of this oscillatory behavior on orifice massflow characteristics are shown in Fig. 8. In this particular case, the unsteadiness leads to orifice massflow variations of roughly  $\pm 4$  percent. Most current atomization theories suppose that the flow from the orifice is steady and that the fluid exits the orifice initially as an undisturbed cylinder subject to aerodynamic interactions from the gas phase. In the present case, the variations in massflow would lead to high-amplitude perturbations with respect to a linearized theory such as this. Experimentalists generally measure massflow by collecting fluid over some time period and therefore only measure an averaged discharge coefficient. For this reason, the unsteadiness in orifice flow has not been studied in any detail previously.

By performing a Fourier transform on the  $L_C$  and  $C_D$  histories, one can obtain the principle frequency of oscillation of each of these parameters,  $f_C$  and  $f_D$ . Since these frequencies are nondimensionalized by the orifice diameter and the Bernoulli velocity, they represent Strouhal numbers for each of the oscillations. In addition, we should point out that the Fourier transforms typically show most of the energy in 2-3 discrete frequencies<sup>11,21</sup>. The bulk of the energy is contained in the primary harmonic, other frequencies which appear to be higher harmonics tend to contain much less energy. This work will focus on behavior of the

primary harmonic found for each particular orifice flow.

Figure 9 shows the variation in non-dimensional  $f_C$  and  $f_D$  with variations in  $K$  at fixed Reynolds number for an orifice with  $L/D = 8$ . The point of cavitation inception is shown on the figure; the region to the left of this point is where cavitation is evident in the flowfield. Over this range note the agreement in the two frequencies; this factor confirms the notion that cavitation oscillations are responsible for massflow variations when cavitation is present. Note that cavitation does tend to increase frequencies up to a point, beyond which the very large cavities tend to respond at lower frequencies. This behavior is consistent with prior simulations<sup>21</sup> which showed the oscillation generated by a disturbance in the collapse zone which is fed upstream at a roughly constant velocity.

It may be possible to make use of this result to design passive oscillations of a desired frequency. In general, the frequencies are consistent with the time it takes a fluid element to traverse the length of the orifice passage. Atomizers which produce fine sprays tend to produce droplets at much higher frequencies than those noted in Fig. 9. Partial cavitation may be used to “pump” instabilities for atomizers operating at more modest pressure drops such as a flow produced in inkjet printing applications.

## Reynolds Number Effects

A series of simulations were conducted to investigate the influence of Reynolds number as an independent parameter. Orifice geometry, cavitation number, and exit pressure were all held fixed in this series of runs. Results on the mean and oscillatory components of  $L_C$  and  $C_D$  are shown in Fig. 10. The mean discharge coefficient ( $\bar{C}_D$ ) was unaffected by changes in  $Re$ . This behavior is attributed to the fact that a relatively short orifice,  $L/D = 4$ , was used such that contraction losses dominated the losses and wall friction was of lesser importance. As  $Re$  was increased, the average cavitation length,  $\bar{L}_C$ , also changed very little. However at low  $Re$ , the extent of cavitation was reduced; below  $Re$  of about 5000, no cavitation was observed in this case.

The RMS oscillations in cavitation length and discharge coefficient ( $\Delta L_C$ ,  $\Delta C_D$ ) show a similar Insensitivity to  $Re$  above  $Re \approx 20,000$ . Below  $Re \approx 5000$  the oscillations vanish and a steady flow is computed. It is interesting to note that this threshold is near experimental values quoted for transition to turbulent flow in pipes. In this problem, the unsteadiness which has traditionally been attributed to turbulence may in many cases be due to instability of the vena-contracta since our laminar calculations show “turbulent like” qualities.

## Supply Pressure Effects

A series of simulations were conducted with a fixed orifice diameter, discharge pressure, and fluid properties to identify the influence of supply pressure on the flowfield. Figure 11 highlights massflow variations for three different orifice lengths as a function of supply pressure. The point where cavitation begins is noted in each curve; the region to the right of this point corresponds to partially cavitating flows. Note that cavitation

becomes evident at supply pressures in the 2-3 atmosphere range for these sharp-edged inlets; since most applications utilize higher supply pressures cavitation is presumed to be present in a large fraction of pressure atomizers in use today. The highest massflow variations occur in this region as the violence associated with cavity collapse (or partial collapse) and reformation lead to significant changes in massflow. It is interesting to note that significant massflow variations are shown even for *non-cavitating flows*. Once again, these variations are largest for the shortest orifice passages.

Figure 12 shows the oscillations in cavitation length with increased supply pressure. The increases in  $\Delta L_C$  are directly correlated with increases in  $\Delta C_D$  as discussed previously. Note that as the orifice length increases,  $\Delta L_C$  becomes relatively insensitive to this parameter, the cavitation is restricted to a fairly small fraction of the orifice length.

Figure 13 depicts the changes in non-dimensional oscillation frequency with  $P_1$  for each of the three orifices studied. There is a general trend toward decreasing frequencies with increased orifice length; the frequencies are coupled to the orifice transit time. The onset of cavitation signals a dramatic increase in frequency for each case studied. It may be possible to use this fact as a diagnostic tool by instrumenting an orifice with microphones or transducers to detect acoustic energy in the fluid. In combining these results with Fig. 11 one can note that peak oscillation frequencies are not correlated with maximum variations in massflow; instead massflow variations are correlated with  $L_C$ .

## Effect of Discharge Pressure

Figure 14 highlights the effect of discharge pressure ( $P_2$ ) on the range under which cavitation is prominent in a  $L/D = 6$  orifice. Increasing back pressure leads to modest increases in the  $K$  value at which inception occurs. The flipping condition appears to be insensitive to back pressure, occurring near  $K = 1.5$  for the three cases investigated. Of course, the flipping condition is highly dependent on orifice length.

Finally, we note that the cavitation range tends to be extended as the discharge pressure is raised. High pressure applications such as combustion chambers are subject to cavitating flows over a much wider range of pressures than one might see in an ambient pressure test. This points out the scaling problems encountered in cold flow testing of high pressure combustion systems; cavitation and Reynolds numbers cannot both be matched unless both pressure levels and pressure drops are replicated in testing.

The implications of changes in back pressure on oscillation frequencies is shown in Fig. 15. Raising pressure levels in the atomizer leads to increases in oscillation frequencies over the range of conditions in which cavitation is present. This behavior is attributed to the fact that pressure gradients increase at constant  $K$  with the increase in discharge pressure since the orifice dimensions are fixed in this particular study. Higher pressure gradients lead to higher velocities feeding periodic processes associated with the unstable cavitation region. Under non-cavitating conditions, the change in  $P_2$  had no effect on the oscillation frequencies.



## Effect of Inlet Rounding

A series of simulations were conducted with fixed fluid properties, discharge pressure, and  $L/D$  to assess the effects of inlet rounding. Several experiments and numerical simulations<sup>20</sup> have noted that inlet rounding can delay the occurrence of cavitation and increase discharge coefficient through reductions in contraction losses. However, the effects of rounding on the unsteady behavior has not been investigated in any great detail. For this reason, the unsteady characteristics have been studied assuming the inlet is rounded with a circle of given radius. Figure 16 depicts the level of massflow variations due to unsteadiness at various cavitation numbers for three levels of inlet rounding ( $r/R = 0, 0.05, 0.1$ ). The cavitation onset point is noted; cavitating results lie to the left of this point since decreasing  $K$  corresponds to increased supply pressure.

Results in Fig. 16 show that massflow variations are reduced dramatically for even a small amount of inlet rounding. For an inlet radius of 10% of the orifice radius ( $r/R = 0.1$ ) massflow variations have all but been eliminated for the entire pressure range noted. These results are disturbing in that there is a great sensitivity of the flow unsteadiness to minor changes in shape. Since real orifices are not infinitely sharp, cavitation sites will most likely appear at burrs or notches formed during the fabrication process. These features are generally not reproducible and lead to hole-to-hole variations which are known to plague some manufacturers. For example, modern diesel orifices are typically 2-300 microns in diameter and defects/tolerances are generally a significant fraction of this diameter. Reproducibility in tiny orifices can be problematic for these reasons.

Figure 17 highlights cavitation length variations from the inlet rounding study. The overall level of length variations is reduced as inlet rounding is increased. In addition, rounding of the inlet suppresses cavitation (and  $\Delta L_C$ ) moving inception and partial cavitation to lower  $K$  and higher  $P_1$  values. It is interesting to note that substantial  $\Delta L_C$  values are still noted for the rounded inlets (compare values with those in Fig. 12), yet the repercussions on the massflow are much less pronounced. The cavity still oscillates, but the undulations are much less violent than in the case of a sharp-edged inlet.

## Conclusions

The internal flow in plain orifice atomizers operating at modest or high Reynolds numbers is inherently unsteady due to the instability of the vena-contracta formed at the inlet lip. This phenomenon leads to periodic variations in orifice massflow over a time scale near the orifice transit time. Cavitation is shown to enhance both the magnitude and the frequency of these oscillations. The influence of Reynolds number, supply pressure, discharge pressure, orifice  $L/D$  and inlet rounding have been investigated using laminar axisymmetric calculations with a homogeneous flow model for addressing cavitation.

Both the mean and oscillatory components of cavitation length and discharge coefficient are affected little by Reynolds numbers when it is above about 20,000. Steady flow solutions were found for Reynolds numbers below about 5000. Unsteadiness in orifice massflow tended to increase with decreased orifice  $L/D$ . This unsteadiness also increased rapidly near conditions where the orifice was cavitating. Modest amounts of

cavitation increased the frequency of massflow oscillations with a maximum frequency occurring at modest cavitation lengths. Increased discharge pressure tended to delay cavitation inception and broaden the range of injection pressures over which cavitation was present. Rounding of the inlet had dramatic effects in reducing unsteadiness in massflow, even under cavitated conditions. The large sensitivity due to minor geometry changes is unsettling in that minor manufacturing variations can play important roles in the overall behavior of these atomizers.

## Nomenclature

$C_d$  - Orifice Discharge Coefficient (Eq. 7)

$D$  - Orifice diameter

$f$  - Non-dimensional frequency

$f^*$  - dimensional frequency

$K$  - Cavitation number

$L$  - Orifice length

$\dot{m}$  - Orifice massflow

$L_c$  - Cavitation length

$n$  - Bubble number density

$P$  - Pressure

$Re$  - Reynolds number

$r$  - Radial or transverse coordinate

$t$  - Time

$v$  - Bernoulli velocity

$z$  - Axial coordinate

$\alpha$  - Void fraction

$\mu$  - Viscosity

$\rho$  - Fluid pseudo-density

## Subscripts

1 - Inlet

2 - Outlet

$C$  - Cavitation length

$D$  - Discharge coefficient

$l$  - Liquid

$v$  - Vapor

## References

1. Lefebvre A. H., *Atomization and Sprays*, Hemisphere Publishing Company, 1989.
2. Ohn T. R., Senser D. W., and Lefebvre A. H., "Geometrical Effects on Discharge Coefficients for Plain-Orifice Atomizers," *Atomization and Sprays*, Vol. 1, No. 2, 1991, pp. 137-157.
3. Reitz R. D., and Bracco F. V., "Mechanisms of Breakup of Round Liquid Jets," *Encyclopedia of Fluid Mechanics. Vol. 3: Gas-Liquid Flows. Properties of Dispersed and Atomized Flows*, pp. 233-249, 1986.
4. Knapp R. T., Daily J. W. and Hammit F.G., *Cavitation*, McGraw-Hill, 1970.
5. Bergwerk W., "Flow Pattern In Diesel Nozzle Spray Holes," *Procs. Instn. Mech. Engs.*, Vol.173, pp655-660, 1959.
6. Nurick W. H., "Orifice Cavitation and Its Effect on Spray Mixing," *Journal of Fluids Engineering*, Dec., pp. 681-687, 1976.
7. He L. and Ruiz F., "Effect of Cavitation on Flow and Turbulence in Plain Orifices for High-Speed Atomization," *Atomization and Sprays*, Vol. 5, pp. 569-584, 1996.
8. Chaves H., Knapp M. and Kubitzek A., "Experimental Study of Cavitation in the Nozzle Hole of Diesel Injectors Using Transparent Nozzles," SAE Paper No. 950290, 1995.
9. Henry M. E. *An Experimental Investigation of a Cavitation Slot Orifice*, MS. Thesis, School of Aeronautics and Astronautics, Purdue University, IN, May 1997.
10. Li H. and Collicott S. H., "Initial Images of Cavitation Inside High-Pressure Atomizers," ILASS-99 Conference Proceedings, pp. 409-413, Indianapolis, IN, 1999.
11. Chandra B. W. and Collicott S. H., "Experimental Investigation of Cavitation Frequency in a Slot Orifice," ILASS-99 Conference Proceedings, pp. 379-384, Indianapolis, IN, 1999.
12. Sanchez P. K. and Collicott S. H., "Statistics of Cavitation Length in a 2-D Slot Orifice," ILASS-99 Conference Proceedings, pp 403-408, Indianapolis, IN, 1999.
13. Hiroyasu H., Arai M. and Shimizu M., "Break-Up Length of a Liquid Jet and Internal Flow in a Nozzle," ICLASS-91, Paper 26, pp. 275-282, 1991.
14. Tamaki N., Nishida K., Hiroyasu, H. and Shimizu, M., "Effects of the Internal Flow in a Nozzle Hole on the Breakup Processes of a Liquid Jet," to appear, *Atomization and Sprays*, see also, ILASS-96 Conference Proceedings, 1996.
15. Karasawa T, Tanaka M., Abe K. and Kurabayashi T., "Effect of Nozzle Configuration on the Atomization of a Steady Spray," *Atomization and Sprays*, Vol.2, pp.411-426, 1992.
16. Schmidt D. P., Rutland C. J. and Corradini M. L., "A Fully Compressible, Two-Dimensional Model of Small, High-Speed, Cavitating Nozzles," *Atomization and Sprays*, Vol. 9, No. 3, pp. 255-276, 1999.
17. Delannoy Y. and J. L. Kueny, "Two Phase Flow Approach in Unsteady Cavitation Modeling," *Cavitation and Multiphase Flow Forum*, ASME, FED Vol.98, 1990.
18. Chen Y., *Numerical Approaches for Hydrodynamic Cavitating Flows*, Ph.D Thesis, School of Aeronautics and Astronautics, Purdue University, IN, May 1995.
19. Chen Y. and Heister S. D., "Modeling Hydrodynamic Non-Equilibrium in Bubbly and Cavitating Flows," *Journal of Fluids Engineering*, Vol. 118, No. 1, pp. 172-178, 1995.

20. Chen Y. and Heister S. D., "Modeling Cavitating Flows in Diesel Injectors," *Atomization and Sprays*, Vol. 6, pp. 709-726, 1996.
21. Bunnell R. A., Heister S. D., Yen C. and Collicott S. C., "Cavitating Injector Flows: Validation of Numerical Models and Simulations of High-Pressure Injectors," To Appear, *Atomization and Sprays*, 1999.
22. Alajbegovic A., Grogger H. A. and Philipp H., "Calculation of Transient Cavitation in Nozzle Using the Two-Fluid Model," ILASS-99 Conference Proceedings, pp. 373-377, Indianapolis, IN, 1999.

## Figure Captions

1. Schematic of the flow features in a cavitating orifice.
2. Computational domain and mesh for orifice flow (for clarity, only a small portion of the grid lines are shown).
3. Critical pressure ratio comparison with experimental results<sup>5</sup>;  $D=2.5\text{mm}$ ,  $Re \approx 10000$ , sharp-edged inlet.
4. Discharge coefficient  $C_D$  comparison with experimental results<sup>6</sup>;  $L/D=6$ ,  $D=3.18\text{ mm}$ ,  $P_2=13.8\text{ psi}$ .
5. Cavitation frequency comparison with experimental results<sup>11</sup> for high aspect ratio slots
6. Typical streamline patterns near the inlet lip under cavitating ( $Re = 16188$ ,  $K = 1.53$ ) and noncavitating ( $Re = 11849$ ,  $K = 1.98$ ) conditions. The vertical scale has been expanded for clarity.
7. Typical quasi-periodic behavior of cavitation length  $L_C$
8. Typical orifice discharge coefficient ( $C_D$ ) behavior.
9. Frequency of discharge ( $f_D$ ) and and cavitation length ( $f_C$ ) vs. cavitation number;  $L/D=8$ ,  $P_2 = 1\text{ atm}$ .
10. The effect of Reynolds number on average and unsteady components of discharge coefficient and cavitation length;  $L/D=4$ ,  $K = 1.6$ ,  $P_2=1\text{ atm}$ .
11. The effect of supply pressure on the fluctuation of discharge coefficient,  $D=0.566\text{ mm}$ ,  $P_2=1\text{ atm}$ , sharp-edged inlet.
12. The effect of supply pressure on fluctuations in cavitation length,  $D=0.566\text{mm}$ ,  $P_2=1\text{ atm}$ , sharp-edged inlet.
13. The effect of supply pressure on the frequency of discharge coefficient,  $D=0.566\text{ mm}$ ,  $P_2=1\text{ atm}$ , sharp-edged inlet.
14. The effect of back pressure on the flow state  $L/D=6$ ,  $D=0.566\text{ mm}$ .
15. The effect of supply pressure on the frequency of discharge coefficient,  $D=0.566\text{ mm}$ ,  $P_2=1\text{ atm}$ , sharp-edged inlet.
16. The effect of inlet rounding on fluctuations of orifice massflow,  $L/D=6$ ,  $P_2=1\text{ atm}$ .
17. The effect of inlet rounding on fluctuations in cavitation length,  $L/D=6$ ,  $P_2=1\text{ atm}$ .

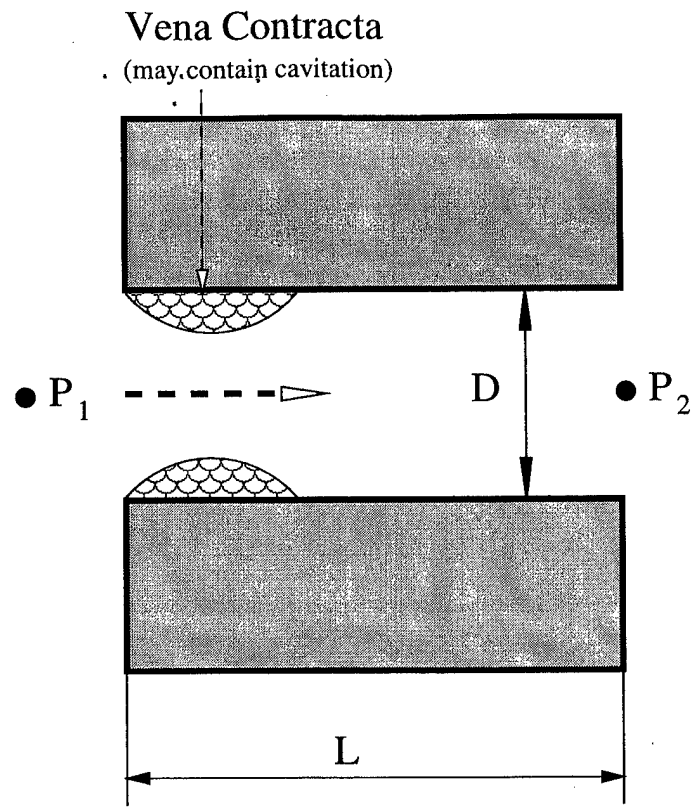


Figure 1: Schematic of the flow features in a cavitating orifice.

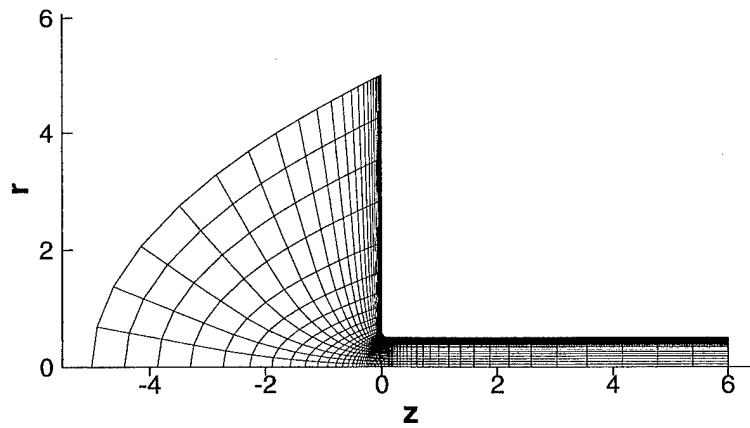


Figure 2: Computational domain and mesh for orifice flow (for clarity, only a small portion of the grid lines are shown).

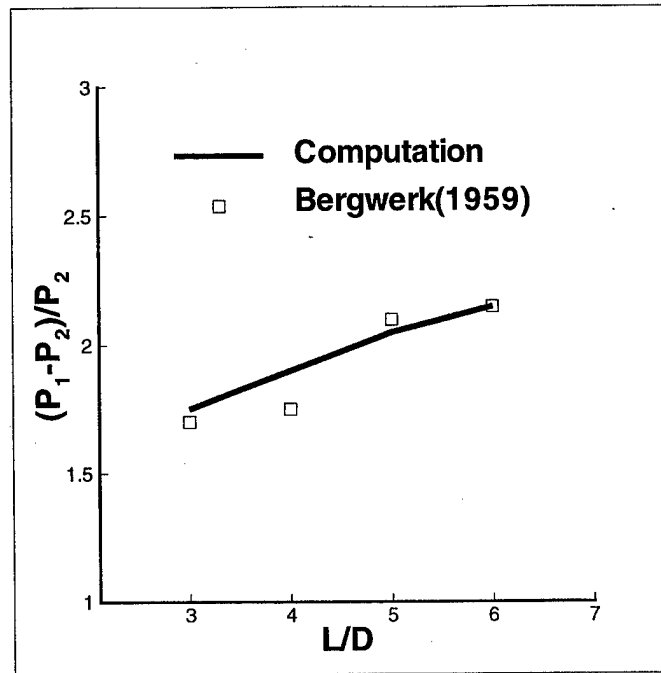


Figure 3: Critical pressure ratio comparison with experimental results<sup>5</sup>;  $D=2.5\text{mm}$ ,  $Re \approx 10000$ , sharp-edged inlet.

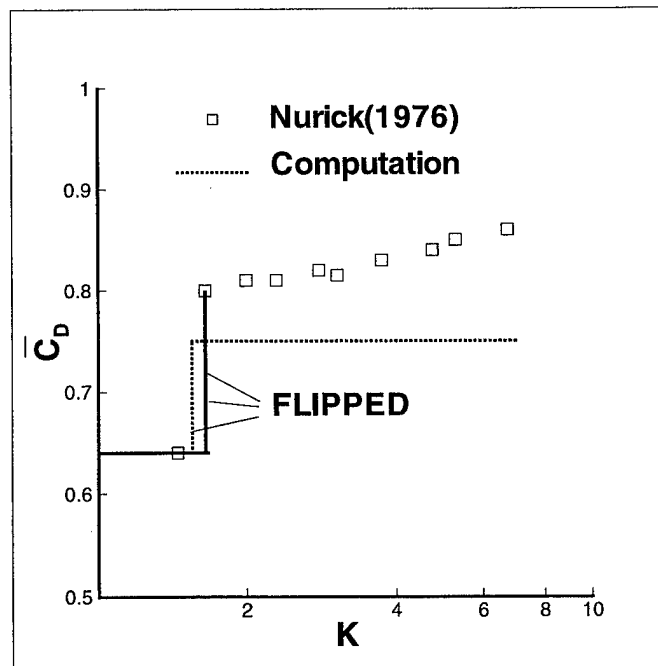


Figure 4: Discharge coefficient  $C_D$  comparison with experimental results<sup>6</sup>;  $L/D=6$ ,  $D=3.18\text{ mm}$ ,  $P_2=13.8\text{ psi}$ .

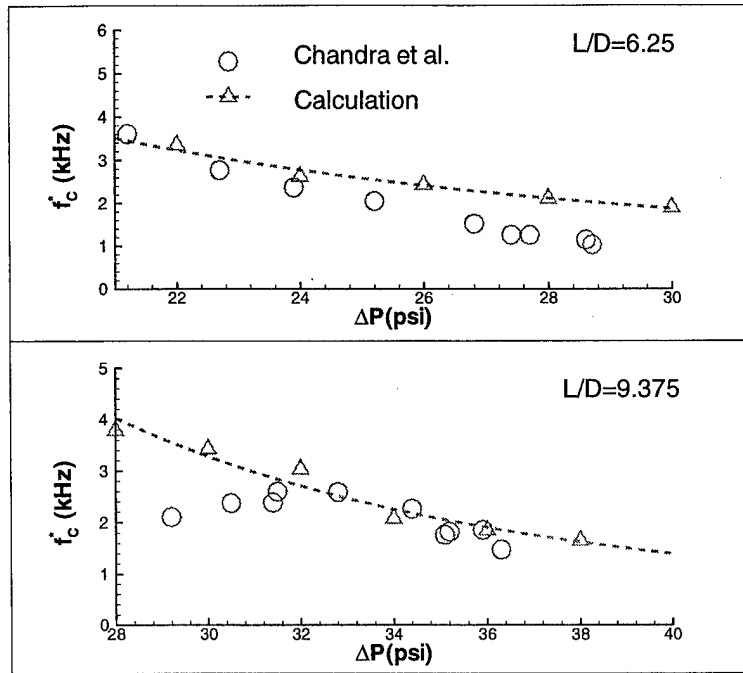


Figure 5: Cavitation frequency comparison with experimental results<sup>11</sup> for high aspect ratio slots

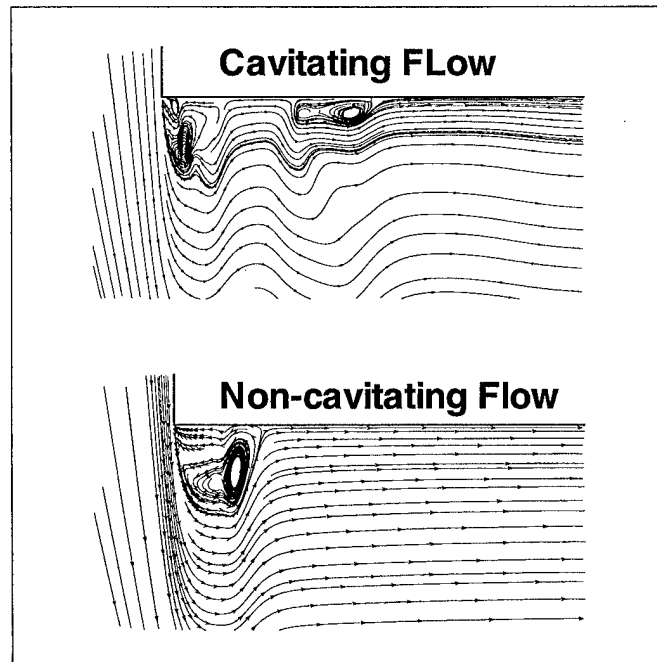


Figure 6: Typical streamline patterns near the inlet lip under cavitating ( $Re = 16188, K = 1.53$ ) and noncavitating ( $Re = 11849, K = 1.98$ ) conditions. The vertical scale has been expanded for clarity.



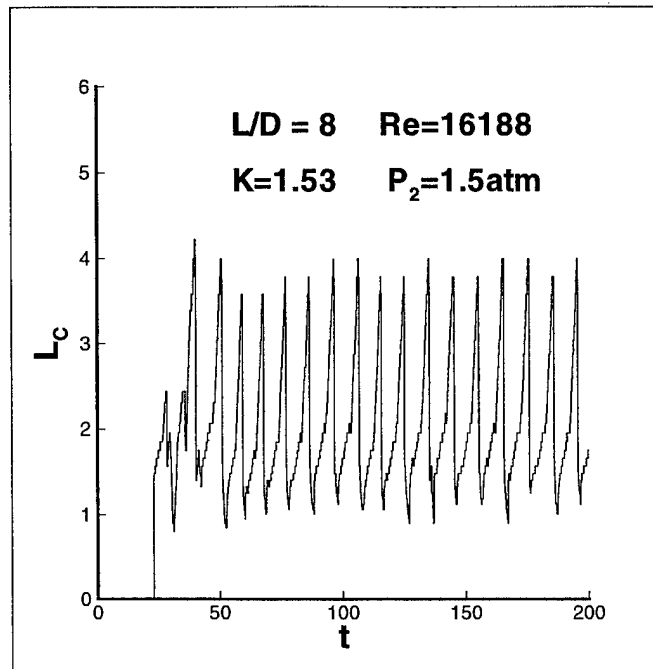


Figure 7: Typical quasi-periodic behavior of cavitation length  $L_C$

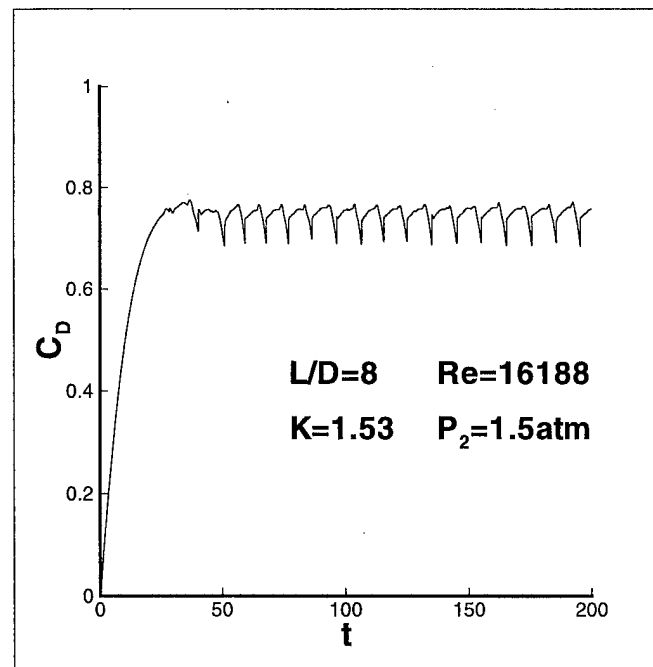


Figure 8: Typical orifice discharge coefficient ( $C_D$ ) behavior.

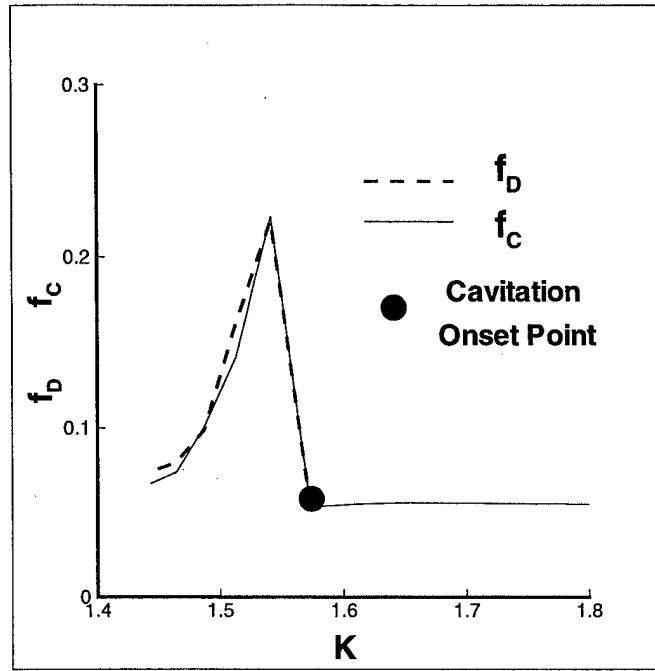


Figure 9: Frequency of discharge ( $f_D$ ) and and cavitation length ( $f_c$ ) vs. cavitation number;  $L/D=8$ ,  $P_2 = 1 \text{ atm}$ .

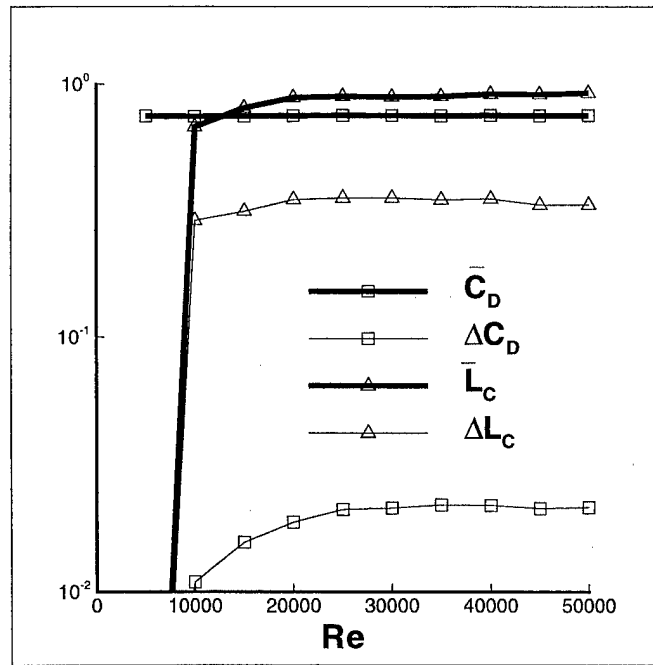


Figure 10: The effect of Reynolds number on average and unsteady components of discharge coefficient and cavitation length;  $L/D=4$ ,  $K = 1.6$ ,  $P_2=1 \text{ atm}$ .

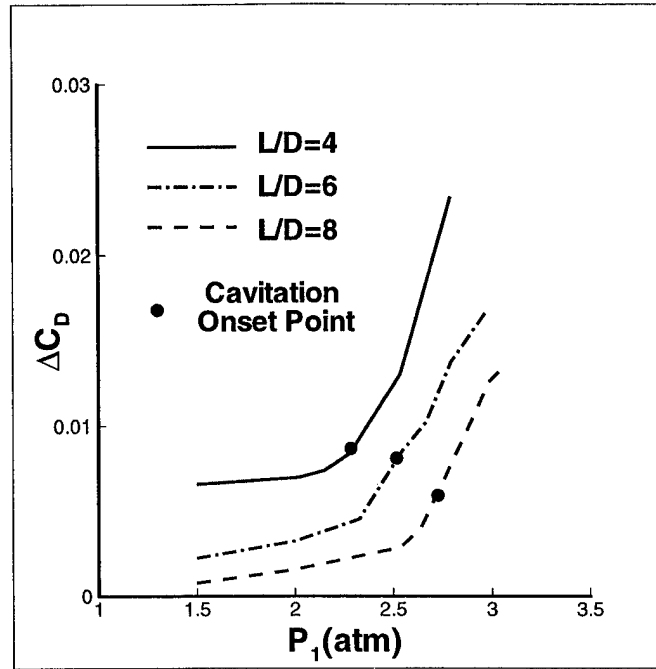


Figure 11: The effect of supply pressure on the fluctuation of discharge coefficient,  $D=0.566$  mm,  $P_2=1$  atm, sharp-edged inlet.

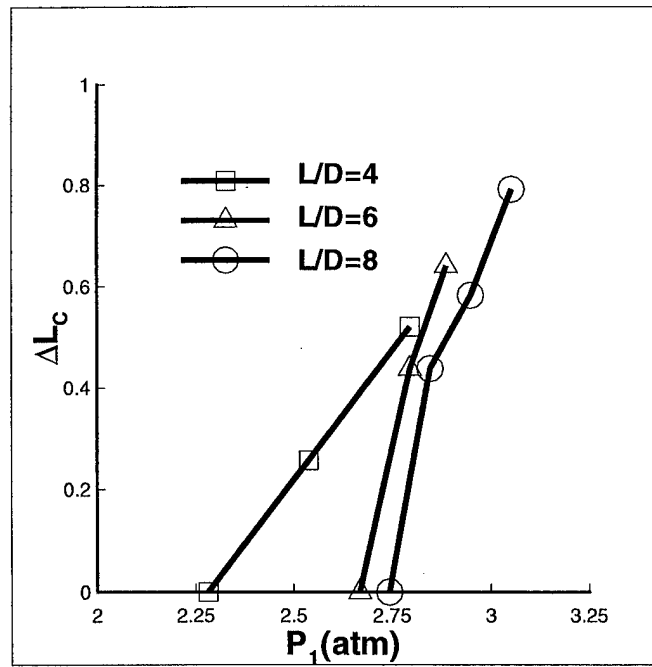


Figure 12: The effect of supply pressure on fluctuations in cavitation length,  $D=0.566$  mm,  $P_2=1$  atm, sharp-edged inlet.

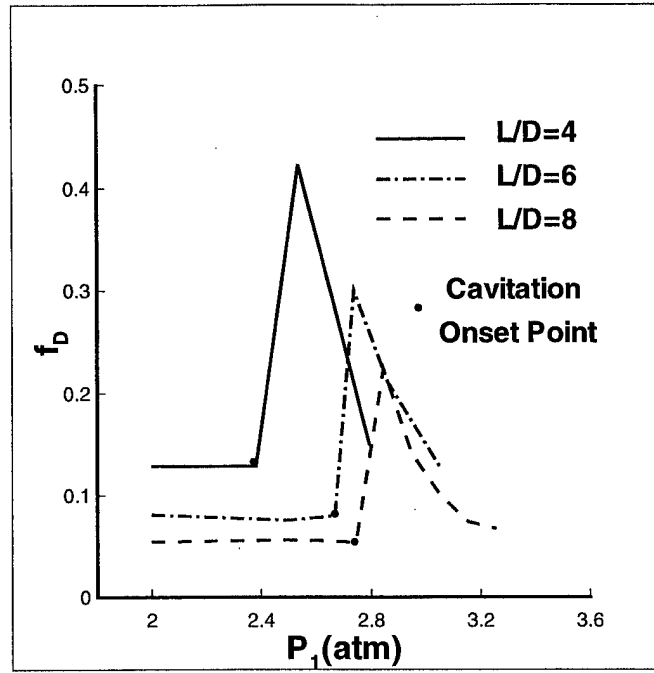


Figure 13: The effect of supply pressure on the frequency of discharge coefficient,  $D=0.566$  mm,  $P_2=1$  atm, sharp-edged inlet.

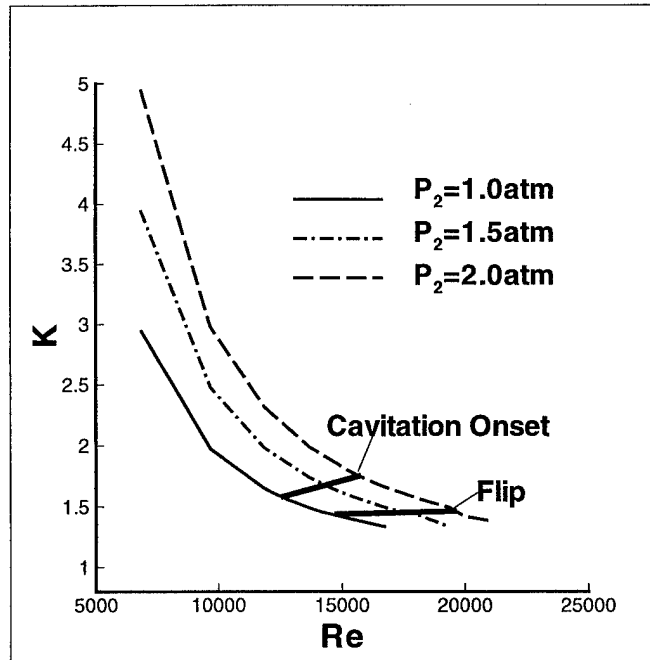


Figure 14: The effect of back pressure on the flow state  $L/D=6$ ,  $D=0.566$  mm.

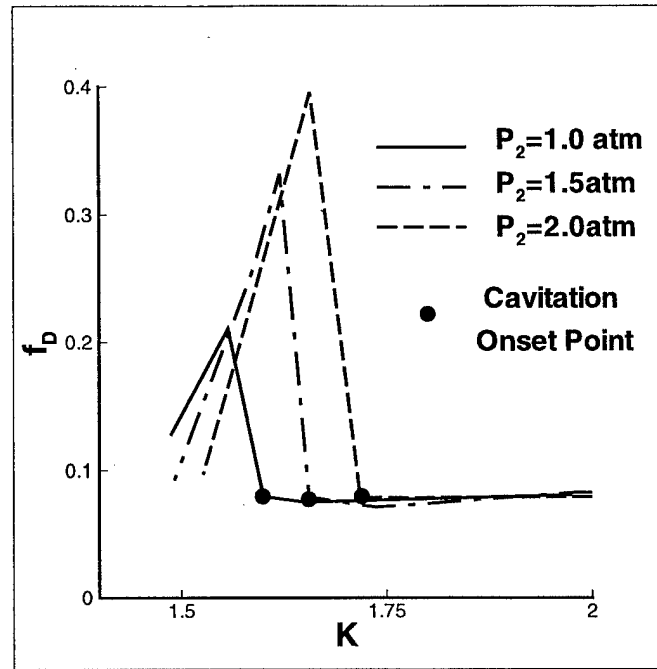


Figure 15: The effect of back pressure on the frequency of discharge coefficient  $L/D=6$ ,  $D=0.566\text{mm}$

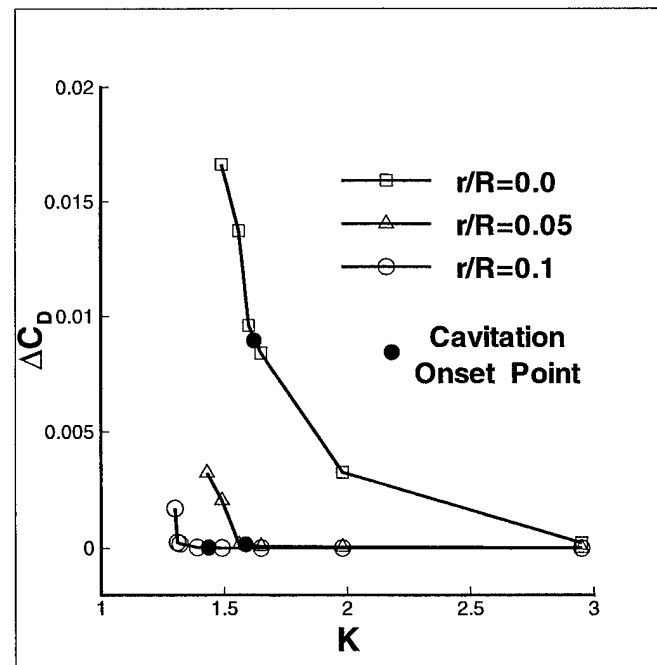


Figure 16: The effect of inlet rounding on fluctuations of orifice massflow,  $L/D=6$ ,  $P_2=1\text{ atm}$ .

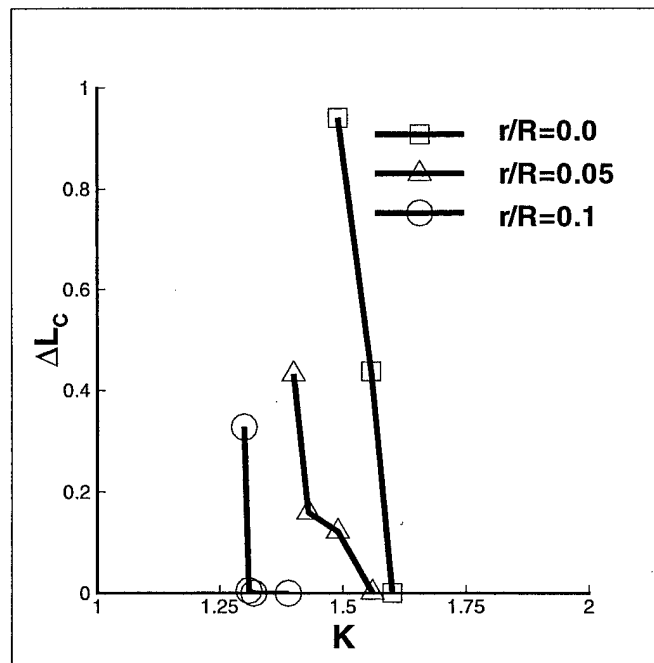


Figure 17: The effect of inlet rounding on fluctuations in cavitation length,  $L/D=6$ ,  $P_2=1$  atm.

## **8 Appendix B - 2D and Axisymmetric Turbulent, Cavitating Flow Simulations**

Xu, C., "Simulation of Orifice Internal Flows Including Cavitation and Turbulence" Ph. D. Thesis, School of Aeronautics and Astronautics, Purdue University, West Lafayette, IN, August 2001, pp. 44 - 81. 1996.

## 4. 2D AND AXISYMMETRIC TURBULENT, CAVITATING FLOW SIMULATIONS

### 4.1 Introduction

The presence of cavitation inside a slot/orifice injector nozzle increases the turbulence level of the flow greatly. Recent experiments (Tamaki et al., 1998; Hiroyasu, 2000) have shown that the turbulence in the nozzle hole resulting from cavitation is a mechanism that promotes atomization. Under partial cavitation conditions, the cavitation region extends only a fraction of the orifice length, its shape is unsteady, and oscillates in a quasi-periodic manner (Bunnell and Heister, 1999; Henry, 1997; Sanchez, 1999). At the rear end of the cavity, the main flow of the liquid eventually reattaches to the wall, and clusters of bubbles collapse accompanying the recovery of pressure. This process generates a great amount of turbulence in the flow. Fig. 4.1 is a schematic representation of this process. While the mechanism of energy transfer from mean flow to turbulence during cavitation remains unresolved, experiments have shown that turbulence intensity is increased in the presence of cavitation. Gopalan and Katz (2000) observed that the unsteady cavity collapse involves substantial increases in turbulence intensity, momentum and displacement thicknesses in the boundary layer. They also showed that the collapse of bubbles is the dominant source of vorticity downstream of a cavity. Ruiz and He (1999) have shown that there is a jump in turbulence intensity in a flow after a cavitation zone, and the turbulence decays more slowly than ordinary turbulence.

In this chapter, the turbulent characteristics of cavitating flows are investigated. The  $k-\omega$  turbulence model and Chen and Heister's (1995) homogeneous fluid model are employed in simulations of turbulent cavitating flows. The predicted discharge



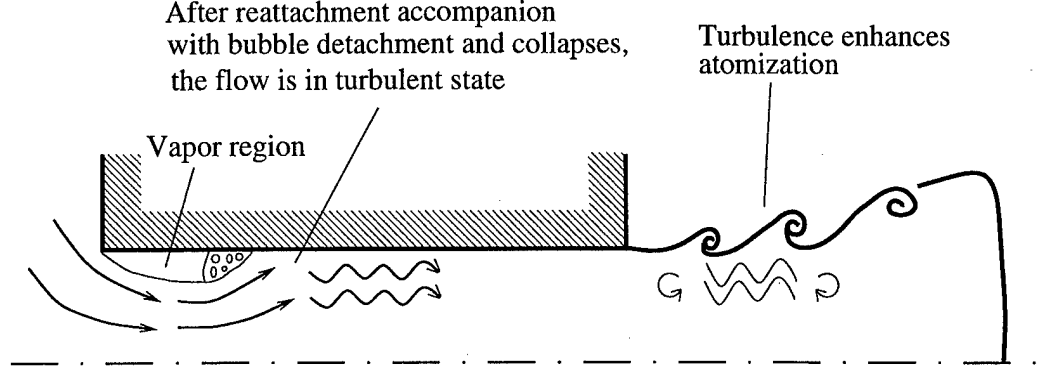


Figure 4.1 Partial cavitation condition enhances atomization

coefficient, cavitation length and turbulence quantities are compared with available experimental data.

## 4.2 Model Formulation

In order to avoid the presence of additional correlations due to the presence of density fluctuation, it is convenient to recast the instantaneous flow fields in terms of Favre averages instead of time averages. A Favre averaged variable, denoted by a tilde, is defined as

$$\tilde{f} = \frac{\overline{\rho f}}{\bar{\rho}} \quad (4.1)$$

Here, we introduce Favre averaging because the density changes greatly between the inside and outside of the cavity region. Favre averaging is a mathematical simplification to eliminate the additional terms resulting from time-averaging because of the fluctuation of density (Wilcox, 1998). Thus, we decompose the flow properties as follows

$$\begin{aligned} u_i &= \tilde{u}_i + u_i'' \\ p &= P + p' \\ \rho &= \bar{\rho} + \rho' \end{aligned} \quad (4.2)$$

where  $\tilde{u}_i$  is Favre mass-averaged velocity, and  $u_i''$  is the fluctuation part of the velocity. Density and pressure are decomposed as the time-averaged part and fluctuation part.

The governing equations are as shown below.

$$\frac{\partial(r^a \bar{\rho})}{\partial t} + \frac{\partial(r^a \bar{\rho} \tilde{u}_i)}{\partial x_i} = 0 \quad (4.3)$$

$$\frac{\partial(r^a \bar{\rho} \tilde{u}_i)}{\partial t} + \frac{\partial(r^a \bar{\rho} \tilde{u}_j \tilde{u}_i)}{\partial x_j} = -r^a \frac{\partial P}{\partial x_i} + r^a \frac{\partial}{\partial x_j} [\bar{t}_{ji} + \tau_{ji}] \quad (4.4)$$

where,  $a = 0$  for a 2-D problem and  $a = 1$  for an axisymmetric problem.  $\bar{t}_{ij}$  and  $\tau_{ij}$  are the viscous stress tensor and mass-averaged Reynolds stress tensor  $\tau_{ij} = -\overline{\rho u_i'' u_j''}$ , respectively, which are defined as

$$\bar{t}_{ij} = \frac{2\mu}{Re} \left( S_{ij} - \frac{1}{3} \frac{\partial u_k}{\partial x_k} \delta_{ij} \right) \quad (4.5)$$

$$\tau_{ij} = \frac{2\mu_T}{Re} \left( S_{ij} - \frac{1}{3} \frac{\partial u_k}{\partial x_k} \delta_{ij} \right) - \frac{2}{3} \bar{\rho} k \delta_{ij} \quad (4.6)$$

Here, the viscous and Reynolds stresses are expressed in compressible form since the divergence of velocity is not zero in the cavity region. The eddy viscosity,  $\mu_T$ , is calculated from the  $k - \omega$  model, and  $S_{ij}$  is strain rate tensor,

$$S_{ij} = \frac{1}{2} \left( \frac{\partial \tilde{u}_i}{\partial \tilde{x}_j} + \frac{\partial \tilde{u}_j}{\partial \tilde{x}_i} \right) \quad (4.7)$$

The  $k - \omega$  model (Wilcox, 1998) takes the following form

$$\begin{aligned} \frac{\partial(r^a \bar{\rho} k)}{\partial t} + \frac{\partial(r^a \bar{\rho} \tilde{u}_j k)}{\partial x_j} &= r^a \tau_{ij} \frac{\partial \tilde{u}_i}{\partial x_j} - r^a Re \beta^* \bar{\rho} k \omega + \\ &\quad \frac{\partial}{\partial x_j} \left[ \frac{r^a}{Re} (\mu + \sigma^* \mu_T) \frac{\partial k}{\partial x_j} \right] \end{aligned} \quad (4.8)$$

$$\begin{aligned} \frac{\partial(r^a \bar{\rho} \omega)}{\partial t} + \frac{\partial(r^a \bar{\rho} \tilde{u}_j \omega)}{\partial x_j} &= r^a \alpha \frac{\omega}{k} \tau_{ij} \frac{\partial \tilde{u}_i}{\partial x_j} - r^a Re \beta \bar{\rho} \omega^2 + \\ &\quad \frac{\partial}{\partial x_j} \left[ \frac{r^a}{Re} (\mu + \sigma \mu_T) \frac{\partial \omega}{\partial x_j} \right] \end{aligned} \quad (4.9)$$

One critical issue is how to resolve the eddy viscosity in the two phase mixture region. Here, we took the same treatment for the eddy viscosity,  $\mu_T$ , as that for the dynamic viscosity,  $\mu$ , for two phase mixture,

$$\mu_T \propto (1 - f_g) \frac{k}{\omega} = \bar{\rho} \frac{k}{\omega} \quad (4.10)$$

where  $f_g$  is void fraction,  $\bar{\rho} = 1 - f_g$ . The implication of Eq. 4.10 is that the contribution of gas phase to turbulence is neglected compared to that of liquid phase because  $\rho_g \ll \rho_l$ . Including the closure coefficient, eddy viscosity is evaluated by

$$\mu_T = \alpha^* \bar{\rho} \frac{k}{\omega} \quad (4.11)$$

The closure coefficients and auxiliary relations of the  $k - \omega$  model are given in section 3.2. All quantities in the above equations are non-nondimensionalized based on Bernoulli velocity  $U^*$ , slot height/orifice diameter  $D^*$ , liquid density  $\rho_l^*$  and dynamic viscosity  $\mu_l^*$ . Hence

$$\begin{aligned} \tilde{u}_i^* &= U^* \tilde{u}_i & P^* &= \rho_l^* U^{*2} P & x_i^* &= D^* x_i \\ k^* &= U^{*2} k & \omega^* &= \frac{\rho_l^* U^{*2}}{\mu_l^*} \omega & Re &= \frac{\rho_l^* U^* D^*}{\mu_l^*} \end{aligned} \quad (4.12)$$

### 4.3 Injector Internal Flows

#### 4.3.1 Boundary Conditions

For flow through an injector slot/orifice, a constant pressure condition is utilized both at the inflow and outflow boundaries. To insure the accuracy of the constant pressure inflow condition, the inflow boundary is placed five gap heights or orifice diameters upstream of the inlet corner. Previous simulations (Bunnell et al., 1999) used zero velocity at the inflow boundary. Because the inflow boundary is far from the inlet, and the velocity there approaches zero, this only leads to minor errors in the calculation. However, this treatment violates conservation of mass flow, since zero velocity at the inflow means zero mass flow rate at the inflow. In order to circumvent this dilemma, we employ a sink at the origin to approximate the inflow velocity conditions. A similar treatment was utilized before to approximate the inflow conditions of a three dimensional manifold cross-flow by Bunnell (1999). As shown in Fig. 4.2 an artificial sink is put at the origin. For a 2-D problem the velocity at the inflow boundary is calculated by

$$u_{in} = -\frac{\Lambda}{2\pi r} \cos \theta \quad v_{in} = -\frac{\Lambda}{2\pi r} \sin \theta \quad (4.13)$$

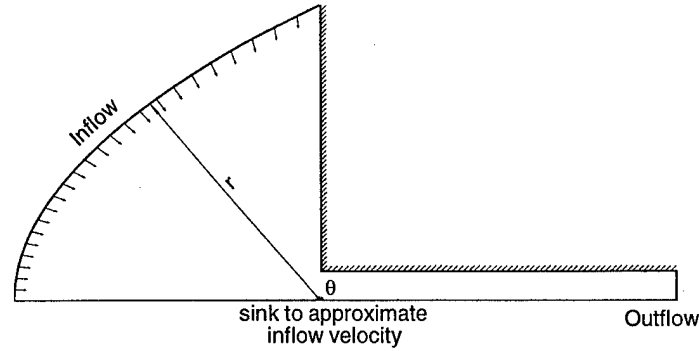


Figure 4.2 Schematic representation of a sink approximation of inflow velocity

The strength of the sink,  $\Lambda$ , is updated during each time step by the conservation of mass flow rate through the nozzle passage. The only difference between an axisymmetric problem and a 2-D problem at this point is that a three dimensional sink is utilized for the former. This assumption might be not fully proper for unsteady flow conditions. However, the unsteadiness is considerably smaller than the average magnitude of mass flow rate through the nozzle hole. This treatment also results in the improvement of discharge coefficient predictions which will be discussed in section 4.3.3.

The inflow boundary condition of turbulence properties  $k$  and  $\omega$  have an unexpected effect on the turbulence models' performance. The profile for  $k$  can be estimated from experimental data. However, it is hard to set the inflow condition for  $\omega$ . Even if  $k$  and  $\mu_T$  are sufficiently small at the inflow boundary, the choice of  $\omega$  can have a significant effect on the flow downstream. It has been documented that free shear flow spreading rates are sensitive to the free stream value of  $\omega$  (Wilcox, 1998). In the flow over a backward facing step, the prediction gives a shorter reattachment length with a larger initial length scale (larger eddy viscosity) (Nallasamy, 1987). For this particular problem, the inflow boundary is put five gap heights or orifice diameters upstream of the inlet corner where the velocity is small. Because no experimental data are available and there is no reason to set a high  $k$  value there, we choose a  $k$  value of  $0.5\%U_{in}^2$  at the inflow boundary, which is very small due to the small inlet

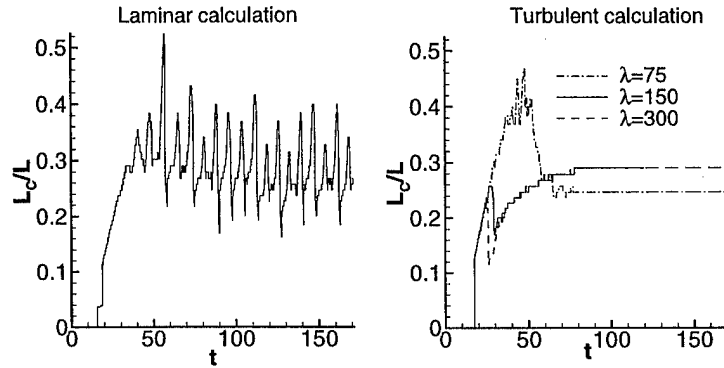


Figure 4.3 Sensitivity of cavitation length to inflow  $\omega$  conditions

velocity. The specific dissipation rate at the inflow boundary is given by

$$\omega = \frac{\sqrt{k}}{\lambda D} \quad (4.14)$$

$\lambda$  is a scale factor and can be a free parameter to adjust the inflow length scale. We performed a study of the effect of inflow  $\omega$  value on the flow downstream. In Fig. 4.3, the curve on the left is from a laminar calculation which represents zero length scale at the inflow, the curves on the right are due to turbulent calculations with three different length scales. The laminar solution gives a cavitation length with significant oscillations representing strong unsteadiness in the flow field. However, turbulent modeling produces a constant value of cavitation length. This is not outside our expectation since Reynolds averaged models decompose the instantaneous flow field into an average part and a fluctuating part and only solves for the mean flow part. This simplification usually results in a steady state solution which still provides the essence of a problem. In this study, we choose three different  $\lambda$  values 75, 150 and 300. Larger  $\lambda$  values correspond to smaller  $\omega$  values (larger eddy viscosity). As shown in Fig. 4.3, there is no difference in the resulting  $L_C$  when  $\lambda = 150, 300$ . Note that the cavitation length in these two cases is close to the average value of  $L_C$  from the laminar result. We prefer a smaller  $\lambda$  value which gives a smaller eddy viscosity at the inflow because we believe the turbulence level is not high there. A  $\lambda$  value of 150

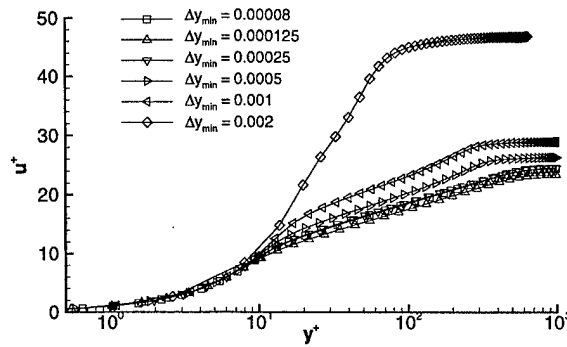


Figure 4.4 Velocity profile resolved by different meshes (a)

gives an inflow eddy viscosity approaching unity, and this value is used through all the calculations.

#### 4.3.2 Grid Refinement Study

In previous work (Bunnell et al., 1999), a grid-refinement study was performed. A grid of 140x60 was found to be fine enough for laminar simulations. However this grid is not proper for turbulence modeling calculations. It is necessary to place a very fine grid in the near wall region to resolve a turbulent boundary layer. Since the grid used is highly stretched in the wall normal direction, we carried out this grid dependency study in two ways: (1) the effect of minimum distance of the grid beyond the wall, (2) the effect of the total number of grid points in the normal direction. Fig. 4.4 shows the effect of the minimum distance away from the wall of a mesh on the velocity profile at the exit of a circular orifice. Here  $u^+$  and  $y^+$  are defined as

$$u^+ = \frac{\tilde{u}}{u_\tau} \quad \text{and} \quad y^+ = \frac{u_\tau y}{\nu} \quad (4.15)$$

where  $u_\tau$  is the friction velocity.

A typical velocity profile for a turbulent boundary layer consists of three regions: viscous layer, log layer and defect layer. It is clearly shown in Fig. 4.4 that a mesh with the first point placed at 0.002 can not resolve the three-layer structure. As the first grid moves closer to the wall the friction velocity  $u_\tau$  resolved is greater, generating a lower curve in the plot. However a mesh with  $\Delta y_{min} = 0.000125$  produces a lower

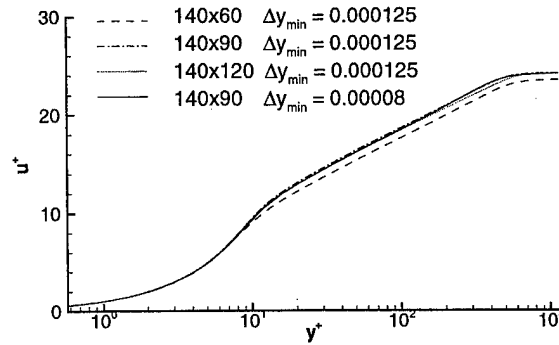


Figure 4.5 Velocity profile resolved by different meshes (b)

curve than the one produced by a mesh with  $\Delta y_{min} = 0.000080$ . This is because a constant total number of normal grid points of 60 was used in the calculations of Fig. 4.4. The smaller  $\Delta y_{min}$  is, the coarser the grid in the middle of the flow field. To a certain degree, such a grid, however, is less sufficient. Fig. 4.5 shows the effect of the total number of grid points in the normal direction. With  $\Delta y_{min} = 0.000125$  a mesh of 140x90 is equally sufficient compared to a mesh of 140x120 and a mesh of 140x90 with  $\Delta y_{min} = 0.000080$ . Thus we consider a grid of 140x90 with  $\Delta y_{min} = 0.000125$  to be fine enough for the turbulence calculation. With such a choice, the wall unit of the first point below or above the wall is at  $y^+ = 0.16$  and about 10 points are placed below  $y^+ = 2.5$ , as recommended by Wilcox (1998).

#### 4.3.3 Discharge Coefficient Prediction

A few axisymmetric runs were made to compare with the discharge coefficient,  $C_D$ , measurements by Nurick (1976) on a circular orifice. Fig. 4.6 shows the results of a comparison on an orifice of  $L/D = 6$ ,  $D = 3.18mm$  under a back pressure of  $P_2 = 13.8psi$ . In Fig. 4.6, “Lam1” represents a laminar calculation with zero inflow velocity boundary condition, “Lam2” represents a laminar calculation with an approximated inflow velocity from an artificial sink as described in the previous section, and the line denoted as “Turb” is calculated from the turbulence model. As shown in the plot, the new inflow velocity treatment greatly improves the prediction

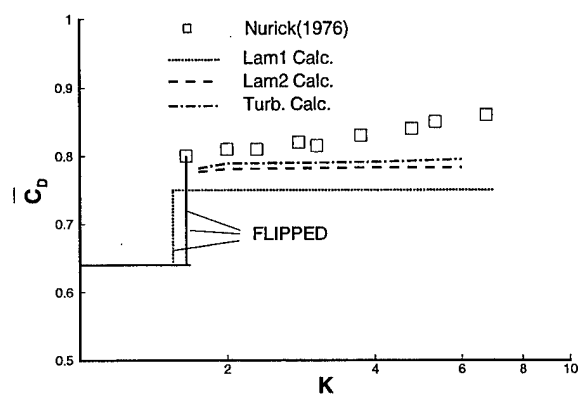


Figure 4.6 Discharge coefficient  $C_D$  comparison with experimental results;  
 $L/D = 6, D = 3.18mm$

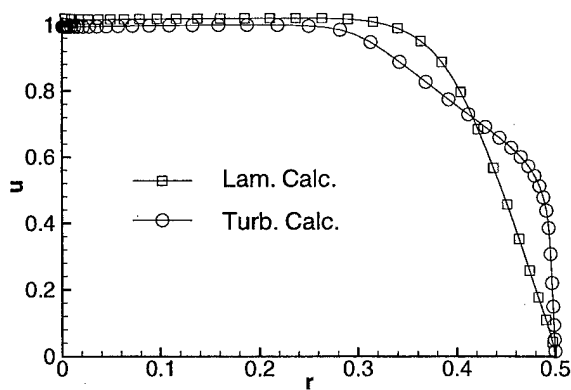


Figure 4.7 Comparison of velocity profile at exit for laminar and turbulent  
solutions;  $L/D = 6, D = 3.18mm$



of discharge coefficient. There is an increase in the magnitude of  $C_D$  of 4.7% over the zero inflow velocity treatment. The turbulence model shows a further improvement and gives results somewhat closer to the experimental data. The differences between the turbulence model and laminar predictions on  $C_D$  might be explained by Fig. 4.7 in which the exit velocity profiles are plotted for both calculations. The turbulent velocity profile is fuller than the laminar one. Due to this feature, the turbulence model yields a larger  $C_D$  by 1.6%. In the calculations a sharp-edged inlet is assumed, however the amount of inlet rounding on the experimental hardware is not known. As noted in section 2.4.5 small degree of inlet rounding can lead to substantial increase in discharge coefficient. This factor might be the primary reason for the model's consistent underprediction of discharge coefficient.

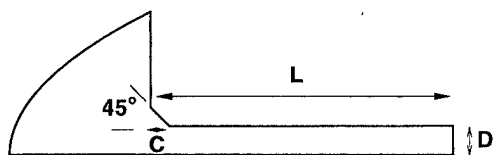
#### 4.3.4 Cavitation Extent Comparison

The 2-D code was used to simulate the flow through slots with the geometry used by Henry (1997) and Sanchez (1999). Extensive comparisons between cavitation length predicted by the laminar code (Bunnell et al. 1999) and the measurements provided by Henry have been conducted. The measured cavitation length falls within the range of the maximum and minimum cavitation lengths predicted by the laminar code for various slot size and flow conditions. To validate the turbulent code, a similar comparison between the average cavitation length predicted by the turbulent code and the measurements by Henry and Sanchez was performed. The computational conditions are presented in Table 4.1.

As mentioned in the previous section, the turbulent code produces a constant value of the cavitation length. Figures 4.8- 4.10 show the results for the three slots. The best agreement was obtained with the slot with medium length/height ratio,  $L/D=9.375$ . For this case the predicted average cavitation length,  $L_C$ , agrees very well with Henry's data. For all three kinds of slots, Henry had a larger cavitation region than Sanchez had, and the slot with the largest length/height ratio,  $L/D = 10.714$  shows the largest difference. The reason for the variation between Henry and Sanchez

Table 4.1 Computational conditions

case	$\Delta P(\text{psi})$	Re	K	$P_V$
L/D=10.174    D(mm)=0.889    C(mm)=0.325				
1	30	22420	1.48	-0.239
2	32	22420	1.45	-0.224
3	34	23110	1.42	-0.211
4	36	23780	1.40	-0.199
5	38	24431	1.38	-0.189
L/D=9.375    D(mm)=1.016    C(mm)=0.325				
6	28	23968	1.51	-0.256
7	30	24809	1.48	-0.239
8	32	25623	1.45	-0.224
9	34	26411	1.42	-0.211
10	36	27177	1.40	-0.199
11	38	27922	1.38	-0.189
L/D=6.25    D(mm)=1.524    C(mm)=0.325				
12	22	31868	1.65	-0.326
13	24	33285	1.60	-0.299
14	26	34644	1.55	-0.276
15	28	35952	1.51	-0.256
16	30	37214	1.48	-0.239



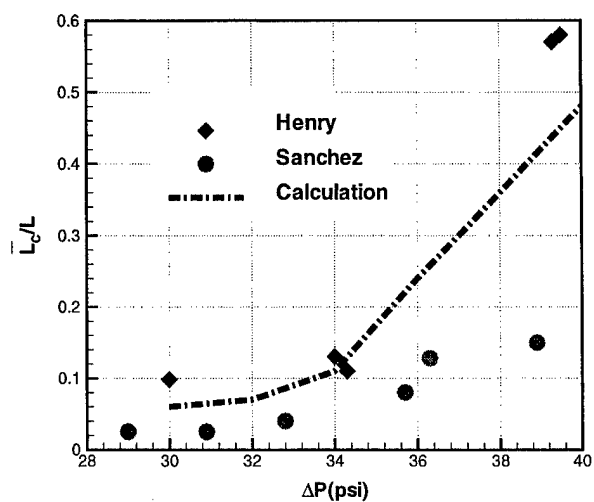


Figure 4.8 Cavitation length,  $L_C$  comparison with experimental results,  
 $L/D = 10.714$

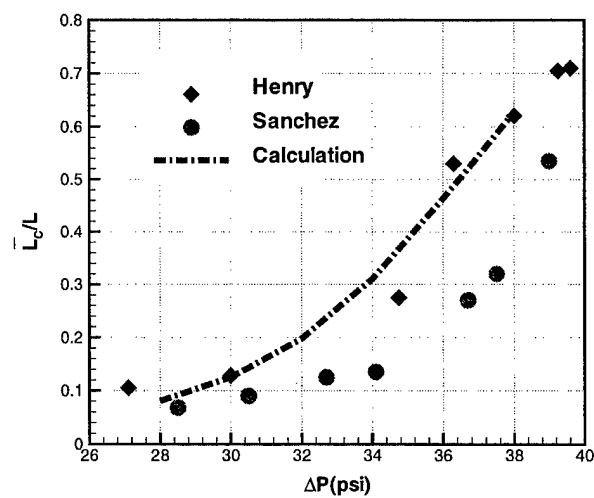


Figure 4.9 Cavitation length,  $L_C$  comparison with experimental results,  
 $L/D = 9.375$

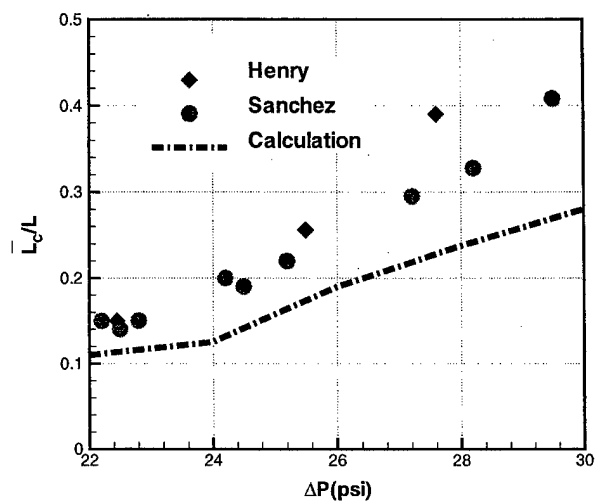


Figure 4.10 Cavitation length,  $L_C$  comparison with experimental results,  $L/D = 6.25$

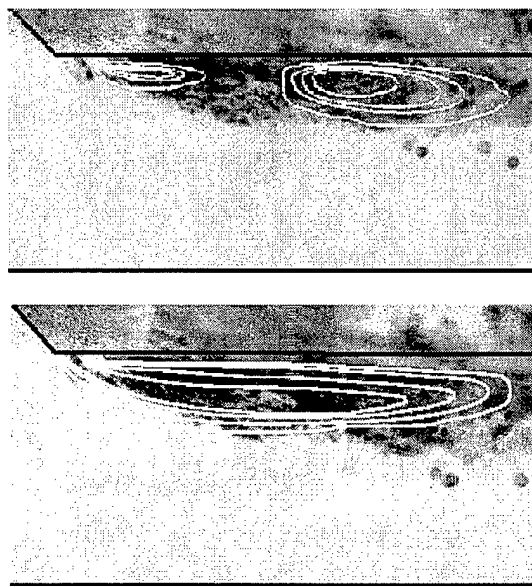


Figure 4.11 Overlays of numerical results and photographic time shot of cavitation region, ( $\Delta P \approx 36 \text{ psi}$ ,  $L/D = 10.714$ ). Here,  $\rho = 0.98$  on the outermost contour with gradients of 0.2 between contours

data is not clear; however, they used different methods for measuring the cavitation length. The computational  $L_C$  for  $L/D = 10.714$  slot lies in between Henry's results and Sanchez's results and is closer to Henry's. The  $L/D = 6.25$  slot shows the poorest agreement between computed results and experimental measurements. The reason for that might be that the collapse and reformation of the bubble cavity tends to be more violent for a shorter slot, and the turbulence model does not account for the turbulence caused by bubble collapse. Although, the turbulence model smears out the oscillations, it generates a cavitation length in acceptable agreement with the experimental data.

The turbulent calculation also produces a single contiguous cavitation region near the inlet corner, consistent with experimental observation. Fig. 4.11 shows density contours, which denote the cavity region, obtained from laminar (the upper one) and turbulent (the lower one) calculations, overlaying one photographic snapshot by Henry. Although the laminar simulation results in an overall cavitation extent consistent with experiment, it indicates two separate regions of cavitation. The turbulence model improves on this point by generating a single cavitation region which appears to be quite consistent with experimental results both in axial and cross-stream directions.

#### 4.3.5 Velocity Fields and Boundary Layer Thicknesses

Fig. 4.12 shows the velocity vectors of the three cases ( $L/D = 10.714$ ) described in Table 4.1. The broken lines in this plot are density contours of a value 0.98. All three cases indicate that the flow reattaches to the wall at the rear end of cavitation region. The close-up of the streamlines near the inlet corner of the case  $\Delta P = 32\text{psi}$  is shown in Fig. 4.13. As seen from this figure the flow separates at the second corner of the bevel.

Fig. 4.14 shows velocity profiles inside the location of the cavity region for cavitating and non-cavitating conditions. The flow inside the cavitation region in general is slower under cavitating conditions than under non-cavitating conditions. Especially

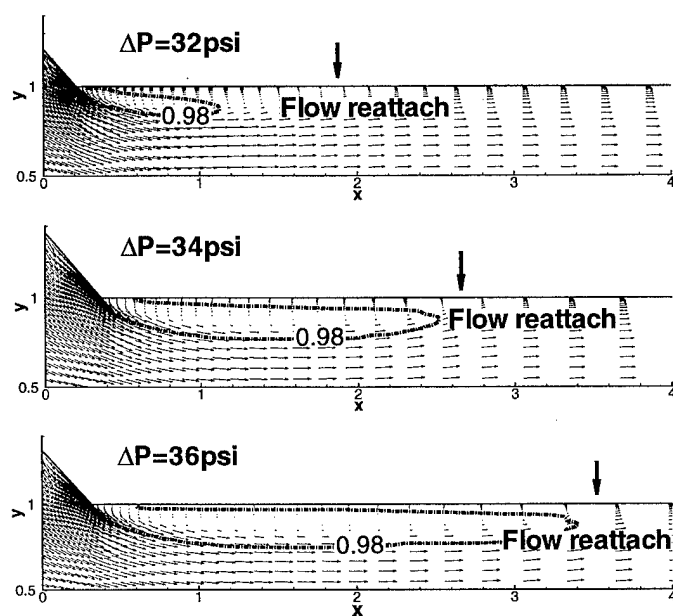


Figure 4.12 Velocity vectors under different partial cavitation conditions, the broken lines are density contours of 0.98

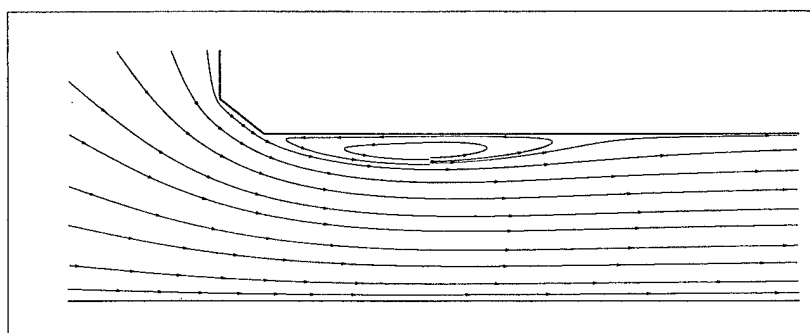


Figure 4.13 The streamlines near the inlet corner,  $L/D = 10.714$ ,  $\Delta P = 32 \text{ psi}$

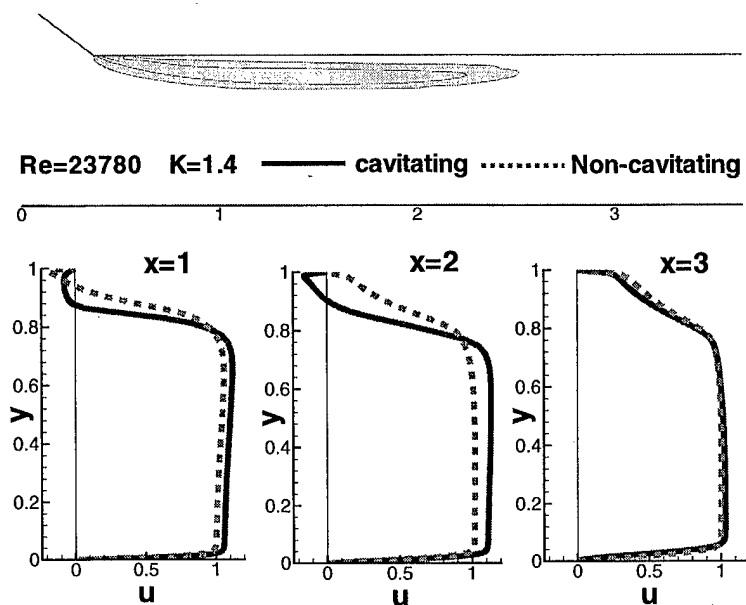


Figure 4.14 Velocity profiles under cavitating and non-cavitating conditions,  
 $Re = 23780$ ,  $K = 1.4$ ,  $L/D = 10.714$

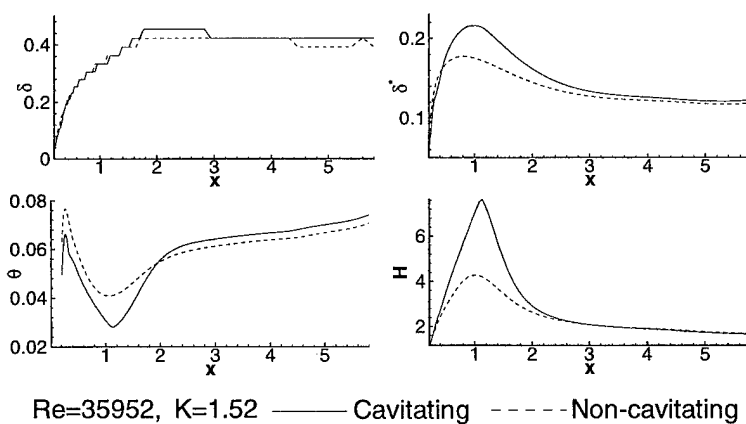


Figure 4.15 Comparison of boundary-layer thickness  $\delta$ , displacement thickness  $\delta^*$ , momentum thickness  $\theta$ , and form factor  $H$ , distribution on the upper wall of a nozzle passage,  $L/D = 6.25$ ,  $Re = 34644$ ,  $K = 1.55$

in the middle of the cavity ( $x = 2$ ), a strong reverse flow occurs between the wall and cavity. At the end of the cavitation region ( $x = 3$ ) the velocity profiles approach the same shape for both cavitating and non-cavitating conditions.

As shown in Fig. 4.15 cavitation has a significant effect on the downstream boundary layer thickness,  $\delta$ , displacement thickness  $\delta^*$ , momentum thickness  $\theta$ . They are defined as

$$\begin{aligned}\delta &= D - y|_{\tilde{u}=0.99\tilde{u}_{max}} \\ \delta^* &= \sum_{D-\delta}^D \left(1 - \frac{\tilde{u}}{\tilde{u}_{max}}\right) \Delta y \\ \theta &= \sum_{D-\delta}^D \frac{\tilde{u}}{\tilde{u}_{max}} \left(1 - \frac{\tilde{u}}{\tilde{u}_{max}}\right) \Delta y\end{aligned}\tag{4.16}$$

where  $\tilde{u}_{max}$  is the maximum  $\tilde{u}$  value in a specific cross section. The cavitation region corresponding to the situation of Fig. 4.15 extends to  $x = 1.12$ . Fig. 4.15 shows the distribution of  $\delta$ ,  $\delta^*$ ,  $\theta$ , and shape factor  $H$  along the streamwise direction for both cavitating and non-cavitating conditions. Even though the turbulence model predicts  $\delta$  distributions which are almost identical for both cavitating and non-cavitating conditions, it produces an increased displacement and momentum thicknesses for cavitating conditions. Previous researchers (Gopalan and Katz, 2000; Kubota et. al, 1992) have observed/predicted the same behavior.

Fig. 4.16 shows the contour of vorticity which is defined as

$$\omega_z = \frac{\partial v}{\partial x} - \frac{\partial u}{\partial y}\tag{4.17}$$

Note the maximum and minimum value of  $\omega$  occurs near the walls. To highlight the interior distribution of  $\omega$  the contour levels have been reduced to such as indicated in the plot. As seen from the plot, high magnitude vorticity exist downstream of the inlet corner where strong recirculation occurs. The plot also indicates a big portion of this internal flow remains irrotational with vorticity close to zero. Fig. 4.17 shows a detail comparison of the distribution of vorticity in normal direction at different axial locations. As the flow moves toward the exit, the maximum value of the vorticity in



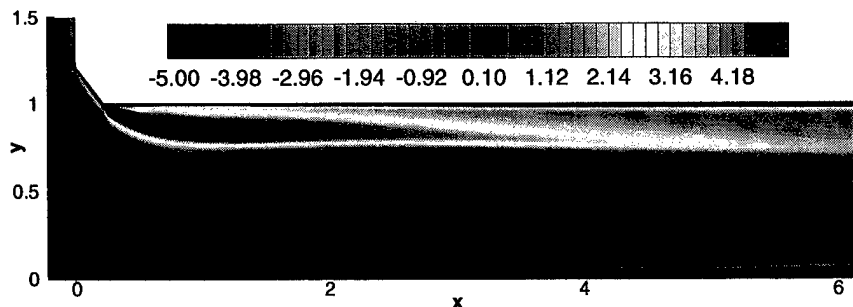


Figure 4.16 The distribution of vorticity,  $L/D = 6.25$ ,  $Re = 34644$ ,  $K = 1.55$

the upper wall boundary layer reduces greatly, however considerable level of vorticity remains at the exit. Note the vorticity level at the edge of the boundary layer of the upper wall is about 0.1.

#### 4.3.6 TKE and Reynolds stresses

We present the contour plots of TKE (turbulent kinetic energy) in figures 4.18, 4.19 and 4.20 for three operating conditions to demonstrate the effect of cavitation on turbulence. The corresponding pseudo density and eddy viscosity contours for each case are also shown in the figures. As seen from the plots, the peak region of TKE locates right at the rear end of cavity region, the wake of the cavity, for all operating conditions. It is well known that the wake where bubble detachment and collapses accompanied with pressure recovery occurs is the most 'turbulent' region. It is interesting to note that the calculation can capture this important phenomenon in cavitating flows. Also note that as bubble cavity becomes bigger (cavitation number getting lower) the location of TKE peak shifts downstream and the peak value of TKE is nearly doubled for the modestly cavitating case (Fig. 4.20) compared with the slightly cavitating case (Fig. 4.18). The distribution of eddy viscosity shows similar behavior to that of TKE. Fig. 4.21 shows the profiles of TKE at the exit for these three cases. One might expect  $k \propto U^2 \propto \Delta P$  or  $\frac{k_1}{k_2} = \frac{U_1^2}{U_2^2} = \frac{\Delta P_1}{\Delta P_2}$ . However, the increase in  $k$  is larger than what is expected based on the increased pressure loss alone. The ratio of the pressure loss  $\Delta P = 36psi$  to  $\Delta P = 28psi$  is 1.29, whereas

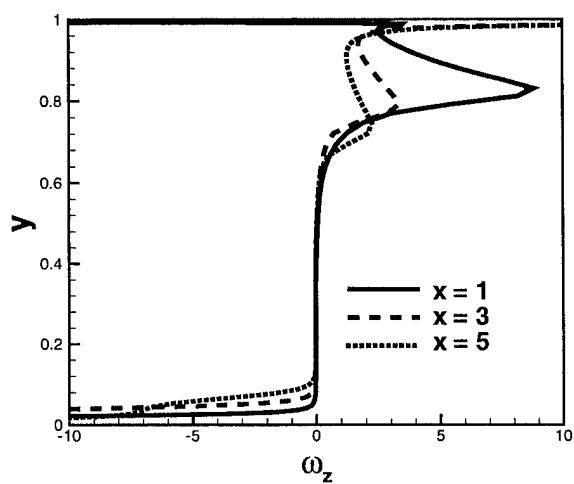


Figure 4.17 Vorticity profiles at different axial locations,  
 $L/D = 6.25$ ,  $Re = 34644$ ,  $K = 1.55$

the ratio of the maximum TKE at the exit of these two cases is 1.71. This indicates cavitation plays a role in the increase of  $k$  value.

The 2-D code was also used to analyze the flow through a slot with the geometry consistent with the one used by Ruiz and He (1999). In this case a sharp cornered,  $L/D = 6$  and  $D = 25mm$ , slot was used. Fig. 4.22 shows turbulence intensities in the streamwise and normal direction and Reynolds shear stress compared with experimental data (Ruiz and He, 1999) at different streamwise locations. Here,  $R_{xx}^{\frac{1}{2}} = \sqrt{\rho u'' u''}$  and  $R_{yy}^{\frac{1}{2}} = \sqrt{\rho v'' v''}$ , representing turbulence intensity in  $x$  and  $y$  directions are the dimensionless mass weighted velocity fluctuation in streamwise and normal directions, and  $R_{xy} = \overline{\rho u'' v''}$  is the mass averaged Reynolds shear stress. The cavitation extent is also shown in this plot. In the experiment, an artificial air filled cavity was introduced near the inlet corner, which is different from a vapor filled cavity generated from cavitation. In the calculation the outflow pressure,  $P_2$  was used as a free parameter (the lower  $P_2$  is, the more likely the flow is to cavitate) to match the cavity extent, which is about one fourth of the slot length. The Reynolds number,  $Re = 11280$ , is the same as that in the experiment.

The turbulence model predicts higher values of turbulence intensity and Reynolds shear stress for cavitating flow conditions than for non-cavitating conditions. Quantitatively the calculation results are comparable to the experimental data. Near the rear end of cavity region the calculation predicts  $R_{xx}^{\frac{1}{2}}$ ,  $R_{yy}^{\frac{1}{2}}$  and  $R_{xy}$  are significantly larger under cavitating conditions than under non-cavitating conditions due to flow reattachment. It should be mentioned the  $k - \omega$  model does not include any production terms due to bubble collapse. The only mechanism to capture turbulence generation for the turbulence model is the occurrence of a strong strain rate. However, due to the presence of cavitation the pseudo density model produces a larger strain rate flow field. It has been observed that the collapse of bubbles is a source of vortex generation (Gopalan and Katz, 2000). Here, we can see a good coordination of the pseudo density model and the turbulence model in terms of the prediction

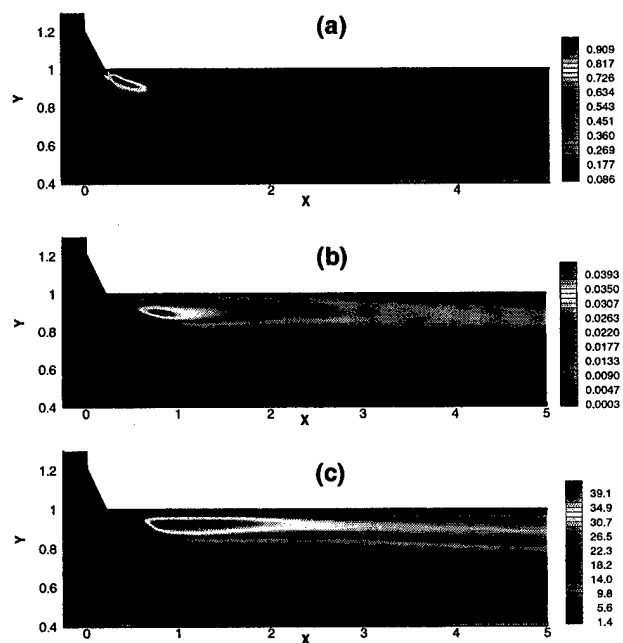


Figure 4.18 (a) Pseudo density contours, (b) TKE (turbulent kinetic energy) contours, (c) eddy viscosity contours.  $L/D = 9.375$ ,  $\Delta P = 28 \text{ psi}$

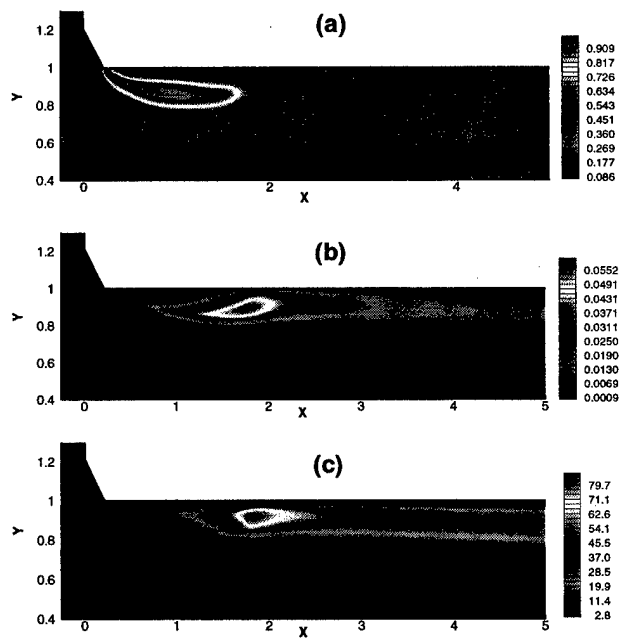


Figure 4.19 (a) Pseudo density contours, (b) TKE (turbulent kinetic energy) contours, (c) eddy viscosity contours.  $L/D = 9.375$ ,  $\Delta P = 32 \text{ psi}$

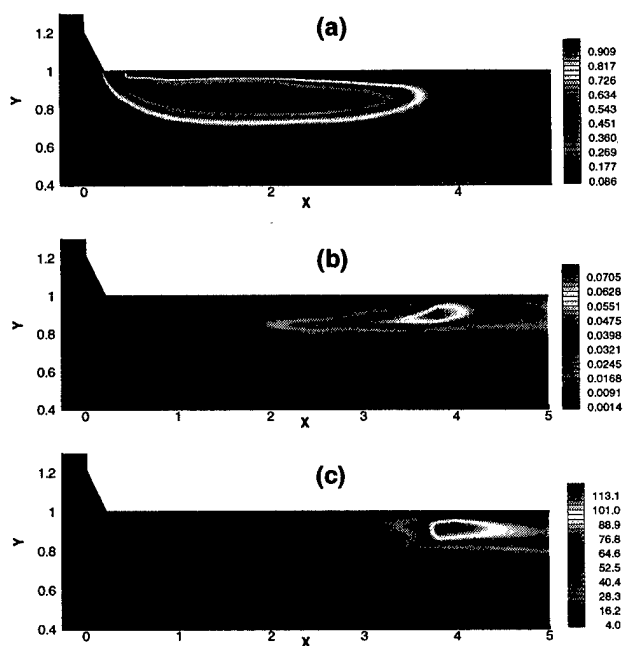


Figure 4.20 (a) Pseudo density contours, (b) TKE (turbulent kinetic energy) contours, (c) eddy viscosity contours.  $L/D = 9.375$ ,  $\Delta P = 36 \text{ psi}$

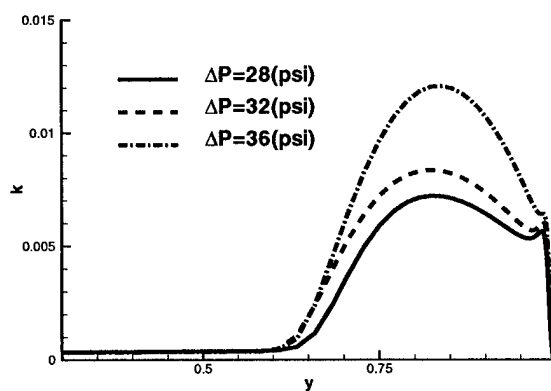


Figure 4.21 Turbulence intensities at the exit under different operating conditions ( $L/D = 9.375$ )

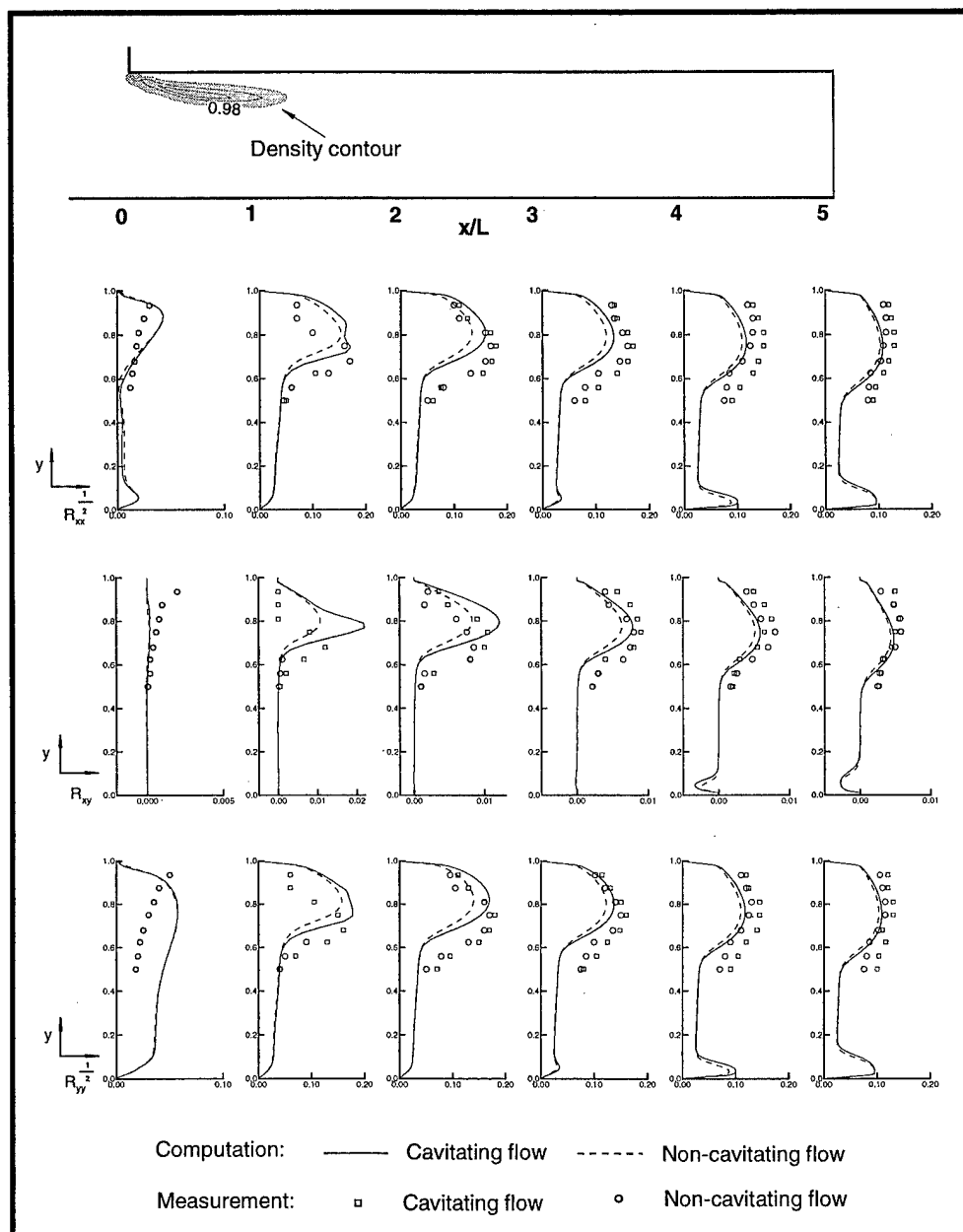


Figure 4.22 Turbulence intensities and mass-averaged Reynolds stress comparison with experimental results at different axial locations, with and without cavitation (turbulent calculation)

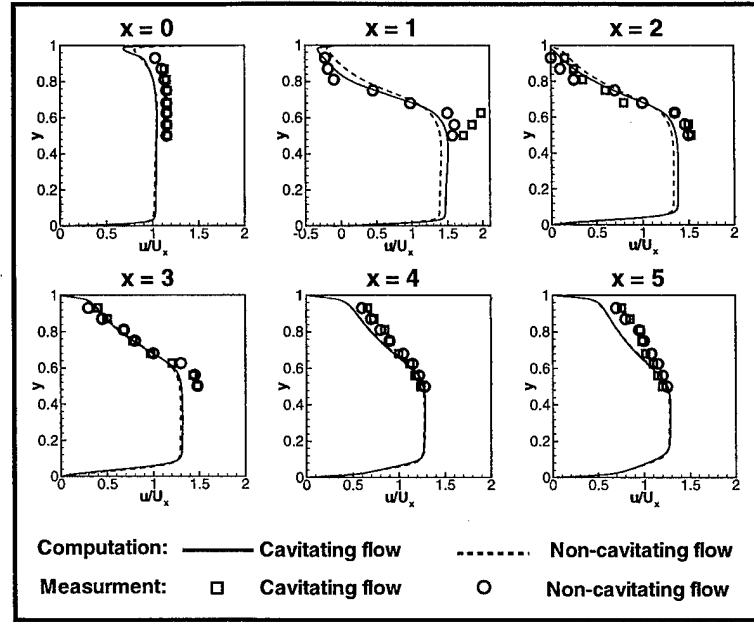


Figure 4.23 Mean axial velocity comparison with experimental results at different axial locations, with and without cavitation

of turbulence quantities in spite of the fact that turbulence production by bubble collapse is not explicitly accounted for.

Fig. 4.23 shows the computed and measured mean axial velocity profiles at different streamwise locations. The velocity is normalized by  $U_x$ , the average mean velocity at the exit. Both the model and measurement have near identical velocity profile for both cavitating flow and non-cavitating flow at all locations except inside the cavitation region ( $x = 1$ ). However, the model underpredicts the potential core velocity inside the slot ( $x = 0, 1, 2, 3$ ), especially for the flow over the cavity ( $x = 1$ ). The reason for that might be of the assumption of no slip between phases employed in the pseudo density model. In reality, the fluid over a bubble cavity tends to move faster.

We also used the laminar code to compute the Reynolds stresses from the unsteady solution. In order to do that, the definition of the Favre average of velocity was utilized.

$$\bar{u}'' = u - \tilde{u} \quad (4.18)$$

Hence, we can express the mass-averaged Reynolds normal stress as

$$\begin{aligned}
 \overline{\rho u'' u''} &= \overline{\rho(u - \tilde{u})^2} \\
 &= \overline{\rho(u^2 - 2u\tilde{u} + \tilde{u}^2)} \\
 &= \overline{\rho u^2} - 2\tilde{u}\overline{\rho u} + \overline{\rho \tilde{u}^2} \\
 &= \overline{\rho u^2} - 2\overline{\rho} \tilde{u}^2 + \overline{\rho \tilde{u}^2} \\
 &= \overline{\rho u^2} - \overline{\rho} \tilde{u}^2
 \end{aligned} \tag{4.19}$$

Similarly, we have

$$\overline{\rho u'' v''} = \overline{\rho uv} - \overline{\rho} \tilde{u} \tilde{v} \tag{4.20}$$

$$\overline{\rho v'' v''} = \overline{\rho v^2} - \overline{\rho} \tilde{v}^2 \tag{4.21}$$

To complete the calculation of the three components of Reynolds stress tensor shown above, the following time-averaged and mass-averaged variables need to be determined first as follows

$$\begin{aligned}
 \overline{\rho} &= \frac{1}{N} \sum_{i=1}^N \rho_i \\
 \overline{\rho u^2} &= \frac{1}{N} \sum_{i=1}^N \rho_i u_i^2 \\
 \overline{\rho v^2} &= \frac{1}{N} \sum_{i=1}^N \rho_i v_i^2 \\
 \overline{\rho uv} &= \frac{1}{N} \sum_{i=1}^N \rho_i u_i v_i \\
 \tilde{u} &= \frac{\overline{\rho u}}{\overline{\rho}} = \frac{1}{\overline{\rho}} \frac{1}{N} \sum_{i=1}^N (\rho u)_i \\
 \tilde{v} &= \frac{\overline{\rho v}}{\overline{\rho}} = \frac{1}{\overline{\rho}} \frac{1}{N} \sum_{i=1}^N (\rho v)_i
 \end{aligned} \tag{4.22}$$

The instantaneous flow fields  $\rho$ ,  $u$ ,  $v$  from laminar calculation were stored to disk during each time step, and  $N$  is the total sample number of each flow variable stored. Fig. 4.24 shows the comparison of Reynolds stresses from laminar calculation and Ruiz and He's measurements. As seen from the figure, the disagreement between the



two sets of data is much bigger, compared with the results from turbulent calculation. Although the laminar calculation generates an unsteady solution, it is not capable of capturing the very small length scale turbulence. On the contrary, regarding the prediction of turbulence intensity the turbulence model does a better job on the same grid resolution.

#### 4.4 Flow through a 2-D Nozzle

Gopalan and Katz (2000) performed an experiment to study the closure region of an attached cavity over a nozzle surface. They presented data on instantaneous and averaged velocity, vorticity and turbulence downstream of the cavitation region when cavitation is very slight. The two dimensional code is utilized to simulate the flow over a nozzle surface whose geometry is consistent with the one in Gopalan and Katz's experiment. The cross section of the water tunnel in the experiment is  $6.35 \times 5.08 \text{ cm}^2$ . Strictly speaking, we should consider this flow field as three-dimensional. But in order to use our existing turbulent code to simulate this flow, we simplify this problem to a two-dimensional flow as Gopalan and Katz did in the measurement.

The computational mesh used is shown in Fig. 4.25. The reference dimension in this case is the length of the curved nozzle surface,  $L$ , as shown in Fig. 4.25. A non-uniform mesh was generated, with dense grid points near upper and lower walls and within the throat section of the nozzle. For clarity, only part of whole computational grid is shown in the plot, and every other index in both normal and axial direction of the grid is skipped. To ensure the accuracy of the calculation the inflow boundary is put at a distance of  $L$  upstream of the beginning point of the nozzle curve, and the outflow boundary was put at a distance of  $2L$  downstream of the end point of the nozzle curve. A grid refinement study similar to that in section 4.3.2 was undertaken, resulting in a grid of  $140 \times 50$  being adequate to resolve the flow field. The velocity profile at  $x/L = 0.3$  was chosen to test the convergence of the solution. The result is shown in Fig. 4.26.

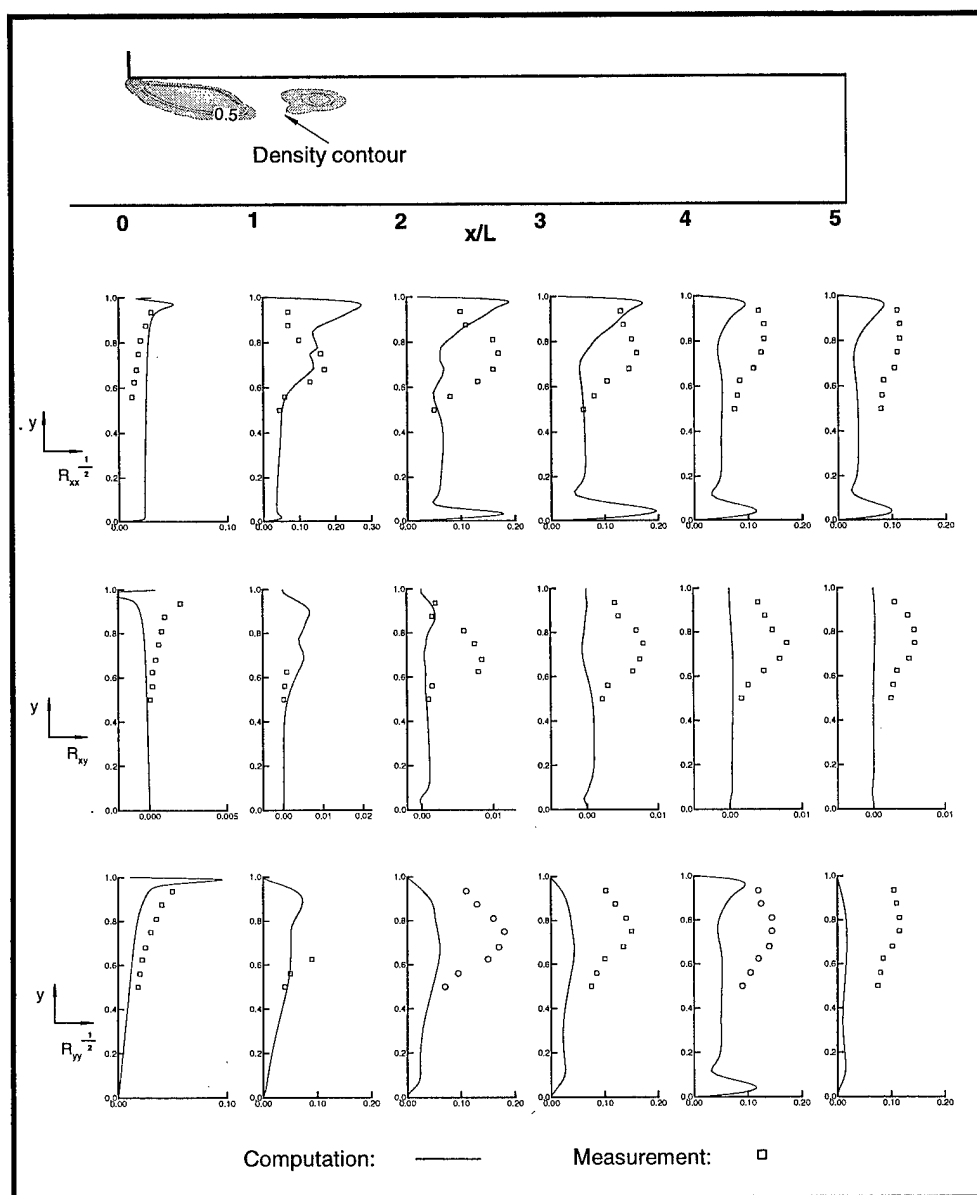


Figure 4.24 Turbulence intensities and mass-averaged Reynolds stress comparison with experimental results at different axial locations, with and without cavitation (laminar calculation)

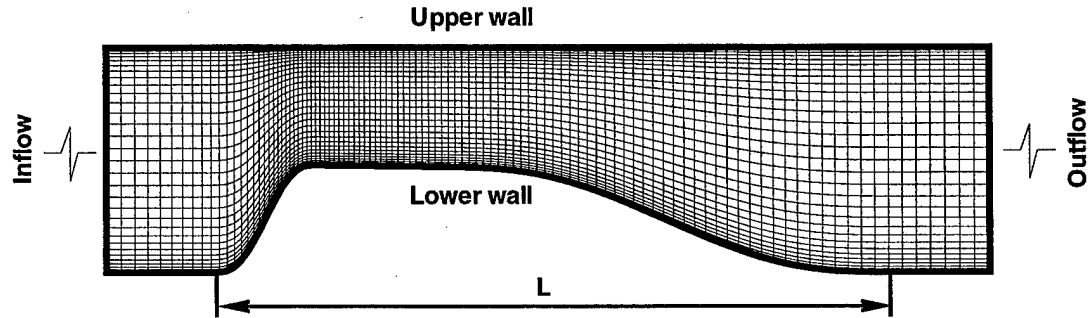


Figure 4.25 Computational mesh for the flow through a nozzle

At the inflow boundary uniform velocity was specified. The other boundary conditions are similar to that of the flow through an injector passage. The inflow turbulence level  $k$  is chosen as 0.1%, a value close to that in reality (Gopalan and Katz). It is found that the solution of this flow is dependent on the inflow value of  $\omega$ . If the inflow  $\omega$  value is set as such that the inflow eddy viscosity is over thousand or more, the unsteadiness in cavitation would disappear completely. To have a better match with the measured cavitation extent, the inflow value of  $\omega$  is chosen as such that the bulk value of the inflow eddy viscosity is unity, a setup similar to that of the orifice flow. However, unlike the orifice flow, under this inflow conditions an unsteady solution is obtained for this flow.

#### 4.4.1 Pressure distribution

First of all, the pressure distribution over the nozzle surface was computed through single phase runs and compared with the computed results of Gopalan and Katz who utilized the commercial CFD code *Fluent*, with RNG  $k - \epsilon$  turbulence model treatment, to carry out their computation. Here, the pressure coefficient  $C_P$  was calculated in the comparison. It is defined as

$$C_P = \frac{P - P_{in}}{1/2 \rho V_{in}^2} \quad (4.23)$$

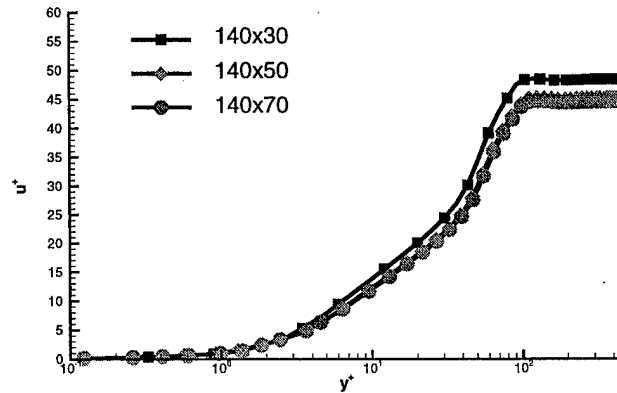


Figure 4.26 Velocity profiles at  $x/L = 0.3$  for various grids

where  $P_{in}$  is the inlet pressure and  $V_{in}$  is the velocity at the inlet. As specified by the geometry of the nozzle surface, a particle of fluid will experience the following four typical phases (presumably there is no flow separation) as it passes over the surface: an increase in pressure near the leading edge, sharp decrease in pressure to the minimum value, quick recovery to pressure lower than outlet pressure, and gradual recovery to pressure close to outlet pressure.

Fig. 4.27 shows the evolution of the  $C_P$  distribution from the  $k - \omega$  model calculation and the results of Gopalan and Katz. As seen from the plot, *Fluent's* RNG calculation reproduces all the four phases mentioned above. Although, in the early stage of the calculation ( $t=0.5$ ) the  $k - \omega$  model generates a nearly identical pressure distribution as *Fluent* does, after a very short time, the recovery of pressure downstream of  $x/L = 0.5$ , where a strong adverse pressure gradient is present, is destroyed. The reason for that is boundary layer separation. We may refer to figures 4.28 and 4.29 which show velocity vector plots at  $t=0.5$  and  $t=3$ , respectively. They indicate that there is no any flow separation at  $t=0.5$ , while a big recirculation zone present near the trailing edge at  $t=3$ , which destroys the pressure recovery. It is clear that the  $k - \omega$  model and *Fluent's* RNG model generate different pressure distributions. We would like to reproduce the pressure distribution as *Fluent* does. For this purpose,

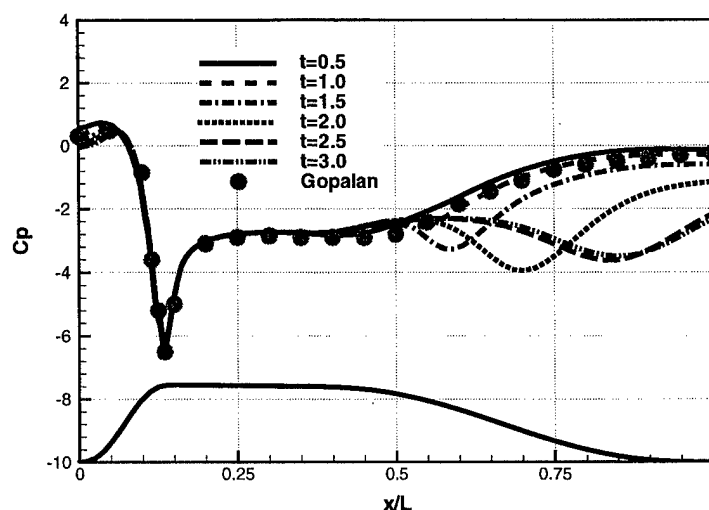


Figure 4.27 Pressure distribution from  $k - \omega$  calculation

we developed our own RNG code, using the model formulation in Wilcox(1998), and made a run to compute the pressure distribution. The results due to the RNG model is shown in Fig. 4.30. Our implementation of the RNG model has a behavior similar to that of the  $k - \omega$  model does, except that it produces a pressure recovery closer to Gopalan's result. But there still exists discrepancy between the two sets of data. The reason for that is not clear. One possibility is that the turbulence model implemented in *Fluent* is proprietary and , therefore, the results can not be matched exactly.

Another issue is that Gopalan and Katz did not show a comparison of experimental result and the *Fluent* result. Therefore, it is not certain that the *Fluent* results is correct. Further more, Our computed results can be partially validated by Gopalan and Katz's experiment in the following aspects. First, the measurement shows that the ratio of the maximum velocity to the inlet velocity is 2.4, whereas this ratio for our computed velocity is 2.6. Second, there are no boundary layer separation in the high adverse pressure gradient region downstream of the minimum pressure point in both the  $k - \omega$  calculation and the experiment. However, given the comparison of our cavitating flow calculation with experiment, it is clear that our turbulence model predicts too large a separation near the trailing edge of the nozzle.

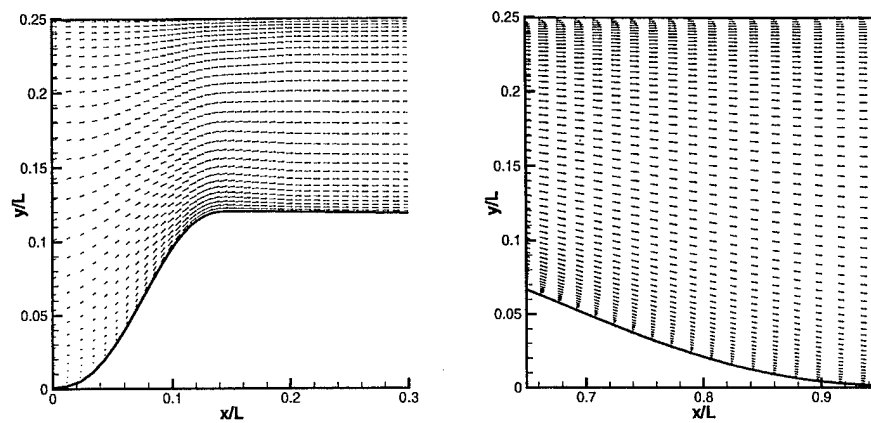


Figure 4.28 Velocity vector with no flow separation, at  $t = 0.5$ , the  $k - \omega$  model calculation

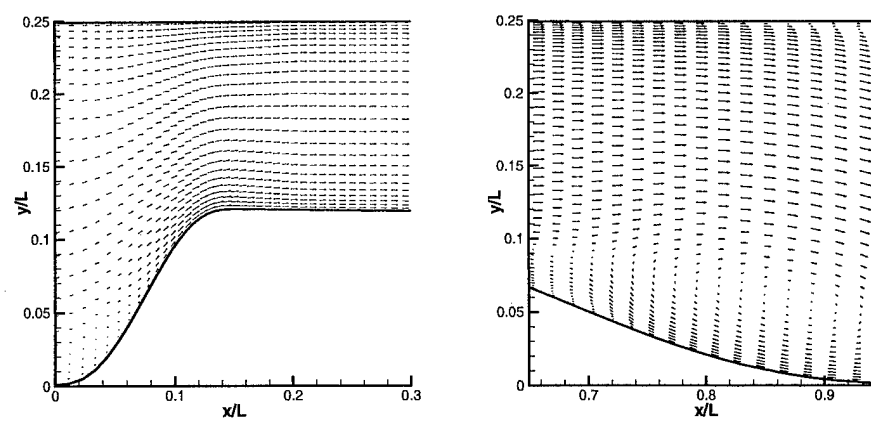


Figure 4.29 Velocity vector with flow separation at  $t = 3$ , the  $k - \omega$  model calculation

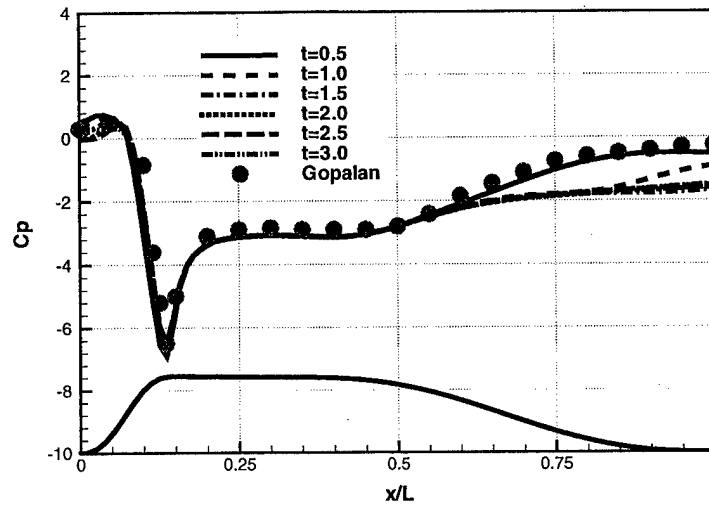


Figure 4.30 Pressure distribution from RNG model calculation

#### 4.4.2 Cavitation extent

For this flow, the cavitation number is defined as

$$K = \frac{P_{in} - P_v}{1/2 \rho V_{in}^2} \quad (4.24)$$

Gopalan and Katz observed that as cavitation number is reduced slightly below the inception level, a cavity with limited extent occurs just downstream of the minimum pressure point, with a “blunt, glossy” leading edge and hairpin-like structure downstream of the closure region. If the pressure level of the system is reduced further (decrease in cavitation number), cavitation will develop into an advanced stage with a massive bubble cloud shed downstream.

In 1995, to validate the pseudo density model Chen and Heister made extensive comparison of cavitation region with experimental data for flows over a conic head and an ogival head which are analogous to this flow, and they got satisfactory matches with the measurements. To further validate the turbulent code, we run it for the flow condition of  $K = 2.5$  under which the flow reaches an advanced cavitation stage. The computed density contours for five numerical snapshots in time are compared with

Gopalan and Katz's experimental photographic shots of the cavitation region at different instances, and the results are shown in Fig. 4.31. In the plot, the experimental snap shots have a light region that denotes the vapor cavity, on the contrary the computed density contours have a dark region which denotes the cavity region with the outmost contour corresponding to  $\rho = 0.98$ . The comparison shows an overall qualitatively good match between the measurement and computation. However, as the cavity extends longer downstream (the two frames at the bottom of the plot), the experiment shows the bubbly cloud region spreads wider both in axial and normal direction as compared with the computed pseudo density contours. The numerical results seem to over collapse the bubble cloud. The reason for that might be that in the wake of the cavitation region the effect of vortex stretching and shedding is dominant and our calculation is two-dimensional which does not allow vortex stretching to occur.

We also performed a case study of  $K = 4.69$  which is slightly lower than the inception cavitation index, with inlet velocity  $V_{in} = 5.2m/s$  and Reynolds number  $Re = 1.58 \times 10^6$ . Under this situation an attached cavity, whose length varies slightly in time but with no massive detached cavity patches, exists just downstream of the minimum pressure point. To compare with experimental measurement for this case, the time average procedure similar to that of section 4.3.6 was performed on the instantaneous flow variables of density, and velocities. Thus all the following analysis are based on the the averaged flow fields. The computed cavity region was compared with Gopalan and Katz's measurement, and the results are shown in Fig. 4.32. The inset shows the global position and overall extent of the cavity which is pretty small and slender. As seen from the plot, the predicted cavitation region is in good agreement with the measured data.

The detailed streamline near the cavity region was shown in Fig. 4.33. The contours of the pseudo density with  $\rho = 0.6$  at the outmost is shown in the plot. Because of the presence of the cavity the flow is pushed away from the wall, and pulled back at the rear end of the cavity due to the recovery of pressure there. A typical flow



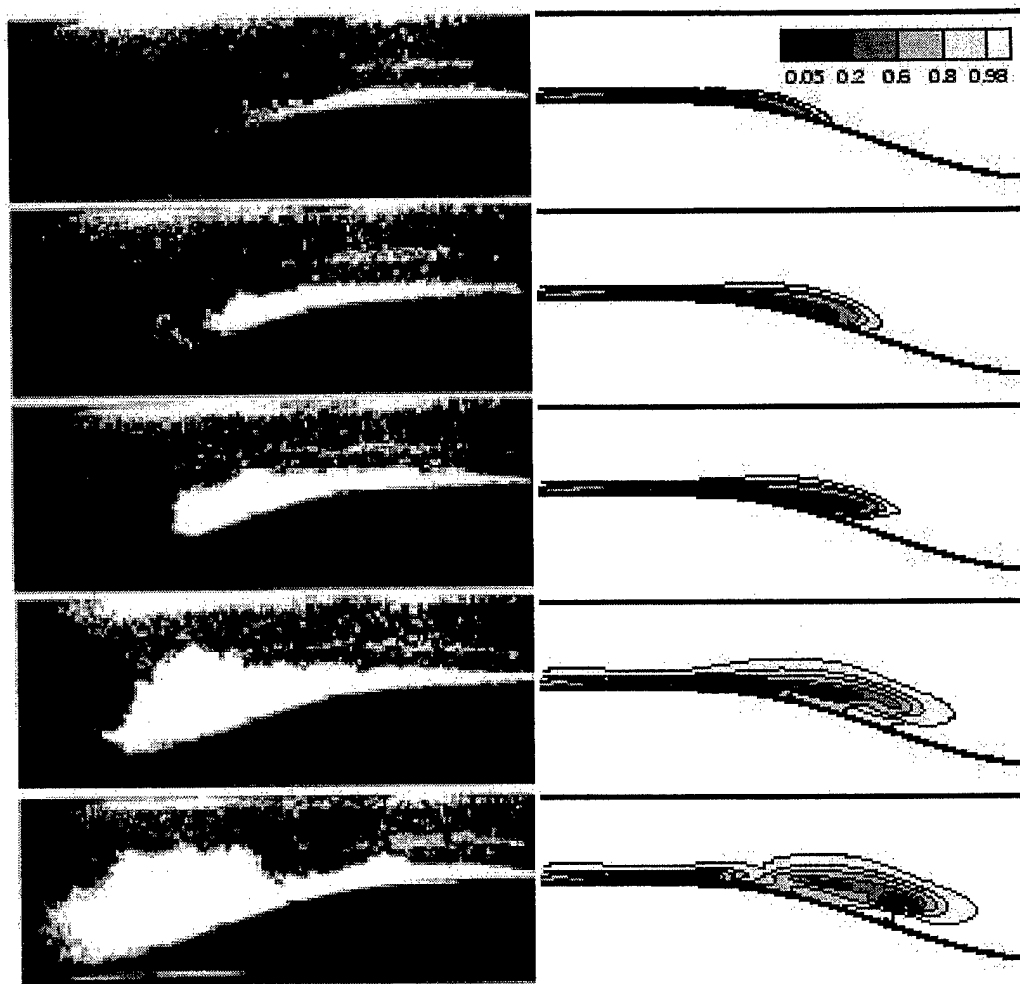


Figure 4.31 Experimental photographs of different stages of unsteady cavitation region (left side), and computational pseudo density contours (right side)

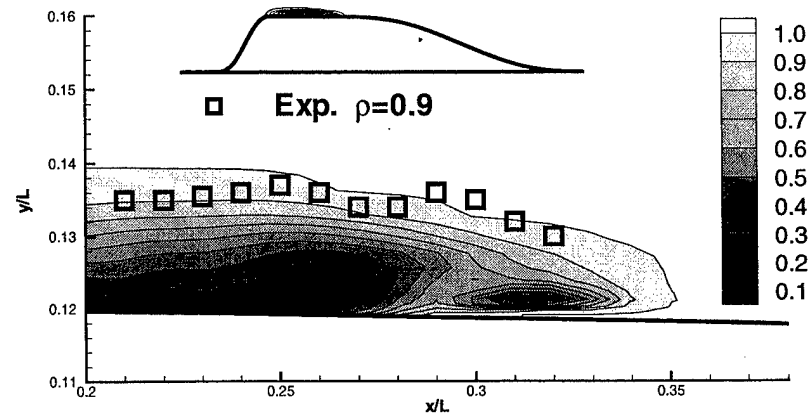


Figure 4.32 Distribution of pseudo density of the rear portion of an attached cavity

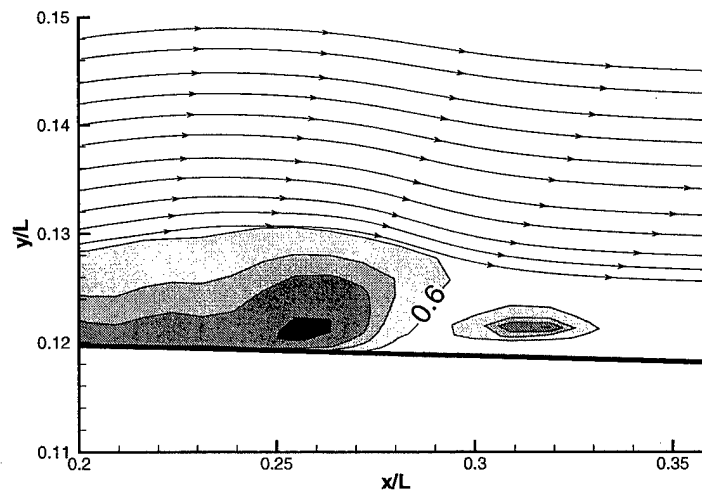


Figure 4.33 Streamline near around the rear portion of an attached cavity

structure around such a cavity would be that the flow separates from the wall at the leading edge of the cavity, passes over the cavity body, and reattaches to the wall at the trailing edge of the cavity. In other words, the presence of cavity serves as an extension of the geometry of the surface which further increases the adverse pressure gradient that might not be strong enough to cause the flow separation in a single phase flow. Many researchers regard flow reattachment as the reason for the existence of the reentrant flow under the cavity. Because the cavity is small and slender in this case, the additional cavity-induced adverse pressure gradient is slight. In our calculation we did not see a reentrant structure existing beneath the vapor region. This is consistent with Gopalan and Katz's observation in their experiment.

Fig. 4.34 shows the distribution of the Reynolds normal stresses  $\overline{\rho u''u''}$ ,  $\overline{\rho v''v''}$  and shear stress  $\overline{\rho u''v''}$ . As seen from the plot, the computation predicts high turbulence levels close to the cavity and in the downstream region. As mentioned in the previous section, this is because of the high strain rate in those regions which is captured by the model. Although, Gopalan and Katz observed the same trend, there exists big discrepancy in the detailed structure of the contours between the measured and computed results in terms of the manner and pattern of the distribution of the stresses. The measured high turbulence level region is closer to the wall compared with the computed results. Fig. 4.35 shows the computed and measured displacement and momentum thicknesses of the boundary layer in the closure region. Compared with the measurement, the computation generate too much displacement and momentum deficit in the boundary layer. It overpredicts the thicknesses more than two times larger than the measured ones. Furthermore, the typical form factor of a turbulent boundary layer is about 1.3, while the computed value of this variable is about 1.43. The measured form factor is about 1.2 at  $x/L = 0.25 - 0.35$ , and it approaches 1 further downstream. The cause of the discrepancies might be due to the inherent drawback in turbulence modeling, the averaging simplification which throws away all the instantaneous information of the flow field. One other reason is because we are

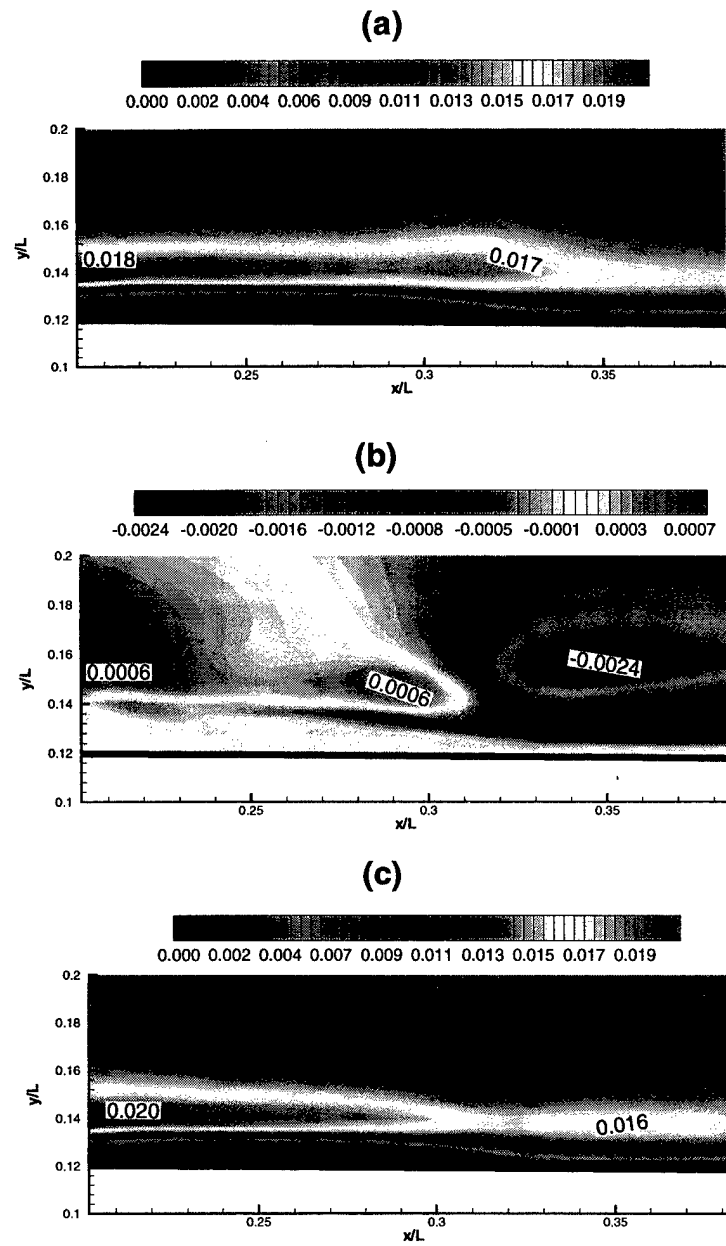


Figure 4.34 Contours of Reynolds stresses at the rear portion of an attached cavity:  
 (a)  $\overline{\rho u'' u''}$ , (b)  $\overline{\rho u'' v''}$ , (c)  $\overline{\rho v'' v''}$

using a traditional single phase turbulence model which does not take into account the effect of phase changes.

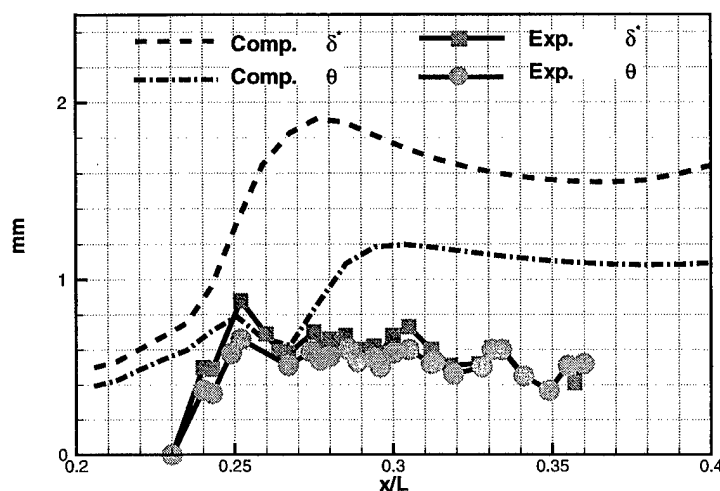


Figure 4.35 Displacement and momentum boundary layer thickness and comparison with experimental measurement

#### 4.5 Conclusions

The homogeneous pseudo density model and the  $k - \omega$  turbulence model were used to approximate cavitation two-phase flows. Simulations of the cavitating flow in an injector slot/orifice were undertaken. The result is found sensitive to the inflow condition of  $\omega$ . The inflow condition is set as such that the cavitation length does not vary with the change of this variable at the inflow boundary, and a steady solution is obtained. Turbulence model shows slight improvement in prediction of the discharge coefficient. The prediction of cavitation length has various performance for different length/diameter ratio slot, and worst agreement with experiment result is obtained for the shortest slot. The computed mean velocity and Reynolds stresses profiles show good agreement with the measured results. Computation also indicates the trend of cavitation increasing the displacement and momentum thicknesses, turbulence intensities which is in accord with experimental observations.

Simulations of the cavitating flow through a two-dimensional nozzle were also performed. The computed pressure distribution from the  $k - \omega$  model calculation does not agree with the *Fluent's* results due to predicting too large a separation. However no experimental results are available to validate these two calculations. The overall matches of the computed cavitation region to the experimental photographic shot of advanced cavitation and measurement of attached cavitation are very well. The computation also indicates high turbulence intensity develops around an attached cavity. However the pattern of the distribution of the Reynolds stresses does not agree with the measured ones. In addition, the models overpredicts the momentum and displacement deficit of the boundary layer in the closure region.

## 9 Appendix C - 3D Cavitating Flow Simulations

Xu, C., "Simulation of Orifice Internal Flows Including Cavitation and Turbulence" Ph. D. Thesis, School of Aeronautics and Astronautics, Purdue University, West Lafayette, IN, August 2001, pp. 82 - 100. 1996.

## 5. 3D CAVITATING FLOW SIMULATIONS

### 5.1 Introduction

Orifice flows driven by the cross flow in a manifold occur in many atomization devices, such as the injector of a diesel engine and a liquid rocket engine. The three-dimensional nature of this particular flow and the potential of it easily becoming cavitating make numerical modeling of it a great challenge. In 2000, Bunnell and Heister investigated the flow inside this geometry by solving the fully three-dimensional, unsteady, two-phase Navier-Stokes equations, with cavitation being treated by the homogeneous fluid model. They investigated the effect of cavitation on orifice mass flow, and found cavitation acts as a slipstream which tends to decrease the discharge velocity at the exit, and thus the mass flow rate. Experimentally, Strakey and Talley (1999) have investigated the effect of manifold cross flow on the discharge coefficient of an orifice. They found that the discharge coefficient closely correlated with the cross flow velocity. The discharge coefficient can be decreased as much as 50% as the cross flow velocity is increased beyond a certain value.

In this chapter, the fully three-dimensional two-phase Navier-Stokes solver developed by Bunnell (1999) is utilized to simulate an orifice flow driven by a manifold cross flow. The effects of the cross flow velocity on cavitation length and discharge coefficient are investigated. The characteristics of this internal flow field are also analyzed based on the results from the calculation. The computed discharge coefficient is compared with Strakey and Talley's measurement. The details of the development and numerics of the model are described by Bunnell (1999). Here, the results of the simulation are provided in the following section.



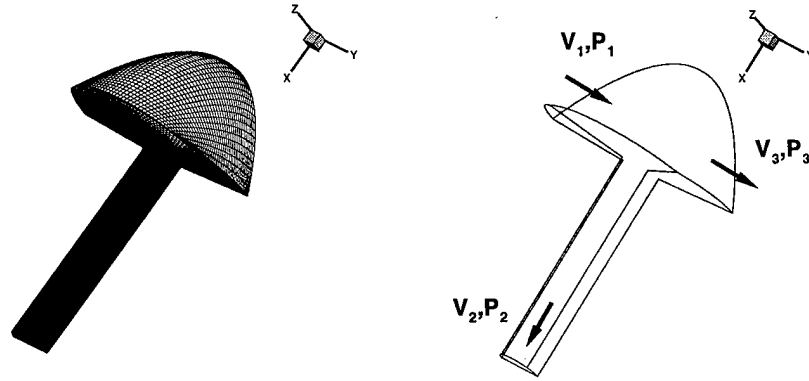


Figure 5.1 3-D manifold cross flow model and key parameters, from Bunnell (1999)

## 5.2 Case Descriptions

Fig. 5.1 shows the schematic representation of the three-dimensional manifold cross flow. In the figure,  $V_1$  is the cross flow velocity, and  $V_2$  is ideal discharge velocity at the exit, calculated from Bernoulli's equation. In this study, eight simulations were conducted on an orifice with diameter  $D = 2.03mm$  and aspect ratio  $L/D = 5$ . In all the cases, the upstream pressure is held as  $P_1 = 0.69MPa$ , a value which was used in Strakey and Talley's experiment. By varying the back pressure of the orifice, hence the cavitation number, and the cross flow velocity, we get the various operating conditions used in the simulations. They are shown in Table 5.1 (Note cases 4, 5, and 6 were simulated by Bunnell. For completeness, we list all of them in the table).

The operating conditions are consistent with those used by Strakey and Talley in their experiment. Therefore it is possible for us to make comparison of the predicted discharge coefficient with the measurements. All the simulations were performed using a mesh of  $120 \times 42 \times 42$  as recommended by Bunnell. In order to save computing time, for each simulation the first 30,000 time steps were carried out as single phase flow calculation, and after that it was run as two phase flow calculation. A typical run takes 3-4 weeks on two Pentium 650HZ PCs. Because it is very time-consuming, only 5 simulations were performed in this study. Those data and the three cases run

Table 5.1 Operating conditions simulated

Case	$V_1(m/s)$	$K$	$\bar{L}_C/L$
1	6.0	1.2	0.56
2	6.0	1.6	0.04
3	6.0	6.0	0
4*	8.9	1.2	0.72
5*	8.9	1.8	0.02
6*	8.9	6.0	0
7	12.1	1.2	1
8	15.1	1.2	1

\* from Bunnell (1999)

by Bunnell, complete the comparison with Strakey and Talley's measurement for one orifice geometry ( $L/D = 5$ ).

### 5.3 Results

The cavitation length history for cases 1 and 2 are shown in Fig. 5.2. Here,  $L_C$  is the length of the cavitation zone as defined as the most downstream point where pseudo density is 0.98. As found before, cavitation number is an important parameter in determining whether or not the flow becomes cavitated. If cavitation number is low, ie. the discharge pressure level is close to the vapor pressure, the cavitation inside the orifice becomes prominent. The computed averaged cavitation length for each cases is shown in Table 5.1. In this series of simulations, when  $K = 1.2$ , for all cases where cross flow velocity ranges from  $6.0m/s$  to  $15.1m/s$ , a highly developed cavity occurs inside the orifice. As cavitation number increases to 1.6 ( $V_1 = 6.0m/s$ ) or 1.8 ( $V_1 = 8.9m/s$ ), cavitation reduces dramatically in both cases. With a further

increase in this number to 6.0, the flow remains non-cavitating completely for any of the values of cross flow velocity simulated in this study.

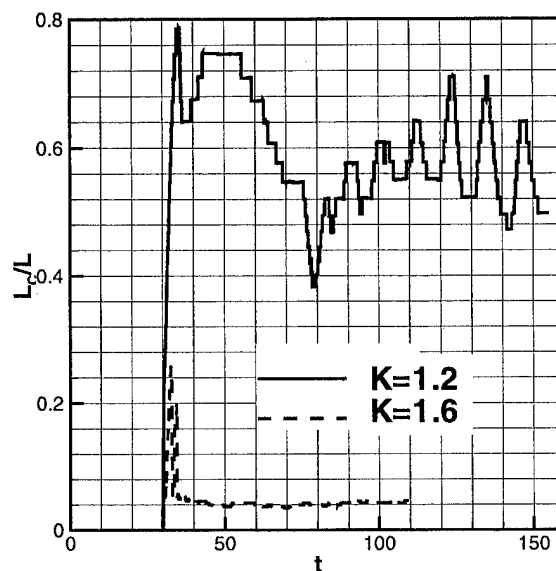


Figure 5.2 Cavitation length history,  $V_1 = 6.0 \text{ m/s}$

Fig. 5.3 shows the cavitation length history for various cross flow velocities when  $K = 1.2$ . As seen from this plot, the other point is evident that cavitation becomes more significant as the flow moves faster across the orifice in the manifold. This happens because with increased cross flow velocity the separated region at the leeward corner, where cavity develops, becomes larger. This trend agrees with the observations of Strakey and Talley. However, the dominant factor that determines the extent of cavity is still the cavitation number. This point can be verified by comparing cavitation length of cases 2 and 5. Case 2 corresponds to a larger cavity because of the lower cavitation number, even though its cross flow speed is less than that of case 5. Strakey and Tally found that the cavitation inception index is about 1.8. Due to the high expense of this computation, we can not afford to determine the the exact inception cavitation number, but the computed cavity is very small when

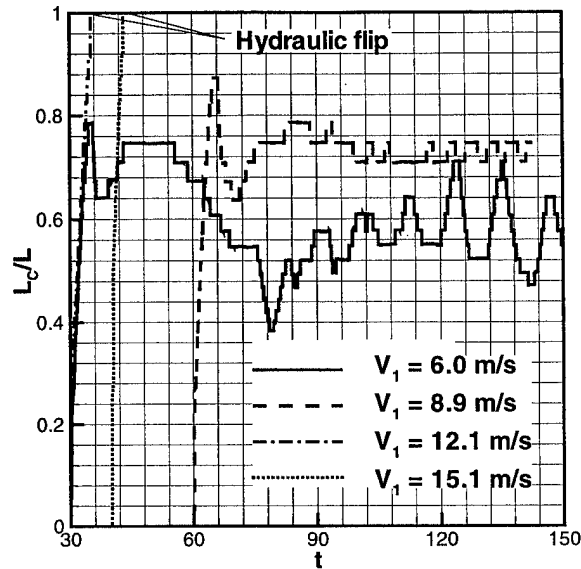


Figure 5.3 Cavitation length history for various cross flow velocity, when  $K = 1.2$  cavitation number used in the simulations (cases 2 and cases 5) are equal or close to the measured inception index.

Fig 5.4 shows the history of the discharge coefficient for the cases of  $V_1 = 6.0 \text{ m/s}$ . Bunnell and Heister had a thorough analysis of the unsteady characteristics of the discharge coefficient before. Here we observe the same periodic behavior of the discharge coefficient as they did. As seen from the plot, the oscillation in the discharge coefficient still exists for the non-cavitating case due to the instability induced by the vena-contracta. For the cavitating cases, after carefully examining the curves of the discharge coefficient and that of their corresponding cavitation length, we can see the instant at which the discharge coefficient reaches its peak lies in the increasing phase of the cavitation length, somewhat slightly later than the instant at which cavitation length reaches its peak. This indicates that the increase in the volume of the cavity pushes a larger amount of liquid out of the exit, on the other hand during the shrinking phase of the cavity more liquid is refrained inside the orifice.

Figure 5.5 shows the comparison of the computed average discharge coefficient and the experimentally measured discharge coefficient. Note the average value is obtained by sampling the data after it reaches a steady oscillation state (For the case of  $K = 1.2$ , we should run the code longer. But as seen from the plot, a nearly steady oscillation state is obtained for this case. The average discharge coefficient for this case is obtained by sampling the data between  $t=116-150$ ). Although the number of computed data is fewer than that of the experimental results because of the high expense of the computation, two patterns can still be observed from the plot. First, for a given cross flow velocity, as cavitation number increases the discharge coefficient increases at first. After reaching the maximum value, discharge coefficient then begins to drop off. The maximum value in discharge coefficient occurs when the cavitation number is about 1.8, a value close to the experimentally measured inception index. The reason for that is the following. The mass flow rate is proportional to the pressure drop through the orifice (increasing with decreasing cavitation number) before the inception of cavitation. When the pressure loss is large enough to cause cavitation to occur, the mass flow rate begins to drop due to the slipstream effect of the cavity as pointed out by Bunnell and Heister. The more significant cavitation becomes, the lower the mass flow rate is. The limited computed data samples reproduce this feature as the experimental counterparts do, except that they overpredict the discharge coefficient in general, especially when  $V_1 = 8.9m/s$  and  $K = 6.0$ . The overprediction might be due to the lack of turbulence in the modeling or because the grid is not fine enough (Bunnell, 1999).

The second trend observed in Fig. 5.5 is with regard to the effect of cross flow velocity. Both the computation and experiment show that as cross velocity increases, discharge coefficient decreases. This phenomenon can be attributed to the increase in velocity ratio, the ratio of the cross flow velocity to the ideal orifice discharge velocity  $V_1/V_2$ , (Strakey and Talley, 1999). With increasing velocity ratio, less amount of fluid passes through the orifice.

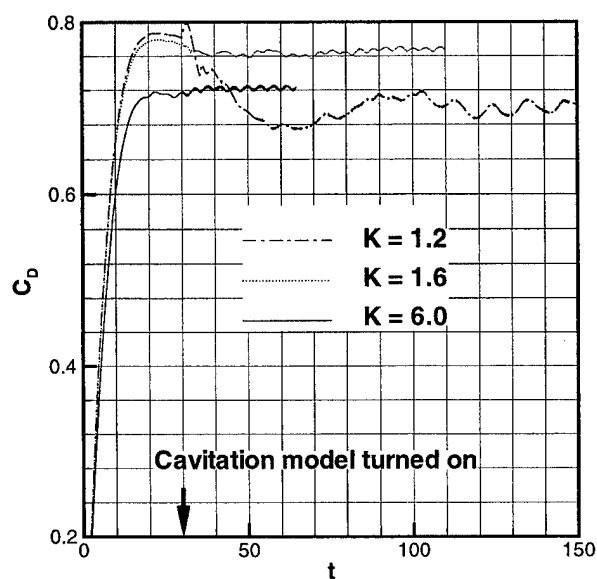


Figure 5.4 Discharge coefficient history,  $V_1 = 6.0 \text{ m/s}$

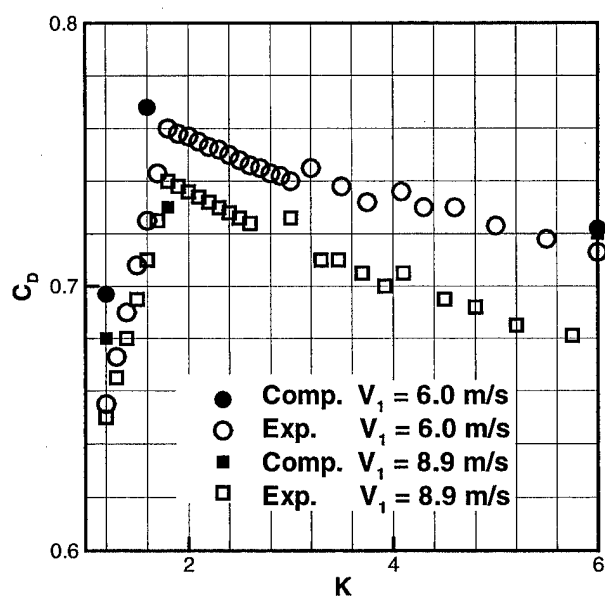


Figure 5.5 The effect of cross flow velocity on discharge coefficient and the comparison with experiment measurement

Table 5.2 Computed average discharge coefficient, its RMS oscillation and oscillating frequency, with cross flow velocity  $V_1 = 6.0m/s$

$K$	$\overline{C}_D$	$\Delta C_D$	f (KHZ)
1.2	0.697	0.00616	1.50
1.6	0.768	0.00165	3.69
6.0	0.722	0.00163	2.00

Table 5.2 shows the computed average discharge coefficient as well as its RMS oscillation and oscillating frequency for the cases where  $V_1 = 6.0m/s$ . The data show a pattern similar to what we found for the axisymmetric flows (Chapter 2), when cavitation occurs longer cavities tend to oscillate at lower frequency. Also note that the variation of mass flow is increased dramatically for highly cavitated flow because the oscillation of the size of the bubble cavity is the primary cause of the variation.

To help us understand how the three-dimensional bubble cavity evolves, the iso-surface on which the pseudo density is 0.98 and the slice-contour of the pseudo density at different instants in time are shown in figures 5.6 through 5.9 and figures 5.10 through 5.13, respectively. In figures 5.6 through 5.9, the cross flow is from left to right and green lines are streamlines. In figures 5.10 through 5.13, the location and orientation of the contour planes are indicated in the three-dimensional inset in the figures, and for the angular plane the flow is from right to left.

The four instants indicated in the plots lie within one cycle of the quasi-periodic oscillation of the cavity (refer to Fig. 5.2). As seen from figures 5.10 through 5.13, the shape of the forepart of the cavity is nearly unchanged in time in both circumferential and radial directions. However, in the wake region, the shape and extent of the rear part of the cavity varies considerably with time. In the growth phase of the cavitation length ( $t = 122, 124$ ), cylindrical like structures exist at the rear part of the cavity. This is similar to what was found by researchers (Kubota, et al.; 1992), based on

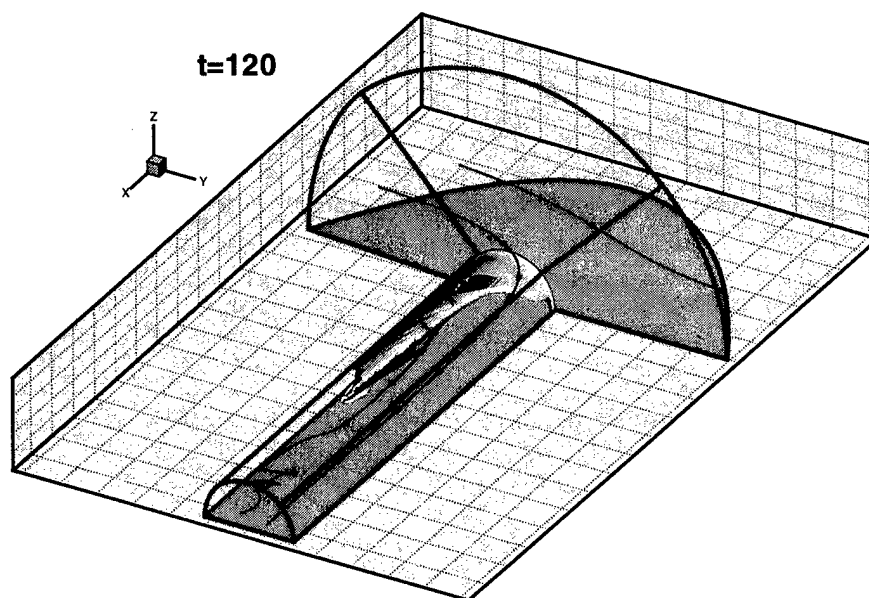


Figure 5.6 (a) Iso-surface plot of pseudo density,  $\rho = 0.98$ , at  $t = 120$ ,  $V_1 = 6.0m/s$ ,  $K = 1.2$ .

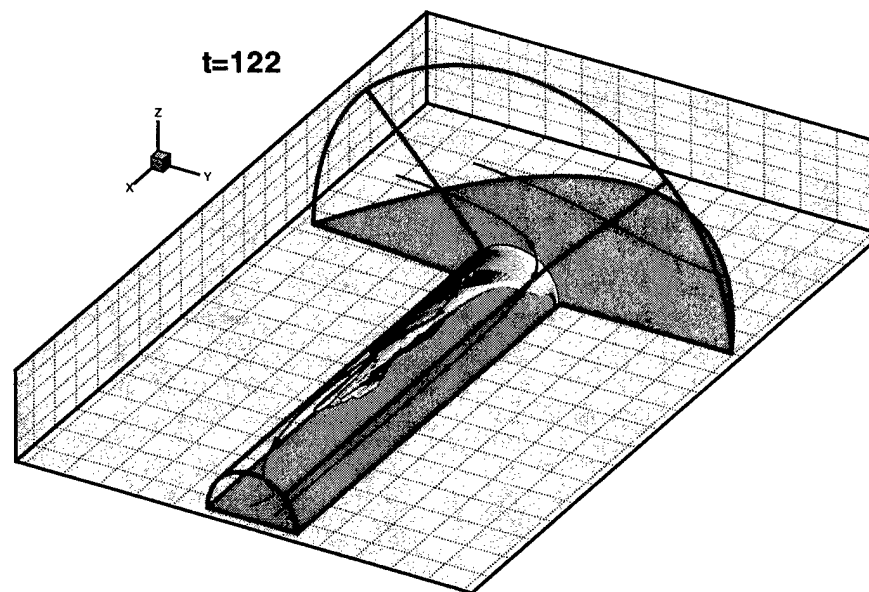


Figure 5.7 (b) Iso-surface plot of pseudo density,  $\rho = 0.98$ , at  $t = 122$ ,  $V_1 = 6.0m/s$ ,  $K = 1.2$ .



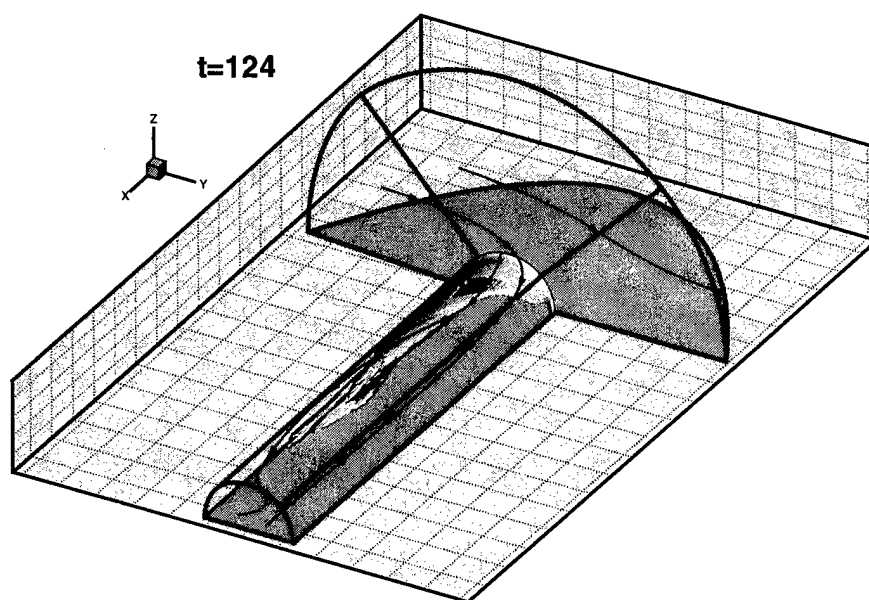


Figure 5.8 (c) Iso-surface plot of pseudo density,  $\rho = 0.98$ , at  $t = 124$ ,  $V_1 = 6.0m/s$ ,  $K = 1.2$ .

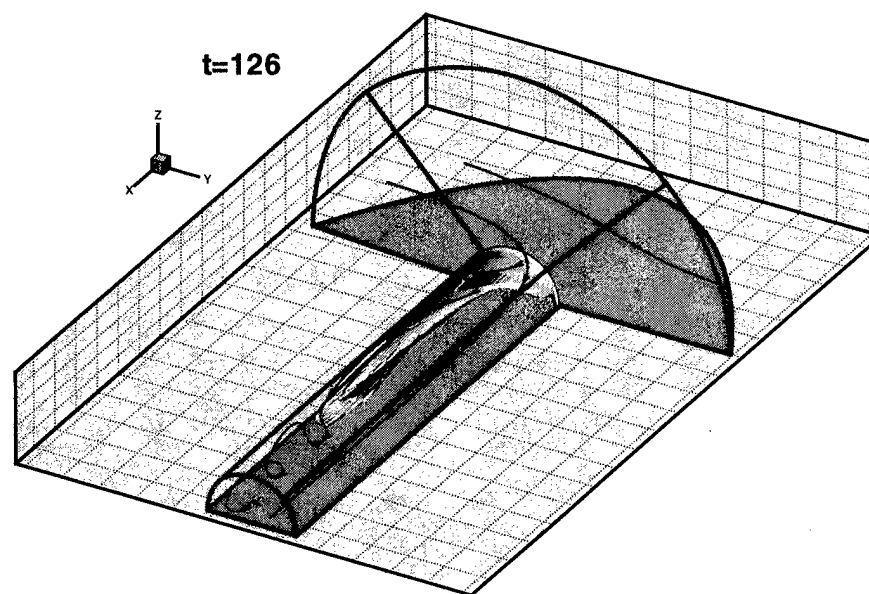


Figure 5.9 (d) Iso-surface plot of pseudo density,  $\rho = 0.98$ , at  $t = 126$ ,  $V_1 = 6.0m/s$ ,  $K = 1.2$ .

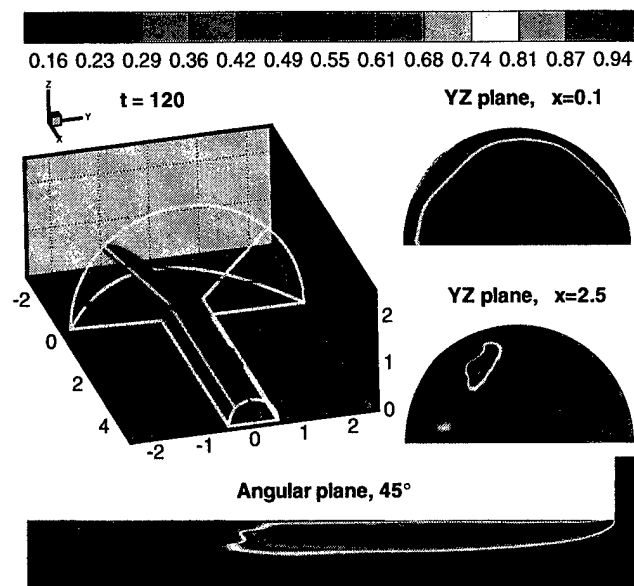


Figure 5.10 (a) Pseudo density slice-contour at  $t = 120$ ,  $V_1 = 6.0m/s$ ,  $K = 1.2$ .

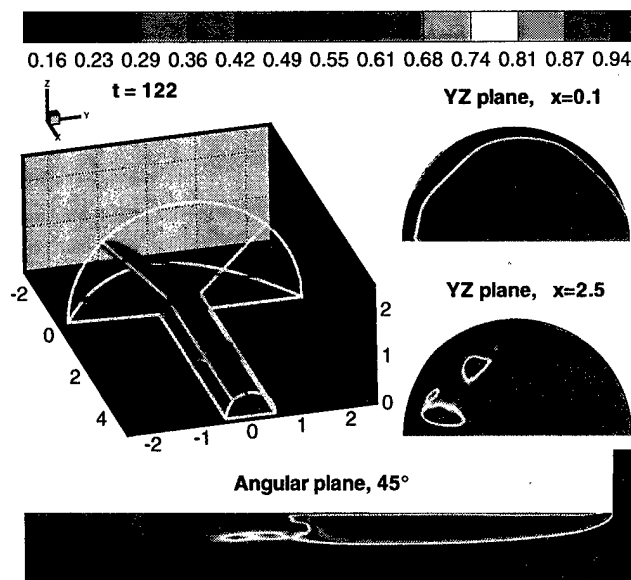


Figure 5.11 (b) Pseudo density slice-contour at  $t = 122$ ,  $V_1 = 6.0m/s$ ,  $K = 1.2$ .

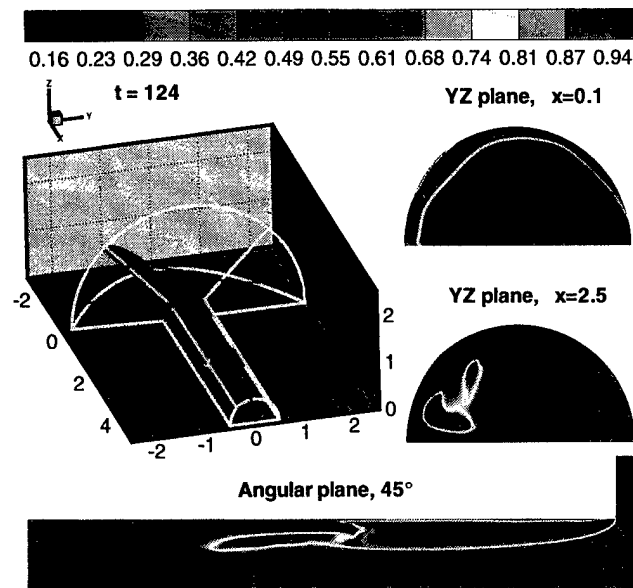


Figure 5.12 (c) Pseudo density slice-contour at  $t = 124$ ,  $V_1 = 6.0m/s$ ,  $K = 1.2$ .

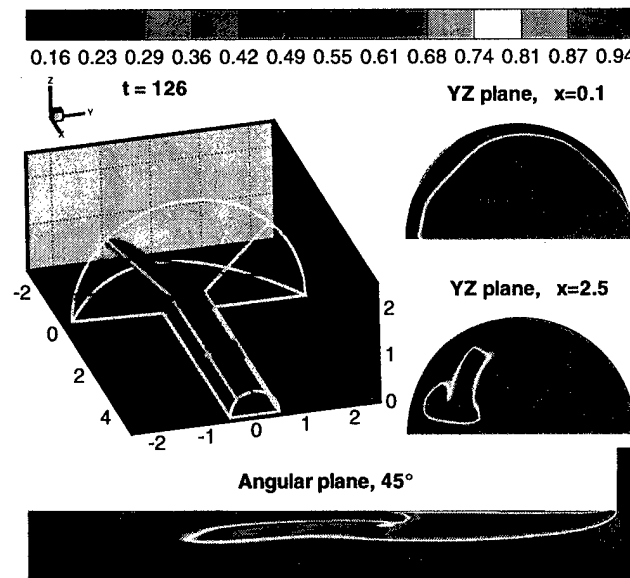


Figure 5.13 (d) Pseudo density slice-contour at  $t = 126$ ,  $V_1 = 6.0m/s$ ,  $K = 1.2$ .

the observation of the cavitating flow over a hydrofoil, that the breakup of sheet cavitation generates large cylindrically shaped bubble clouds shed downstream.

Also note the three stream lines, which begins at fixed locations. The changes of these three specific streamlines highlight the variation of the flow structures of this cavitating flow during a cycle of the growth and shrinking of the cavity. The streamline on the windward side is straight and nearly unchanged with time, however the one on the leeward side is highly sinuous. The sinuousness or twisting of the streamline on the leeward side indicates large eddies are generated downstream of bubble cavity.

Soteriou et al. (2001) have found strong vortex structures exist inside the orifice when cavitation occurs based on their observation on a large scale nozzle. Vortex interaction can also be observed under non-cavitating conditions. The vortices inside the nozzle sometimes intertwine with each other. Fig. 5.14 shows the photographic shot of a vortex intertwining structure inside an orifice, and Fig. 5.15 shows the vortex structure of a diesel spray. Contrary to the traditional theory that the aerodynamic interfacial shear is the dominant force that causes the breakup of the fuel injected from the orifice, Soteriou et al. indicated that the primary factors inducing atomization are associated with the characteristics of the internal flow inside the nozzle.



Figure 5.14 An experimental photographic snapshot of vortex structure inside an orifice. [From Soteriou et al. (2001), used by permission]

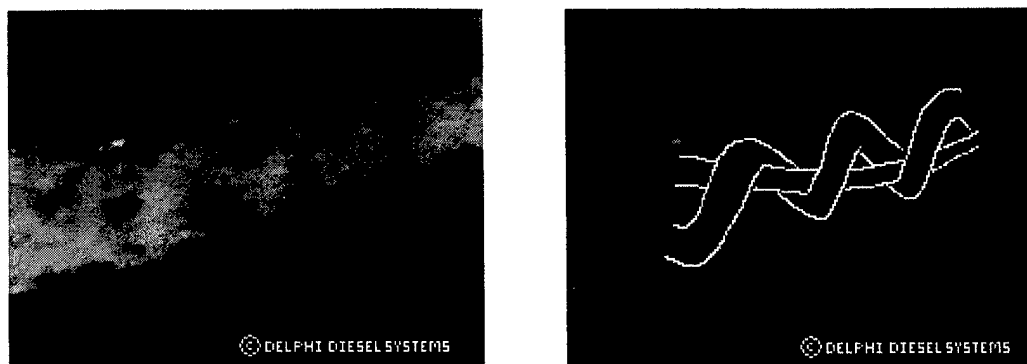


Figure 5.15 An experimental photographic snapshot of vortex structure of diesel sprays, on the right of the plot the dominant structure is outlined. [From Soteriou et al. (2001), used by permission]

Fig. 5.16 and 5.17 show the various computed vortex lines inside the orifice at one instant in time for the conditions with and without cavitation, respectively. At other instants, both flow conditions show a vortex structure similar to what are shown in these two figures. The three component of vorticity are in line with streamwise, cross and vertical directions. The source that generates vorticity is the shear stress in the viscous boundary layer. The vortex structures exist inside the orifices indicates that the vorticity generated from the boundary layer upstream of the separation as well as that generated from the local boundary layer is convected into the fluid in the core region.

Note that each vortex line in Fig. 5.16 has a corresponding counterpart in Fig. 5.17 that starts at or goes through the same location. However, as seen from the plots, the difference between the vortex structure under cavitating condition and that under non-cavitating condition is significant. For non-cavitating case, in the front section of the orifice, the cross or vertical components of the vorticity are dominant. The few vortex lines shown in the figure are nearly parallel to each other and perpendicular to streamwise direction. Based on these representing vortex lines, we believe vortex sheet-like structures exist near the wall region in the front section of the orifice. In the rear section of orifice, the streamwise component of the vorticity start to be dominant.

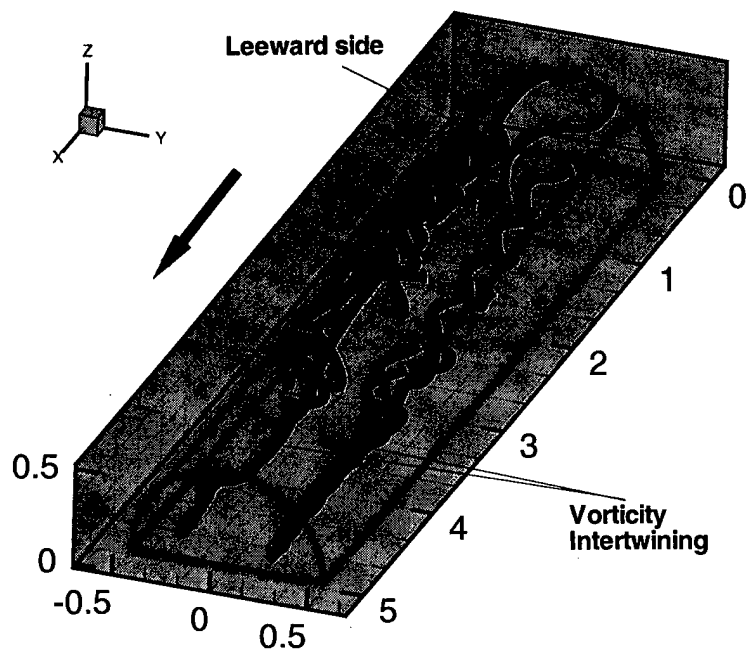


Figure 5.16 Vortex structure inside the orifice under non-cavitating condition,  $V_1 = 6.0 \text{ m/s}$ ,  $K = 1.2$ . Green lines are vortex lines outlined parallel to local vorticity vector

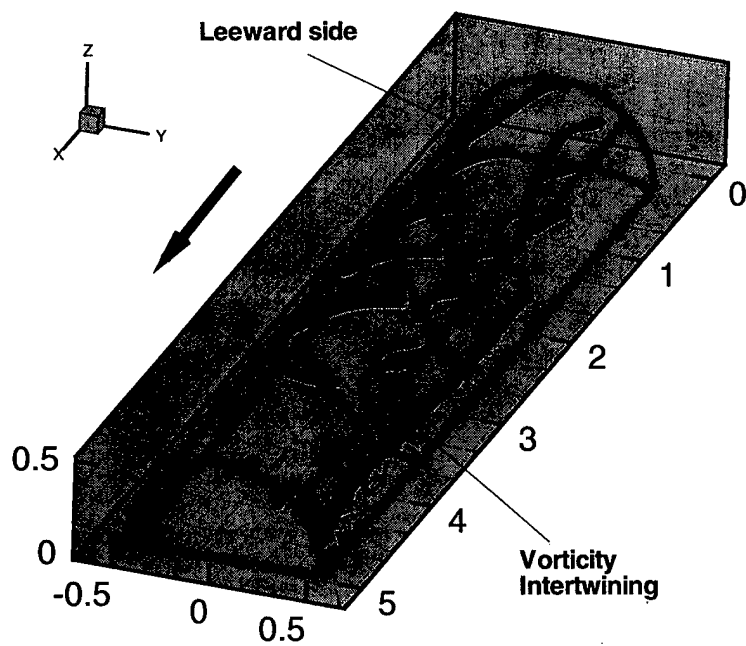


Figure 5.17 Vortex structure inside the orifice under non-cavitating condition,  $V_1 = 6.0 \text{ m/s}$ ,  $K = 6$ . Green lines are vortex lines outlined parallel to local vorticity vector

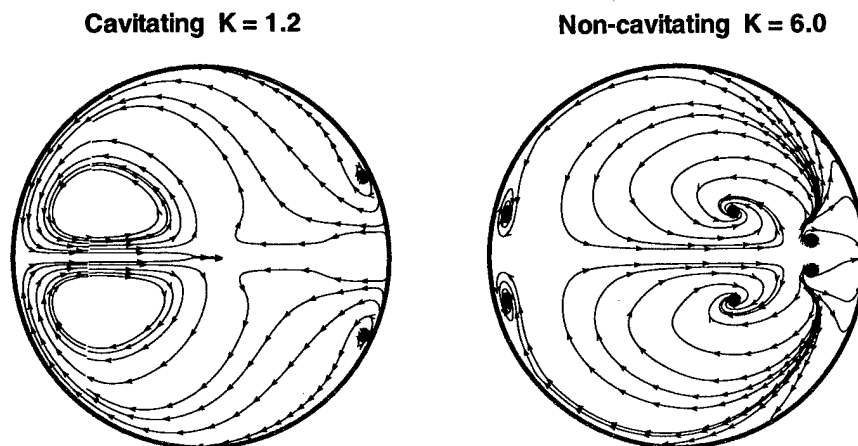


Figure 5.18 Exit plane velocity streamlines,  $V_1 = 6.0 m/s$ . The right of circles is the leeward side.

The vortex sheet starts to roll up and several vortex lines intertwine and form a strong vortex structure on the windward side of orifice.

For the flow with cavitation, vortex interaction begins earlier on the leeward side and two primary vortex structures are formed at the exit of orifice. These vortex structures indicates that swirls with rotating axis in line with streamwise direction exist at the exit. This phenomenon has been observed by Bunnell and Heister, and can be evidenced by figure 5.18 which shows the streamlines of the cross and vertical components of the velocity vector on the exit plane. It is interesting to note that more than one swirls exist on the exit plane for non-cavitating condition. Fig. 5.19 shows the contour of the streamwise component of the vorticity vector,  $\omega_x$ , at the exit plane. Combining figures 5.18 and 5.19, we can see as counter-rotating swirls exist in the upper part and lower part of the exit plane the sign of  $\omega_x$  changes accordingly.

Fig. 5.20 shows the exit-plane-contour of the magnitude of the vorticity vector, which is defined as

$$|\omega| = \sqrt{\omega_x^2 + \omega_y^2 + \omega_z^2} \quad (5.1)$$

where  $\omega_x$ ,  $\omega_y$  and  $\omega_z$  are the three components of the vorticity vector. Note the maximum or minimum contour value of the three variables plotted in these two plots

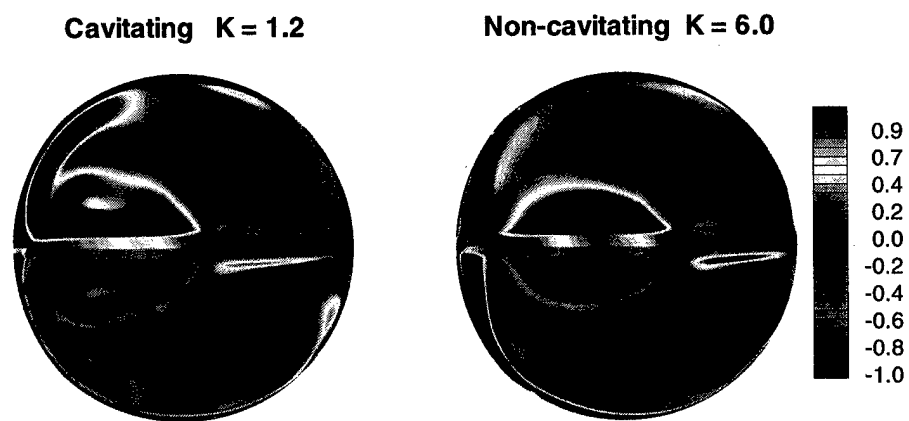


Figure 5.19 Contour plot of the streamwise component of vorticity vector on exit plane,  $V_1 = 6.0m/s$ . The right of circles is the leeward side.



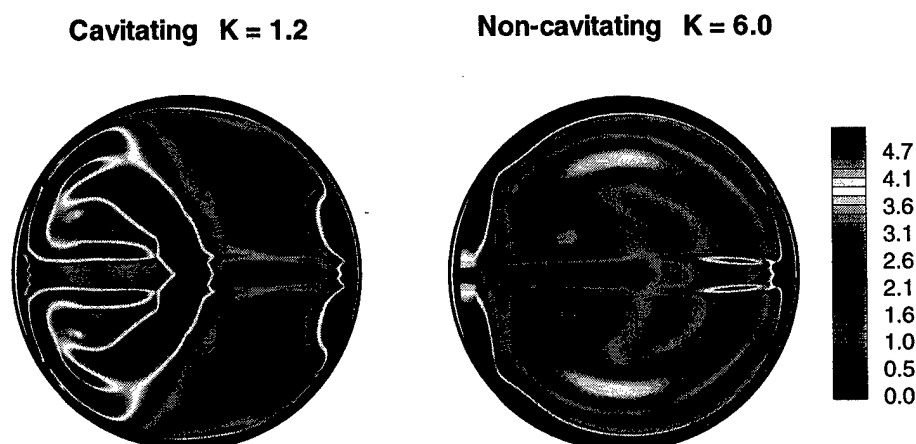


Figure 5.20 Contour plot of the magnitude of vorticity vector on exit plane,  $V_1 = 6.0m/s$ . The right of circles is the leeward side.

occurs near the wall region. To highlight the structure of the interior domain, the contour minimum and maximum levels have been reduced such that the interior structure is obvious. As seen from Fig. 5.20, for cavitating flow, the vorticity on the leeward side is much higher than that on the windward side. On the contrary this distribution seems even for the non-cavitating flow, but with considerable smaller magnitude of vorticity vector on the leeward side. Also, figures 5.18 and 5.20 indicate that at the center of a swirl the magnitude of the vorticity vector does not reaches its maximum value.

The contours for the magnitude of the vorticity vector on the angular plane inclined  $45^\circ$  with respect to the cross flow vector at an instant in time under cavitating and non-cavitating conditions are shown in Fig. 5.21. The flow is from left to right in the figure. As seen from this plot, the flow turns into the orifice with very low-level vorticity in the core region. But after the separation, the magnitude of the vorticity in the interior part of the domain increased greatly for both cavitating and non-cavitating flows. The difference made by cavitation is that the vorticity at the exit is stronger for a cavitating flow.

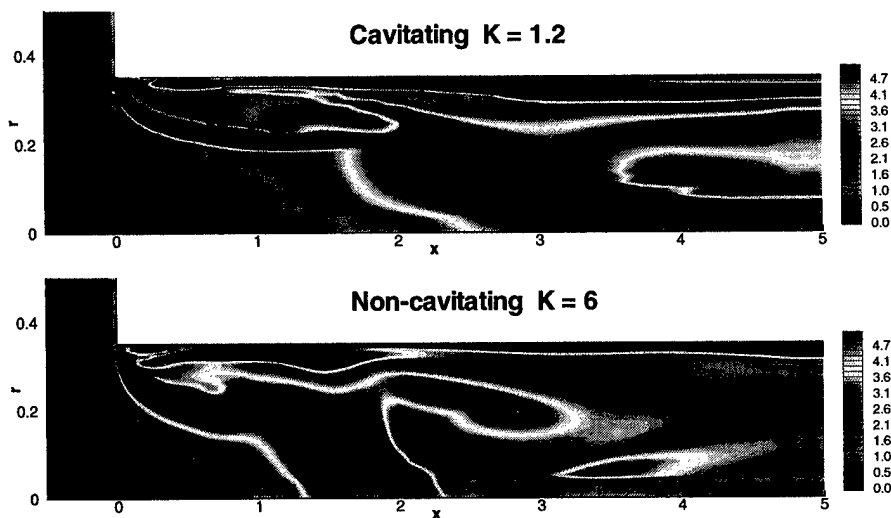


Figure 5.21 Contour plot of the magnitude of vorticity vector on angular plane,  $V_1 = 6.0 \text{ m/s}$ .

#### 5.4 Conclusions

A series of numerical simulations have been performed to study the flow inside an orifice driven by a manifold cross flow. The effect of cavitation number and cross flow velocity on cavitation length and mass flow rate has been examined. The cavitation number is the primary factor that indicates to what degree the flow would become cavitating. However, the cross flow velocity also has a considerable effect on the extent of the cavitation region. For a given cavitation index at which cavitation would occur, increasing cross flow velocity increases cavitation and can promote a hydraulic flip condition. The presence of cavitation acts as a slipstream that tends to reduce the mass flow rate through the nozzle, and a more advanced cavitation situation corresponds to less mass flow rate. Therefore, an increase in cross flow velocity causes a decrease of the mass flow rate through the orifice.

The flow field inside the orifice under both cavitating and non-cavitating conditions has also been assessed. The three-dimensional cavity grows and shrinks quasi-periodically with cylindrical structures formed at its rear part. These structures can be interpreted as bubble clouds shed downstream. Streamwise vortex intertwining

structure has been found for both cavitating and non-cavitating flows. However, the vortex interaction tends to start earlier as the flow begins its journey inside the orifice with the presence of cavitation. The role played by the internal vortex structure on spray atomization is not well understood since it is both a numerical and an experimental new discovery. Recently some authors (Hiroyasu, 2000; Soteriou et al., 2001; Tamaki et al., 1998) have suggested that cavitation inside the orifice is an important factor that promotes atomization. This might be attributed to the difference made by cavitation on the internal flow structure and the magnitude of the vorticity vector at the exit plane. The simulation shows that there is a stronger swirl on the leeward side for cavitating flow. Once the fuel flows out of the orifice, without the constraint of the wall boundary the stronger velocity components in cross and vertical directions tend to cause the jet to break up earlier.